2014 Annual Report

Final Technical Report
Grant number DE-FG02-08ER54979

"Integrated Prediction and Mitigation Methods of Materials Damage and Lifetime Assessment during Plasma Operation and Various Instabilities in Fusion Devices"

Principal Investigator: Ahmed Hassanein

Co-Investigators: Jeff Brooks, Valeryi Sizyuk, Gennady Miloshevsky, Tatyana Sizyuk

Postdocs: Prasoon Diwakar, Jitendra Tripathi

Students: Xue Yang, Alice Hu, Filippo Genco, Anastassiya Suslova, Montaser Al-Ajlony

Institution: Purdue University, West Lafayette, IN

CONTENTS

I. Introduction

Edge plasma evolution plays major role in tokamak plasma confinement and determines/control the High-confinement mode (H-mode) operation. Experiments show the complex character of the edge plasma interaction with tokamak components and as a result the complex self-consistent behavior of plasma in the entire SOL. Successful development of future fusion reactors critically depends on the correct prediction of the heat and particle loads to reactor walls and the optimum materials choice for plasma facing components (PFCs). Experimental data of current tokamak devices and theoretical predictions show that future ITER-like surfaces should be resistant both to steady state heat flux of up to 20 MW/m^2 and to intense transient (τ = 0.1-10 ms) events of up to 10 GW/m^2. The divertor plate is a key component of the tokamak device. High particle and heat fluxes can cause high surface sputtering, melt and vaporization erosion, plasma contamination, and components failure that can interrupt normal operation of the reactor. The reactor geometry, the magnetic configuration, and the interaction processes in the Scrape-of-Layer (SOL) determine not only heat transport and loads to component surfaces but also play an important role in plasma confinement and control the transition to the high-confinement mode (H-mode) operation. Experiments in current tokamak devices show the complex behavior of edge plasma interaction with device components and as a result the required understanding of the complex self-consistent behavior of plasma in the entire SOL configuration. The edge plasma interaction with component surfaces affects the behavior of D-T bulk plasma and impurity contaminations, influences toroidal plasma motion, and redistributes energy loads among reactor components. Damage of plasma facing and structural materials due to loss of plasma confinement remains one of the most serious concerns for safe, successful, and reliable reactor operation. Plasma instabilities occur in various forms such as hard disruptions, which include both thermal and current quench, Edge Localized Modes (ELMs), runaway electrons, and Vertical Displacement Events (VDEs). Therefore, accurate understanding of the escaping core plasma into SOL and the subsequent interaction with device components is extremely important for successful development, operation, and optimization of future fusion devices. Current fusion reactors have complex 3D design and simple one-or two-dimensional models cannot be used for correct description of self-consistent processes of edge plasma evolution. Transport of charged particles in tokamak plasma environment is best described by the kinetic theory [1]. However, solving the full kinetic equations remains impractical task and most recent investigations [2-5] are based on the magnetohydrodynamic (MHD) approach for the modeling core plasma expansion into the SOL area. Simple estimation, for example of the National Spherical Torus eXperiment (NSTX) tokamak pedestal plasma conditions [6], i.e., for $n_e = 7 \cdot 10^{13}\ cm^{-3}$, $T_e = 500\ eV$, and $T_i = 750\ eV$, showed that the time between scattering events [7] for ions is $\tau_i = 4 \cdot 10^{-4}\ s$, and for electrons is $\tau_e = 4 \cdot 10^{-6}\ s$. The predicted parameters for ITER pedestal plasma ($n_e = 3 \cdot 10^{13}\ cm^{-3}$, $T_e = 1.7\ keV$, and $T_i = 2.5\ keV$ [8]) give even more pessimistic numbers that prevents the correct use of the Navier-Stokes equations: $\tau_i = 1 \cdot 10^{-2}\ s$, and $\tau_e = 2 \cdot 10^{-4}\ s$. The classical MHD approach assumes that the time between particles scattering is much smaller than duration of the simulated events (duration of the Edge Localized Modes (ELM) time is about $\tau_{ELM} = 10^{-4} - 10^{-3}\ s$ [9]). However, as it was shown in recent studies [2-4], implementation of various modifications and assumptions to the basic MHD system of equations allows to calculate the parameters of the escaped core plasma particles close enough to the measured experimental data. The main problem lies in the fact that transport properties of the tokamak magnetized plasma cannot accurately be described with pure classical theory. The classical transport theory is valid for collisional plasma in a homogeneous and stationary magnetic field [10]. The classical theory should be expanded to include various turbulence mechanisms to explain the anomalous plasma transport properties in tokamaks [11].

The simulation results were significantly improved when the general SOL transport problem was divided into two subtasks: 1) MHD of the escaping core plasma, starting from the last closed flux surface

(LCFS); and 2) MHD of the SOL neutrals (background gas) [3]. Solution of the first subtask for the escaping core plasma is used as a volume source for the neutrals transport equations. This approach was used in a simplified NSTX geometry where the profiles of divertor heat and particle fluxes were calculated and compared with experimental data [12]. Recent investigations showed that splitting of the SOL transport problem and implementations of various hybrid approaches are prospective ways for better modeling of edge plasma evolution and correctly predicting components heat loads [13-16]. However, it should be stated that full direct integrated model of the SOL plasma is still very complex problem and only simplifications allow simulating characteristics of tokamak operation in reasonable time.

Most recent experimental and theoretical studies of PFCs erosion only considered plasma behavior around local areas of the tokamak geometry [17-20]. Investigators have significant limitations in computational power and relevant experimental data due to design complexity, numerous physical processes involved, and difficulties in the integration of micro- and macro-scale processes. However, understanding various edge plasma processes and their interdependency in the entire SOL area are critically needed for accurate and reliable operation of future higher power devices. In our foregoing study [21] we simulated the evolution of edge plasma during the normal and disruptive operation of tokamak devices also in localized areas of the SOL using our HEIGHTS (High Energy Interaction with General Heterogeneous Target Systems) computer simulation package containing various integrated models [22-24]. These simulations showed a potential serious damage of nearby divertor surfaces in ITER-like devices during giant ELMs and disruption, not directly from the core plasma particles but from the high radiation fluxes of the evolving divertor plasma-shielding layer.

Based on our previous results [18, 25], we should emphasize that the PFC heat load processes, erosion dynamics, and damage spatial profile are closely intercorrelated with the escaped core plasma parameters, divertor magnetohydrodynamic (MHD) evolution, and radiation transport processes during edge localized modes (ELMs) and disruptions. To simulate realistic tokamak divertor/edge/core plasma interdependences, we have developed, implemented, and benchmarked new kinetic Monte Carlo models for the escape of core plasma particles during these events [26]. The main goal of that study was to integrate Monte Carlo models of core plasma impact with an MHD description of the evolving contaminant plasma into one hybrid model and simulation package in the upgraded HEIGHTS package. Surface vaporization due to intense power deposition is the main mechanism of divertor plasma initiation. Macroscopic erosion and splashing of melt layers during plasma transients are treated separately [27]. This mixed approach provides the advantage (compared to most existing models) of considering properties of the core and divertor plasma in parallel. In this approach, the divertor plasma is not simple hydrogen ions but is a partially ionized contaminated plasma of the surface material as seen in various laboratory plasma applications [28, 29], specifically carbon or tungsten contaminants in the present study. The core plasma is described as clean D/T flow in a kinetic model [26]. The response of ITER divertor nearby surfaces due to radiation from the divertor-developed plasma was simulated using actual full 3D reactor design and magnetic configurations. We analyzed in details the radiation emission spectra and compared the emission of both carbon and tungsten as divertor plate materials. The integrated 3D simulation predicted unexpectedly high-damage risk of the open stainless steel legs of the dome structure in current ITER design from the intense radiation during a disruption on the tungsten divertor plate.

Tungsten is the leading high-Z candidate surface material for future tokamak divertor and first wall plasma facing components (PFC's), e.g. as discussed in [30]. There are good reasons for this choice including low activation, high melting point, good thermo-mechanical properties, low sputter erosion, and low tritium retention/co-deposition. However, there are concerns about He, D, T, and neutron-induced ultrastructure changes ("tendrils", bubble formation, etc.) and resulting surface integrity; fatigue, dust, and other issues; and a general major concern about relying on one material for the critical PFC surface. To broaden the options for fusion development we identified and examined five potential alternative high-Z plasma-facing materials: zirconium, niobium, molybdenum, hafnium, and tantalum. We categorize these, for the present purposes, as "Mo-class" or "W-class" materials, with some properties as listed in Table I.1. These can potentially serve as full-thickness structural/facing materials or thinner (~1-5 mm) coating materials. In the history of conceptual fusion power plant designs these alternative materials were

generally not considered for PFC's, due in large part to concerns about activation and waste disposal. The potential for *recycling* activated-material was recognized early, e.g. in the STARFIRE study [31]. However, most activation/recycling analysis appears to have been done for non-surface materials (blanket, shield, etc., e.g. Ta-5W structural material in [31]), focusing on hands-on recycling. More recent developments of advanced remote handling equipment suggest recycling all fusion components, including PFCs [32]. Since plasma/material interactions has emerged as a critical fusion technology issue we believe that all possible plasma facing surface material options must be considered, and none should be excluded based on geologic disposal considerations. The aim of this work is a first-order assessment of alternative high-Z plasma-facing material feasibility. We first examine the activation/waste-disposal issue, and then the critical performance issues of sputter erosion/redeposition and transient response. The focus is on *comparisons* to tungsten. Results are encouraging, in particular, none of these materials are ruled out - from the standpoints examined here - and we strongly encourage further study of these material options by the fusion community.

Table I.1. Candidate high-Z plasma facing surface materials.

Class	Element	At. No.	Melting pt. Deg. C	Atomic density, 10^{28} atoms/m^3
Z~42	Zr	40	1855	4.25
	Nb	41	2477	5.40
	Mo	42	2623	6.36
Z~74	Hf	72	2233	4.39
	Ta	73	3107	5.48
	W	74	3422	6.28

II. Plasma Photon Transport and Tungsten Response

A simple estimation from the energy deposited onto divertor surface during core plasma instabilities predicts a massive flow of divertor material with density up to ~ 10^{17} cm^{-3} near surface that is much higher than the SOL hydrogen plasma values ~ 10^{13} cm^{-3}. These conditions allow treating the divertor plasma evolution as the main process and the core/SOL plasma processes as perturbations to the main process by modeling of the nearby surface phenomena. This dense divertor plasma hydrodynamic evolution enables the use of the extensive models developed for laboratory plasma devices. The magnetohydrodynamics, atomic physics, radiation transport, and heat conduction processes can be simulated in the dense evolving divertor plasma similarly to laser- or discharge-produced plasma devices [28].

Radiation transport is usually considered the most important aspect when simulating laboratory plasma devices used as radiation sources. The spectral and output power characteristics of the laser- or discharge-produced plasma devices should be described very accurately, for example in the optimization of future extreme ultraviolet (EUV) advanced lithography sources [33]. The significant progress and success achieved in the modeling and simulation of these plasma devices is now being used for tokamak divertor plasma modeling. Below we present the new Monte Carlo radiation transport model developed and incorporated into our HEIGHTS computer package and show new and detailed results of PFC and nearby surface heat loads that have never been predicted before. The HEIGHTS package contains various models of atomic physics and plasma opacity calculations. Determination of detailed opacities was the subject of our previous analysis, and publication and the results are only referenced in this work. Optical

coefficients of candidate materials were precalculated and tabulated during our extensive investigations of discharge- and laser-produced plasma devices such as plasma focus, z-pinches, hollow cathode devices, etc., that are appropriate to use based on the enhanced collisional-radiative-equilibrium (CRE) model. Those studies showed good agreement of our calculations with several experiments, for example in EUV photon generation sources [33]. Divertor-generated plasma (i.e., impurity plasma of divertor material such as tungsten or carbon) during giant ELM and disruption is sufficiently dense over a longer time scale, as predicted from the self-consistent integrated solution and energy conservations. The plasma conditions are very similar to those in previous studies of discharge- and laser-produced plasma.

Earlier we reported that direct Gauss integration of the radiation transport equation results in significant computation load to achieve reasonable accuracy [34]. Similarly, direct Monte Carlo simulation methods of the whole ensemble of radiation particles require large memory to track various particles parameters [35]. We developed weighted Monte Carlo methods for detailed calculations of photon emission, propagation through SOL, and deposition into the wall/evolving vapor plasma, and into nearby components. The algorithm is based on data analysis and accumulation regarding the generation and subsequent evolution of particles and has the advantage of being relatively straightforward to apply for complex geometries such as illustrated in Fig.II.1. We used numerical schemes with weighted hierarchy of statistically accumulated events. Two major weight factors were implemented: normalization of emitted photon "bundles" relative to the most radiated cell in the computational domain, and normalization of the photon bundle magnitudes relative to optical thickness of the cell. The first weight coefficient enables us to detail the emission processes by neglecting cold cells emission. The second coefficient allows "idle" processes to be ignored, such as situations with emitting and absorption in one cell (absorbed lines). These coefficients helped to significantly decrease the computational time. From the results of the preliminary calculations in strongly non-uniform mesh, a third weight coefficient is found to be useful. If the volume of the emitting cell is very small then the amount needed to simulate photon bundles should not be zero to prevent excluding the extremely small cells (in most important regions) from the radiation transport. The volume weight coefficient considerably increases the computation accuracy in this case. The implementation of these three weight coefficients made our 3D Monte Carlo methods very efficient, enhanced accuracy, and accommodated complex 3D realistic geometry.

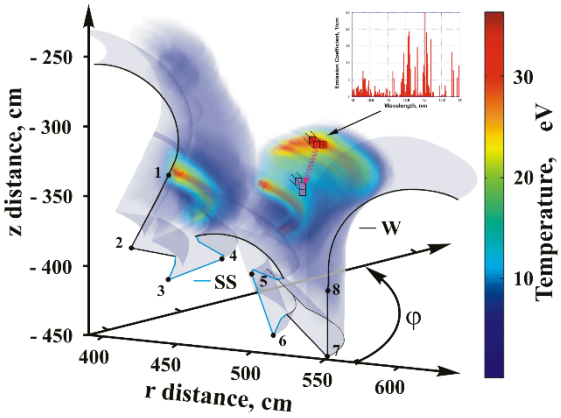

Figure II.1. Schematic illustration of Monte Carlo RT model for ITER geometry: 1-8 are dedicated points.

As previously described [36], to obtain the number N of photons emitted in space (per unit volume per unit time), the emission coefficient k_{em} should be integrated with Planck's function $B(\omega)$ in the full spectrum:

$$N = 4\pi \int_0^{\infty} \frac{k_{em} B(\omega)}{\hbar\omega} d\omega, \quad \text{where} \quad B(\omega) = \frac{\hbar\omega^3}{4\pi^3 c^2} \left(e^{\frac{\hbar\omega}{T}} - 1 \right)^{-1}. \tag{II.1}$$

For the convenience in the optical parameters calculations, we use the Gaussian unit system with the energy and temperature units given in electron volts [eV]. The integration of the number of photons gives the following expression that used in our numerical simulations:

$$N = \int_{E_{\min}}^{E_{\max}} \frac{k_{em}(E,T,\rho) E^2}{\hbar^3 \pi^2 c^2} \left(e^{\frac{E}{T}} - 1 \right)^{-1} dE, \tag{II.2}$$

where E is energy of emitted photon; $E_{\min}, E_{\max}$ is spectral energy range; $k_{em}(E,T,\rho)$ is emission coefficient; T is plasma temperature; ρ is plasma density; $\hbar$ = 6.58217×10^{-16} [eV·s] is Planck's constant; and c is speed of light. From the adaptive mesh refinement (AMR) cell volume V_i, temperature T_i, and density ρ_i we calculate the total amount of photons N_i generated per unit time:

$$N_i = V_i \int_{E_{\min}}^{E_{\max}} \frac{k_{em}(E,T_i,\rho_i) E^2}{\hbar^3 \pi^2 c^2} \left(e^{\frac{E}{T_i}} - 1 \right)^{-1} dE, \tag{II.3}$$

where i is the cell index in unstructured mesh. By analogy with the emission process, the attenuation of light intensity as a result of absorption in mixed media can be expressed as $I = I_0 \exp\left\{ -\int_0^l k_{abs}(\omega,l) dl \right\}$ or the same in photon number terms [37]:

$$N(\omega) = N_0(\omega) \exp\left\{ -\int_0^l k_{abs}(\omega,l) dl \right\}. \tag{II.4}$$

Here $N_0(\omega)$ is the initial number of photons with frequency ω and l is the path length. Considering the photon path within one cell (where we assumed the absorption coefficient is independent of the coordinates) the attenuation can be expressed as:

$$N(\omega) = N_0(\omega) \exp\{ -k_{abs}(\omega) l \}. \tag{II.5}$$

The absorption P_{abs} and transition P_{trans} probabilities of the photon along the path with length l in the $\{i\}$ cell following Eq. (II.4) are given by:

$$P_i^{abs}(\omega) = 1 - \frac{N(\omega)}{N_0(\omega)} = 1 - \exp\left\{ -k_{abs\{i\}}(\omega) l \right\}, \quad P_i^{trans}(\omega) = \exp\left\{ -k_{abs\{i\}}(\omega) l \right\}. \tag{II.6}$$

After sampling the photon energy, photon transport in computational domain cells is simulated by checking each cell for the absorption probability. The sum of all sampled emission and absorption results, i.e., $N = \sum_i N_i^{sim}$ gives information about the energy redistribution in the computational domain due to photon transport. The total amount of photons in most radiated cell is used for the initial normalization of

photon bundles. A reasonable degree of accuracy requires the minimum simulation number of emission not to be less than N_{sim}. Based on this assumption the first weight coefficient of photon bundle can be written as:

$$W_1 = \frac{N^{\max}}{N_{sim}}\ , \qquad \text{(II.7)}$$

$N^{\max}$ is the integral (Eq. II.3) in the most radiated cell and N_{sim} is the real number of photons that will be sampled in this largest cell. To obtain a reasonable accuracy for the radiation transport calculations, we require generating N_{sim} ~10^3 photon in most radiated cells. With Monte Carlo radiation transport method, one can simulate situations in which a spectral band can be completely absorbed within one cell volume. Our Monte Carlo algorithm in this case defines an "idle case", i.e., particle energy is subtracted from the cell energy by emission simulation and is added by absorption in the same cell. The second weight coefficient introduced to solve this problem is given by:

$$W_{2\{i\}}^{n} = k_{abs}\left(E_n, T_i, \rho_i\right)\Delta r_i\ , \qquad \text{(II.8)}$$

$W_{2\{i\}}^{n}$ is the weight coefficient of the n-th spectral range in the $\{i\}$ cell; $k_{abs}(E_n, T_i, \rho_i)$ is the absorption coefficient of the n-th spectral range in the cell $\{i\}$; and Δr_i is the characteristic size of the cell. If the expression (Eq. II.8) is less than 1, the second coefficient is set equal to 1. We assume that the photon energies are distributed equally within one spectral range. Hence, linear interpolation was used to sample the emitted particle energy E_{ph}. Taking into account both weight factors gives the energy of the photon bundle $E_{ph}^{sim} = E_{ph} W_1 W_{2\{i\}}^{n}$ as a function of the spectral range number n. The range number is determined with the real physical energy of photon E_{ph}. During the RT simulation, the value E_{ph}^{sim} is subtracted from the cell energy by the emission processes and added by the absorption processes. The balance between the cell emitted and absorbed energy is the source term Q_{rad} in Eq. (1) of Ref. [26]. This term determines energy redistribution in plasma due to radiation and in ideal case should be recalculated each MHD time step. In practice, the MHD and RT time steps can be not equal and are determined according to the required calculation accuracy and numerical stability of the solution. Applying of additional counters at the cell borders allows calculating the radiation fluxes in matter. The model easily determines the radiation fluxes on surfaces having complex geometry. This is very important for the calculation of the effect of vapor radiation on nearby "hidden" components.

In the calculation of radiation transport in plasma, the integral radiation fluxes depend, to a great extent, on the level of details and precision of the optical coefficients. In turn, the computational accuracy and completeness of the calculated opacities depend on the accuracy and completeness of the atomic data. Since the details of opacity and atomic data calculations are beyond objectives of this work, we refer to our previous publications [38, 39]. Briefly, we note that the structure of atomic energy levels, wavefunctions, transition probabilities, ionization potentials, oscillator strengths, broadening constants, photoionization crosssections, and other atomic characteristics are calculated using the self-consistent Hartree-Fock-Slater (HFS) method [40]. The collisional-radiative equilibrium (CRE) model [41] was used to calculate the populations of atomic levels and the ion and electron plasma concentrations. Because the original CRE model satisfactorily describes the optically thin plasma, the escape probability approximation for line transitions and direct photoionization for the continuum spectrum was applied to reduce the nonlocal radiation effects [42]. From our developed and implemented HFS-CRE models, the thermodynamic and opacity properties of both C and W plasmas were calculated in a wide density and

temperature range: from 10^{10} up to 10^{21} cm^{-3} and from 0.02 up to 250 eV respectively. The emission and absorption coefficients were also determined using CRE model in a wide range of photon energy from 5×10^{-2}eV up to 1×10^{5} eV using super-fine mesh (10^{5} points per full spectrum) for detail isolation of thin spectral lines. Unfortunately taking into account additional plasma density and temperature scales result in enormous data array density/temperature/photon energy $\left(15\times30\times10^{5}\right)$ that cannot be used in reasonable time for the integrated 3D simulations of the entire device. On the other hand, as showed in our previous laboratory plasma studies [28, 43], correct radiation transport modeling requires detail consideration of energy transfer in strong lines along with the continuum spectra. To allow simulation of RT of strong lines we optimized the initial opacities tables and separated full plasma spectrum onto spectral groups where optical coefficients are relatively invariable. Figure II.2 shows sample optimization of tungsten opacities for a preset ratio of opacity variation $R = 0.5$. The variation ratio R is determined as opacity change ratio inside the selected spectral group. Because plasma spectrum depends critically on the temperature, the collected spectral groups are different for each temperature value. The especially developed computer code (i.e., spectrum zipper) combines group locations in one final set that valid for all temperature values and recalculates the opacities for each group.

This recalculation is based on conservation of the total photon number given by Eq. II.2. In this way the variation ratio R becomes an initial variable that determines the final groups amount and the final accuracy of the RT calculations as a result. Preliminary calculations showed reasonable RT calculations accuracy with $\sim 2\cdot10^{4}$ groups for tungsten (19913 groups in Fig. II.2), $\sim 3\cdot10^{3}$ groups for carbon, and $\sim 2\cdot10^{3}$ groups for lithium that depends evidently on the complex atomic structure of the element [44]. To validate the developed RT model and to benchmark HEIGHTS package, we simulated several laboratory plasma problems and compared our results with known analytical and experimental results. The agreement is very good and more detailed information about the validation of our new RT model can be found in Refs. [43-46].

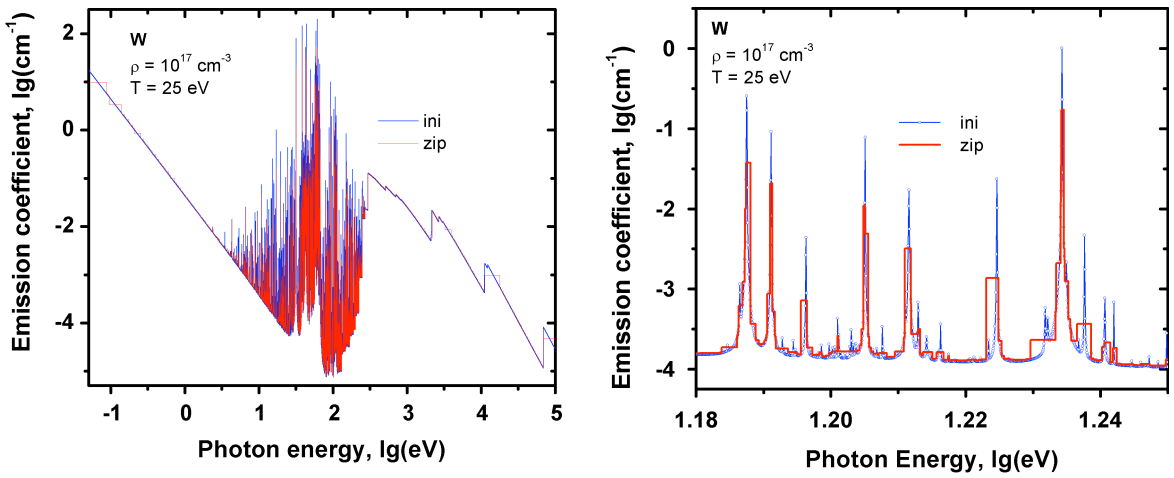

Figure II.2. Optimization of tungsten opacities of the divertor plasma for RT calculations a) full spectrum, b) fine structure.

We implemented the above described radiation transport model in our HEIGHTS package and integrated with the earlier developed model of the escaping core plasma [26], the adaptive mesh refinement magnetohydrodynamic model for the edge plasma [26], the magnetic diffusion, and multiscale mesh coupling of subsurface processes with the SOL plasma models [18] for the detail simulation of the reradiation phenomena in edge divertor plasma. We simulated the evolution of the initiated divertor plasma and particularly its radiation characteristics during and directly after an ELM and a disruption in

ITER device with its current full 3D divertor design [47]. Using the predicted ITER core plasma parameters [18], we calculated the radiation fluxes and heat loads on component surfaces for C and W as potential candidate divertor materials. Schematic illustration of the computational domain in the poloidal crosssection is shown in Fig. II.3. The initial magnetic field structure and location of various component materials are also shown. As in our previous study [26], we started from the equilibrium magnetic field configuration extracted from the EQDSK database files and assumed the initial divertor plasma pressure of 10 Pa. Figure II.3 shows carbon being the divertor plate material however in the calculations below, we also compared tungsten and lithium under similar plasma impact conditions. The implementation of the AMR mesh allowed simulations in the entire SOL area and the presented results are calculated self-consistently involving all physical processes through out the SOL. See for example our discussion about the particle balance between the low- and high-field divertor plates in Ref. [26]. Below, we present the simulation results in zoomed regions of interest (ROI) (see Fig. II.3) for better clarity.

From our preliminary simulation results, RT in the divertor plasma plays key role in the heat flux load of ITER components and surfaces erosion [18]. We predicted the damage due to indirect radiation to the nearby components during giant ELMs and disruptions on divertor plate using local domain simulations. Our simulations show that the radiation fluxes and heat loads to nearby surfaces depend not only on the local impact parameters but also on the integrated behavior of the whole SOL plasma and how it depends on properties and evolution of the divertor plasma material.

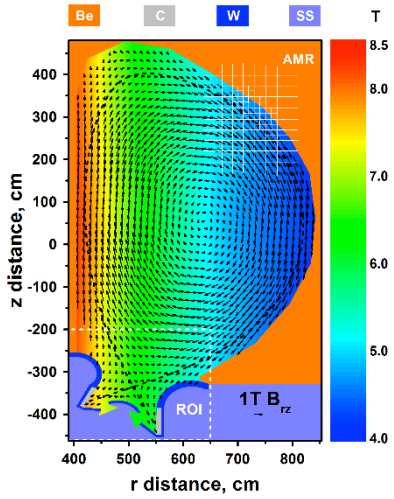

Figure II.3. Schematic illustration of the computational domain with AMR and different component materials: Be, C, W, and SS (stainless steel).

The divertor plasma developed as a result of disruptions/ELMs is composed mainly from component materials that greatly increase the contribution of radiation transport in the total energy balance in comparison to the treatment of clean DT plasma [48, 49]. For the difference in performance, we compared the incident radiation flux on the divertor surface during a giant ELM for tungsten, carbon, and lithium as potential divertor materials. The giant ELM energy (10% of the total) was assumed to be $Q = 12.6\ MJ$, temperature of escaped core plasma $T = 3.5\ keV$, and the impact duration $\tau = 0.1\ ms$. A detailed description of the core plasma escaping model and its numerical implementation with initial and boundary conditions, are presented in Ref. [26]. The considerable differences in radiation fluxes shown in Fig. II.4 for the W, C, and Li divertor plate are striking evidence of the importance of material choice of PFCs in tokamak design. The flux distribution is shown for the time $t = 30\ \mu s$ between the 7 and 8 locations (See Fig. II.1 for specific points location). This time moment in this figure and below is used

due to sufficiently developed physical processes and the start of intense over heating of stainless steel components during a disruption at this time.

It can be seen that the radiation power from tungsten-developed plasma is very large compared to carbon and lithium. We did not specifically calculate the radiation flux assuming hydrogen plasma but it can easily be estimated to be very low from Fig. II.4 by extrapolation of data shown. The calculated radiation fluxes confirm not only increasing of the total radiation energy load from the divertor material for the higher Z materials but also show different spatial divertor plasma evolution for the same incident ELM parameters. The core plasma impact energy is distributed among three different regions: direct particle energy deposition into divertor surface, developed vapor and plasma heating, and radiation of heated plasma to nearby components. Figure II.4 shows that large portion of the initial plasma impact in the case of carbon divertor plate is spent on plasma thermal energy, i.e., the temperature of carbon cloud would be much higher than that for tungsten cloud.

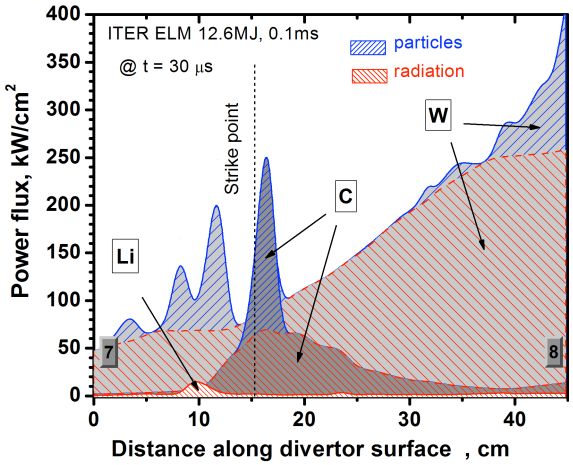

Figure II.4. HEIGHTS predicted radiation (left incline) and particle (right incline) fluxes on the ITER divertor plate surface during giant ELM.

The radiation flux peak has certain forward shift with the material atomic number as shown in Fig. II.4, i.e., different plasma cloud evolution, location, and plasma shielding characteristics. Different plasma dynamics have different plasma density and temperature distribution, which determine maximum fluxes around the radiated plasma cloud. Figure II.5 shows distribution of plasma temperature where considerable lower temperatures can be seen of the developed divertor plasma in the tungsten case. According to our HEIGHTS simulation, the volume and drift velocity of the hot plasma area is also several times smaller in the tungsten divertor compared to the carbon case. However, this could have negative consequences regarding the final heat load of divertor components. As noted above and discussed in Ref. [26], the self-consistent treatment of particles drift in SOL correctly predict the energy exchange between the low- and high-field tokamak sides (inner and outer divertor plates) and the resulting additional damage of the low-field divertor plate in the tungsten case.

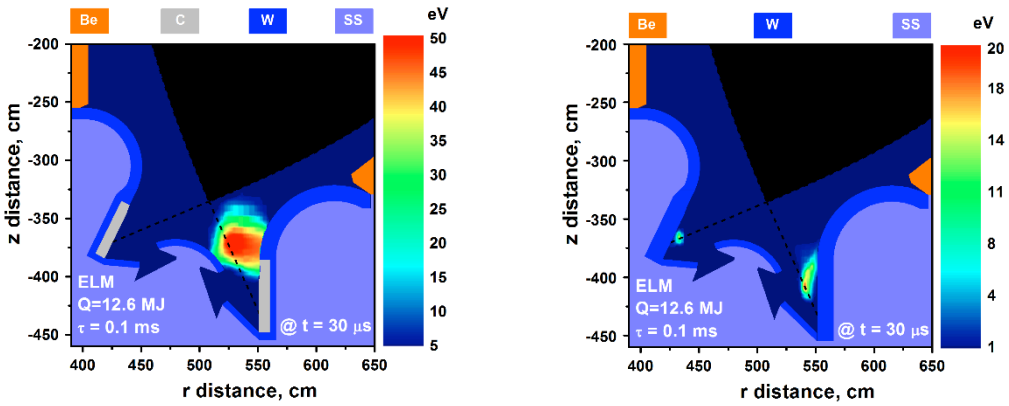

a) b)

Figure II.5. Distribution of plasma temperature in the divertor space during giant ELM: a) carbon divertor plate, b) tungsten divertor plate.

The development of the second high temperature area above the low-field divertor plate is noticeable in Fig. II.5b, left side. Individually, the plasma temperature does not determine the final radiation fluxes profile but coupled with plasma density and the input energy. Figure II.4 shows the carbon peak location of the radiation flux is closer to the strike point while the temperature distribution indicates an opposite situation. Previously, we studied the effect of various processes on plasma evolution in future plasma lithography sources with regard to the conversion efficiency of these sources for emission and collection of EUV photon radiation power [50]. Opposite to the expectation that radiation power is determined with correct plasma density-temperature combination [51], we found that radiation transport and hydrodynamic processes coupled with the external input energy play critical role in determining the final emitted radiation power. The giant ELM simulations predict smaller evolution of plasma density for tungsten divertor case with maximum around $\sim 10^{16} cm^{-3}$ at the second high temperature area above the low-field plate (Fig. II.6). However, as we show below this amount of high-Z impurities is sufficient for the initiation of a high-power radiation source in the divertor space. The escaping core plasma particles are the energy source for generation and evolution of the divertor shielding plasma and consequently determine location and size of the developed radiation source. Most radiated area in the evolving plasma cloud is the result of three dynamical components: density, temperature, and the input energy.

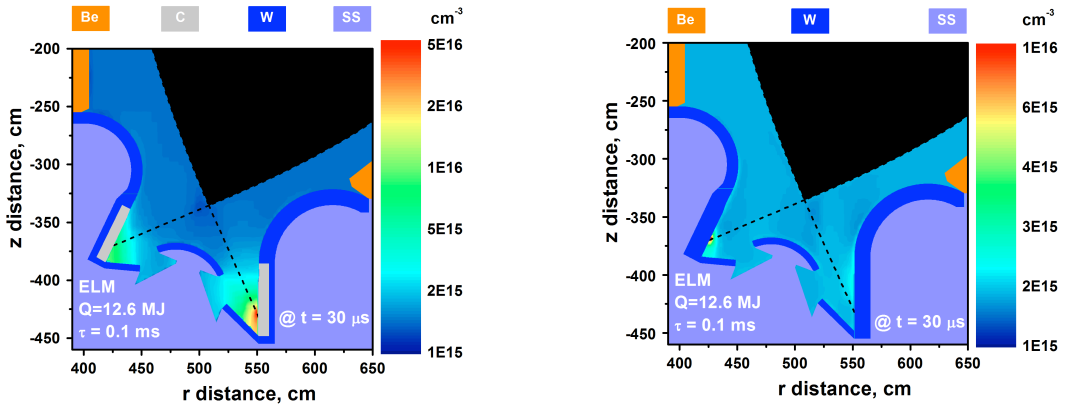

a) b)

Figure II.6. Distribution of plasma density in the divertor space during giant ELM: a) carbon divertor plate, b) tungsten divertor plate.

Figure II.7 shows that the deposition/absorption of the escaped core particles energy in the evolving divertor plasma is the main determining process of radiation emission. The produced divertor plate plasma has sufficient density in this area for effective absorption of the incident impact energy and the subsequent radiation emission from the localized hot temperature areas.

Comparison of the input energy areas, temperature distribution, and the full area of the calculated radiation fluxes shown in Fig. II.8 illustrates the dynamic formation of the radiated plasma cloud/blob and the shielding processes. It can be seen in the tungsten case the much higher radiation fluxes and larger exposed areas. In our previous work [18], we predicted the high values of the radiation fluxes on the divertor nearby surfaces but in this work we show the effect of various divertor materials on the final thermal response of the "hidden" dome components in current ITER design. Figure II.8b shows the dome (umbrella) legs as the most exposed and high-risk location for the secondary radiation heat load from the evolving tungsten divertor plasma, particularly on these cooling tubes that are made of stainless steel [47].

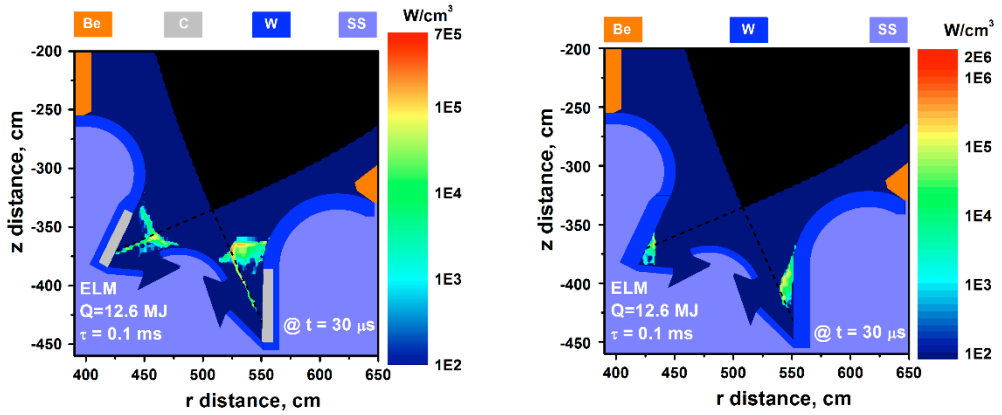

a) b)

Figure II.7. Energy deposition of the escaped core particles into the generated divertor plasma cloud during giant ELM in ITER: a) carbon divertor plate, b) tungsten divertor plate.

The upgraded HEIGHTS integrated models can now calculate the direct (from the escaped core particles) and indirect (from photon radiation) heat loads and heat conduction inside all tokamak chamber surfaces due to the AMR implementation methods.

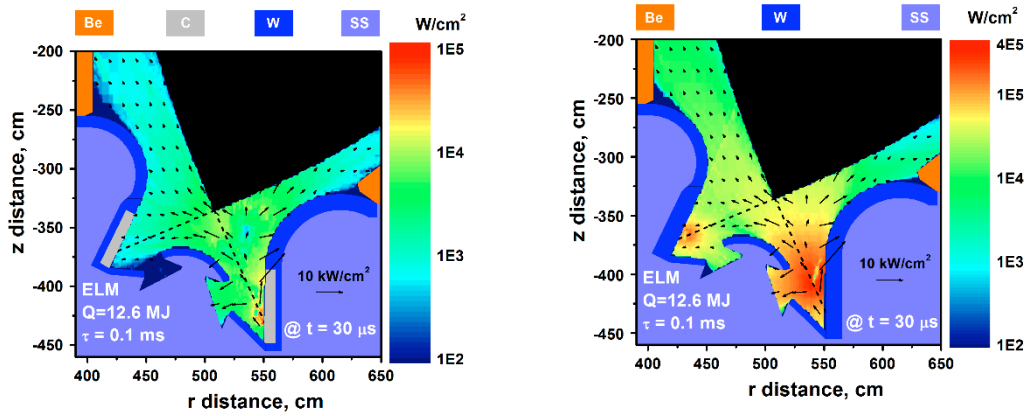

a) b)

Figure II.8. Distribution of radiation fluxes in the divertor space during giant ELM: a) carbon divertor plate, b) tungsten divertor plate.

Figure II.9 shows HEGHTS the calculated surface temperature of ITER dome umbrella tubes on the low-field side between locations 5 and 6 (See Fig. II.1 for points location) during the ELM and disruption. The giant ELM (Fig. II.9a) insignificantly heats the stainless steel tubes in the case of carbon divertor plates but up to $\sim 900\,K$ in the tungsten case, which may also be acceptable. The initial temperature of the tubes was assumed to be $500\,K$. In contrast to the ELM case, a full disruption on tungsten divertor will cause significant heating of the tube surface and up to the melting and vaporization temperatures in the first $25\,\mu s$ (Fig. II.9b). Melting and vaporization temperatures of stainless steel are marked with dashed lines. As in our previous study [18], we assumed the full discharge energy to be $Q_{DIS} = 126\,MJ$, disruption duration $\tau = 0.1\,ms$, and temperature of the escaped core plasma $T = 3.5\,keV$.

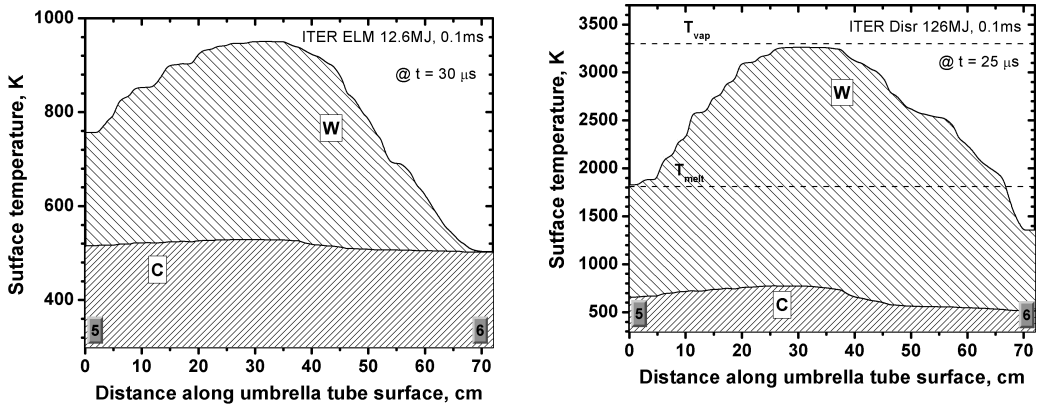

a) b)

Figure II.9. Temperature distribution of the dome leg surface during a) giant ELM, b) disruption

In the case of a carbon divertor plate no significant overheating of the umbrella tubes is expected during disruptions. Figure II.10 shows the dynamics of surface heating in the most irradiated section of the umbrella tubes placed at distance ~ 32 cm between the 5 and 6 locations (Fig. II.9). The surface temperature increases up to maximum value in the first ten microseconds of the disruption while in giant ELM reaches much lower temperature peak at longer time because of the smaller radiation power. The maximum temperature and location in tungsten case is due to the small hot size of the radiated plasma cloud in comparison to the carbon plasma. The maximum temperature corresponds to the location of the drifted divertor plasma closely to the monitored surface. Subsequent decrease in temperature is related to the umbrella shielding. The umbrella shielding is not as effective for the initially larger carbon plasma cloud.

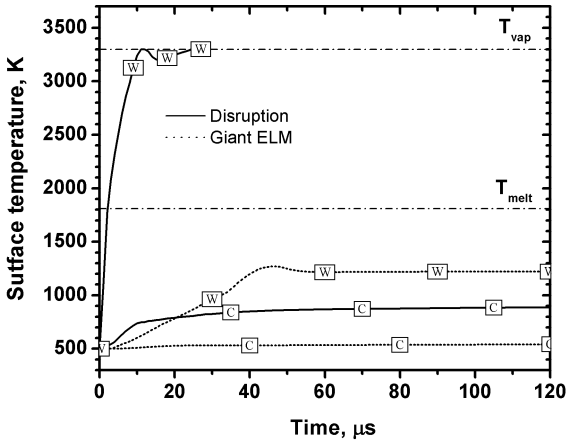

Figure II.10. Dynamic of the SS tubes radiation heating during ELM and disruption

Relevant SOL plasma parameters summarized in table II.1 confirm the complex self-consistent behavior of the escaped core plasma-divertor surface interaction during ELMs and disruptions. Starting from the initial values of Q_{IMP} and Q_{DIS}, we calculated the energy distributions during a giant ELM and disruption. The *ImpEnPlas* is the part of the escaped plasma energy deposited into the edge plasma. Comparison shows that carbon plasma is better energy absorber of the impact energy: ~75% of ELM energy and ~94% of disruption energy compared to ~60% and ~89% in tungsten case respectively. We calculated the percentage from the initial impact energies Q_{ELM} and Q_{DIS}. In both C and W cases, the energy absorption is more efficient during the disruption that can be explained due to stronger shielding effect. The escaped core plasma particles erode the divertor surface and form a plasma cloud from the material vapor, i.e., core plasma influences the generation of divertor plasma. In our previous study [26], we assumed the opposite process where the generation of the divertor plasma influences core plasma-escaping process. Redistribution of the absorbed impact energy between the low- and high-field divertor plates (inner and outer plates) *ImpEnDiv_L*, *ImpEnDiv_H* confirms this assumption. During the ELM in both C and W cases, the absorbed energy in low-field side plate is larger than in high-field side plate. During the disruption however, we conclude an opposite behavior. The high-field side plate is loaded higher that can be explained by the back-influence of MHD processes of the divertor plasma cloud on the escaping of core plasma particles. Having carbon as the divertor plate material provides better protection of the divertor surface because the generated carbon plasma cloud absorbs and keeps larger part of the core impact energy. However, this part increases mainly the temperature of plasma cloud while in tungsten case the energy is used for more ionization.

The *RadEn* is the energy emitted from the entire SOL edge plasma during the ELM or disruption. In the carbon case during ELM, the divertor plasma reradiates ~3.7% of initial energy vs. ~45.5% in tungsten case. The difference in divertor plasma reradiation between C and W increases with the impact energy. For disruption, the reradiated energy reaches higher value ~70% for the tungsten plates. However, a comparison of the radiation energies absorbed in the divertor plates during disruption (See *RadEnDiv_L*, *RadEnDiv_H* in table II.1) shows not such large difference between carbon and tungsten plates. This is typical result of the divertor plate damage that the localized simulations have previously shown [18, 25]. Expansion of simulation to include the entire SOL area shows fine details of the reradiated energy and spatial profile. In the W case most of the radiation energy will be redistributed to divertor nearby components. The summary of the divertor plates evaporated mass (*EvapMassDiv_L*, *EvapMassDiv_H*) and total evaporated mass in SOL (*EvapMassTot*) is good confirmation of these predictions.

Table II.1. Summarized domain plasma parameters integrated by ELM and disruption time.

Parameter, *Unit*	Giant ELM, Q = 12.6 *MJ*		Disruption, Q = 126 *MJ*	
	C	W	C	W
ImpEnPlas, *MJ*	9.42	7.52	118.5	112.3
ImpEnDiv_L, *MJ*	0.87	1.19	0.6	0.78
ImpEnDiv_H, *MJ*	0.41	0.82	0.74	1.08
RadEn, *MJ*	0.46	5.74	3.5	88.77
RadEnDiv_L, *MJ*	0.08	0.78	0.66	3.0
RadEnDiv_H, *MJ*	0.005	0.32	0.14	3.9
EvapMassDiv_L, g	0.91	0.48	2.33	1.17
EvapMassDiv_H, g	0.43	0.2	1.16	0.96
EvapMassTot, g	1.51	12.2	2.72	199.4[1]

[1] Including vaporized SS components

III. Plasma Facing Materials Alternatives to Tungsten

We examined the activation characteristics of the alternative high-Z materials and compared them to the tungsten-baseline armor of a divertor. The selected design for this activation analysis is ARIES-ACT-1 [52] — the most recent power plant design in the ARIES series. The ACT-1 advanced divertor is capable of handling high heat fluxes of 10 MW/m^2 (or more), and operating at high temperature of 800-1300 ^{o}C. The design calls for a 0.5 cm thick sacrificial armor layer to protect the divertor during operation. The 5.5 cm thick divertor consists of ~40% W-1.1TiC alloy, ~12% ODS ferritic steel, and 18% He coolant, by volume, as discussed further in [53]. The 14 MeV source neutrons will activate the armor and generate radioactive materials at the end of the divertor service lifetime (~4.5 years with 85% availability). The strategy for handling fusion activated materials calls for three potential schemes: disposal in geologic repositories, recycling within the nuclear industry, and clearance or release to the commercial market if materials contain traces of radioactivity. Plasma facing components normally contain high radioactivity and do not qualify for clearance. There is a growing effort in the U.S. and abroad to avoid geologic disposal for fusion materials. Alternatively, recycling offers a more environmentally attractive option through the reuse of the continuous stream of activated materials generated during operation and after decommissioning, e.g. as discussed in [32], minimizing the quantity categorized as radwaste needing disposal. Activation calculations for this study used the PARTISN one-dimensional transport code [54] and ALARA activation code [55] with FENDL cross-section libraries [8]. The entire divertor was modeled in poloidal, cylindrical geometry, with a typical average neutron wall loading of 1 MW/m^2. The irradiation history takes into account the 85% machine availability during the projected service lifetime of the divertor (~4.5 years). The alloying elements and complete set of impurities were included in the materials analysis.

In the U.S., the waste disposal rating (WDR) represents a metric for waste classification. A WDR < 1 means low-level waste (LLW) and a WDR > 1 means high-level waste (HLW). By definition, WDR is the ratio of the specific activity (in Ci/m^3 at 100 y after divertor replacement) to the allowable limit summed over all radioisotopes. As Figure III.1 indicates, only the W armor qualifies as LLW under ARIES operating conditions. If the armor is combined with the divertor structure, Ta and Zr could qualify as LLW (due to volume averaging), along with Hf if the Nb impurity is reduced to 1-2 wppm (down from 100 wppm). The Mo and Nb armors generate HLW if disposed of separately or combined with the divertor. Examining the recycling option, Figure III.2 reveals that all armors could potentially be recycled after a few years of storage using advanced remote handling (RH) equipment that is capable of handling high dose rates of 10,000 Sv/hr or more. In fact, W, Mo, and Hf could be recycled immediately after divertor replacement while Nb and Zr would require a few months of storage before recycling. None of the candidate armors could be recycled with hands-on operations because of the high radioactivity.

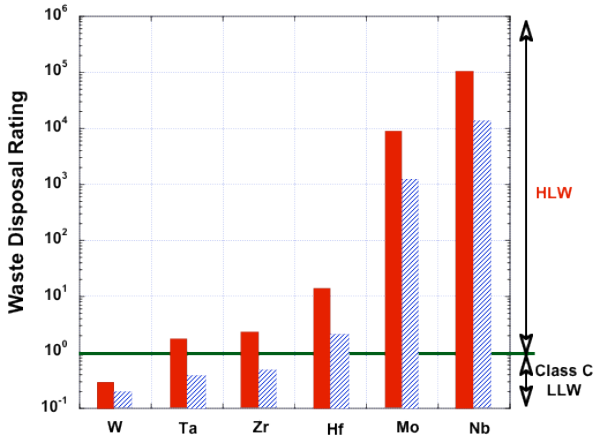

Figure III.1. Waste disposal rating of fully compacted ARIES-ACT-1 components after 3.8 MWy/m^2 of divertor neutron irradiation. Solid bars for armor only. Hatched bars for combined armor and divertor.

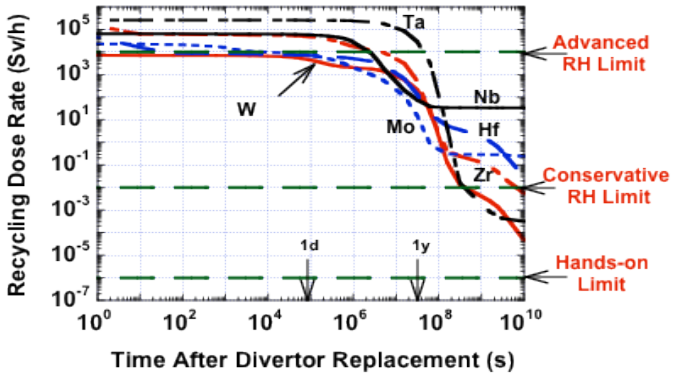

Figure III.2. Time variation of recycling dose rate to the remote handling (RH) equipment for candidate surface materials after divertor replacement (5 mm armor, after 5 year exposure)

The decay heat is another important parameter that determines the cooling needs during recycling, and the thermal response of in-vessel components following loss of coolant/flow accidents. Low decay heat is desirable as it offers safety advantages. The time variation of the decay heat is shown in Figure III.3 for the six armors. Tantalum generates the highest decay heat that remains unchanged for 10 days, while the molybdenum decay heat falls off relatively rapidly after one day. However, even for a few mm thick Ta coating, the impact on the temperature response during a loss of cooling accident is minimal. To conclude, all candidate armors could potentially be recycled with advanced remote handling equipment. Some may require active cooling during the recycling process. W, Ta, Zr, and Hf based divertors (with 1 wppm Nb) qualify as low-level waste while Mo and Nb generate high-level waste.

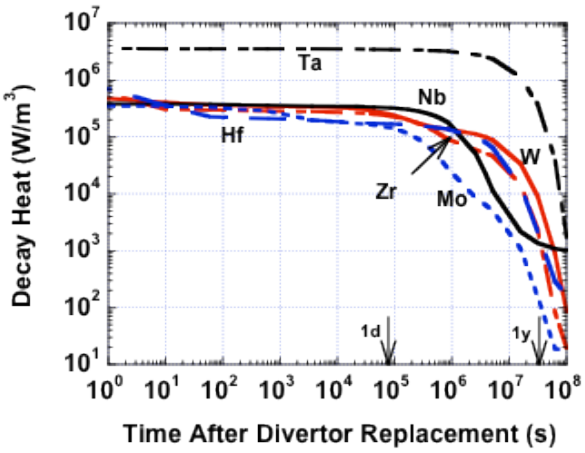

Figure III.3. Variation of armor decay heat with time after divertor replacement

Sputter erosion/redeposition affects the lifetime of plasma facing components, core plasma contamination, and tritium inventory due to codeposition, e.g. as discussed in [57]. For a given plasma solution the erosion/redeposition process is governed by surface (armor) material mass, binding energy, and atomic density; sputter yields and velocity distributions; impurity transport in the sheath and edge/SOL plasma; and redeposited material characteristics. The following information (data, models, code output, etc.) is required for full erosion/redeposition analysis of the candidate high-Z PFC materials:

- D-T, He, O, Ar (or other trace impurity) sputter yields (angle and energy-dependent), and sputtered atom energy/angular distributions, for Zr, Nb, Mo, Hf, Ta, W; pure metal and He and D-T containing redeposited surfaces
- Electron impact ionization rate coefficients for sputtered atom and resulting impurity ions; misc. atomic and molecular processes
- Impurity/plasma velocity-changing collision coefficients (e.g. per Fokker Plank formalism; mass and charge state dependent)
- Self-sputtering coefficients for redeposited, sheath-accelerated ions
- Tritium trapping fractions in co-deposited material

These vary in their availability. They are most available for tungsten and molybdenum—due in obvious part to their use in present tokamaks—less so for the other materials. In spite of various uncertainties, however, our assessment shows that the key erosion/redeposition parameters for Zr, Nb and Mo are known to be, or likely to be similar (within factors of ~2), and likewise for Hf, Ta, W—at least for the pure metals. For example, Figure III.4 shows ITMC-DYN code [58] self-sputtering computations made for this study. The yields for the W-class materials, and for Mo, are practically identical, as is the case for Zr and Nb. The latter two elements are also seen to have a higher incident energy threshold for unity self-sputtering coefficient (due to atomic density and surface binding energy differences). This translates into a higher plasma edge temperature limit (determined primarily by sheath acceleration of multiply charged redeposited ions) to avoid runaway self-sputtering, although such limit is already adequate for tungsten, at Te ~50 eV, e.g. [57]. Available O, Ar, and other trace-material sputter yields for these candidate metals also show reasonable similarity, e.g. [59]. As a final example, Figure III.5 shows neutral atom electron ionization rate coefficients [60]. These rates are fairly close to each other, as well as to Mo and W rates (not shown), for the most relevant Te >10 eV range. We therefore make a detailed sputter performance computation for molybdenum and tungsten—this implies results for the other materials. We note, however, that this must be further studied for D-T and He containing, evolving, mixed-material surfaces.

The selected design for the erosion/redeposition analysis is the C-MOD outer divertor, with simulated fusion DEMO (or commercial) reactor-like edge plasma conditions. The analysis uses the geometry, magnetic field, and plasma profile data for a C-MOD tungsten divertor campaign [61], for two types of observed discharges, with peak Te at the strike point of 12 or 30 eV, these representing "low" and "high" temperature conditions respectively. We scale C-MOD plasma densities for these discharges by a factor of x10, giving divertor peak power loadings of ~5-10 MW/m^2. Also assumed is a D-T plasma with 5% Helium, with or without 0.1% Argon radiating material. (Such radiating material may be needed to control reactor heat loads. Use of other proposed radiating elements, e.g. Xe, would not change our conclusions). While not fully self-consistent, this model should reasonably capture the relevant erosion/redeposition conditions of a tokamak reactor divertor.

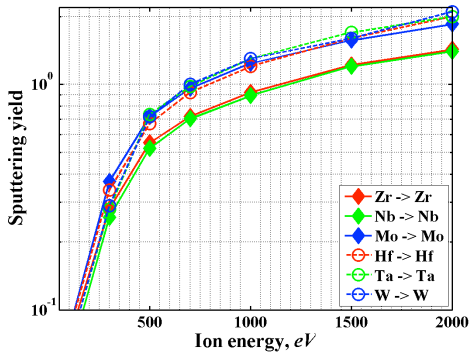

Figure III.4. Self-Sputtering comparison of candidate high-Z materials

ITMC-DYN calculations @ 25° incidence.

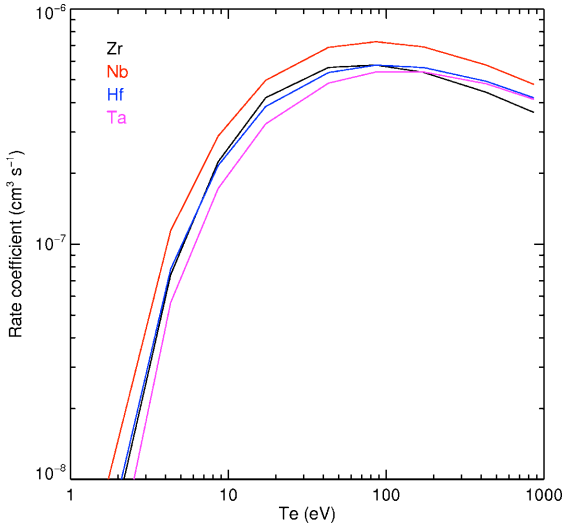

Figure III.5. Electron impact ionization of neutral-atom; rate coefficient comparison of various W-alternative plasma facing high-Z materials. ADAS data [60]

The analysis method follows that for a recent C-MOD tungsten campaign analysis [62]. We use the 3-D, fully kinetic, REDEP/WBC erosion/redeposition code package with ITMC code sputter yields/distributions, with inputs of divertor geometry, magnetic field, and edge/SOL plasma. The codes compute molybdenum and tungsten divertor sputtering—as stated from D, T, He, Ar, and self-sputtering—ionization, and subsequent transport of material due to Lorentz force motion, and plasma/impurity velocity-changing, and further charge-changing collisions.

Figure III.6 summarizes results in terms of peak net erosion rates. For tungsten, D-T ion sputter yields are below the sputter threshold for both temperature cases. (Charge exchange neutral sputtering is not included, due to lack of data, but would not have a significant effect on divertor erosion). Tungsten gross erosion is thus determined by argon ion impingement, if present, with some helium sputtering at the higher temperature case. For molybdenum, both Ar and He sputtering play the major role, with some D-T sputtering for the higher temperature case. For determining *net* erosion, the redeposition fractions depend on the incident particle mix, via sputtered energy distribution differences. This particle mix differs for Mo and W but redeposition is found to be high in any event. Another factor is that self-sputtering coefficients are higher for W than for Mo, offsetting, to some extent, lower W yields for other incident species. The peak net erosion rate varies from ~0-1.5 mm/burn-yr. A 5 mm coating would therefore last several operating years or more, from the sputtering standpoint. All things being equal, tungsten is seen to be preferred over molybdenum, but molybdenum is acceptable. Again, we expect zirconium and niobium performance to be reasonably similar to molybdenum, and likewise for hafnium and tantalum in relation to tungsten. Also, and critically for all cases, there is zero predicted core plasma contamination and negligible tritium co-deposition. Although core plasma contamination modeling is uncertain, the key point here is that contamination is unlikely to be very different for any of these high-Z materials.

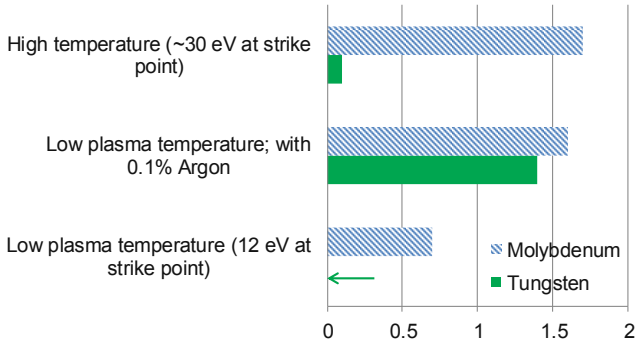

Figure III.6. Tungsten and molybdenum plasma facing material performance comparison; C-MOD tokamak outer divertor with simulated DEMO fusion reactor plasma conditions. Divertor peak net sputtering erosion rate. REDEP/WBC code package analysis

Summarizing, molybdenum and tungsten divertor surfaces do not have major predicted sputter erosion performance differences, viz. having high redeposition (~97% at strike point, ~100% for the overall divertor), order of 1 mm/burn-yr peak net erosion, and negligible core plasma contamination and tritium codeposition. Thus, all six of these candidates high-Z materials appear to offer acceptable sputter erosion/redeposition performance—in the simulated DEMO case studied—within existing margins of error. We also initiated an assessment of *first wall* sputter erosion/redeposition. Here, a controlling factor for a high-Z surface is the D-T charge exchange neutral wall-impingement energy spectrum in the roughly >400 eV range. In addition, plasma parameters at/near the wall, and plasma ion flow to the wall, in particular for turbulent edge plasma conditions, as well as the sheath potential and structure at the wall, are important but uncertain features. Study [63] with one type of turbulent edge plasma and sputtered wall-particle transport model, applied to ITER, showed a low net wall erosion rate for tungsten of ~0.05 mm/burn-yr, and no core plasma contamination. The erosion rate is about 20 times lower for a non-turbulent (diffusion-only) plasma edge [63]. Extrapolating to molybdenum, for the turbulent case, erosion is about 4 times higher than for tungsten. This still would permit an adequate sputter-determined lifetime; of order 5 years for a 1 mm Mo wall coating. An analysis of wall-sputtered Mo core plasma contamination is beyond our present scope—but does not appear likely to be much different than for W. The non-contamination is due to the long distance from the wall to the core plasma, collisions with the boundary plasma flowing to the various PFC surfaces, and the lack of a strong inward transport mechanism. However, this issue needs rigorous, detailed assessment, including re-assessment for tungsten, for a variety of plasma conditions and validated turbulent transport models, and ideally using coupled/codes and supercomputing, e.g. as suggested in [63, 64].

Damage to plasma facing components during abnormal events remains one of the most serious concerns for safe, successful, and reliable tokamak reactor operation. Plasma instabilities occur in various forms such as disruptions, which includes both thermal and current quench, Edge Localized Modes (ELMs), runaway electrons (RE), and Vertical Displacement Events (VDEs). These can result in partial or complete loss of plasma confinement, with resulting high or very high heat and particle loads. The HEIGHTS transient response simulation package has been used for several decades, with continuous improvements, to investigate in great detail the effect of plasma instabilities on plasma facing components of a tokamak reactor [65]. The 3-D integrated HEIGHTS model combines four main parts: energy deposition, target hydrodynamic evolution, radiation transport and energy dissipation (with both heat conduction and magnetic diffusion). HEIGHTS follows various stages of plasma evolution and materials interactions in the plasma and scrape-off-layer, up to the transport of the eroded debris and splashed target materials as a result of the deposited energy.

Plasma instabilities will have varied effects on both plasma-facing materials and the underlying structural materials. The main consequences of ELMs and disruptions are erosion of PFC surface layers from evaporation and splashing of melted layers; heating and evaporation of nearby components by intense radiation from the developed divertor vapor-plasma; and core plasma contamination by eroded materials [65]. No damage is expected to the structural materials of the divertor because of the short duration of these two events. All materials examined (C, Be, W in particular) show serious issues. Disruptions and ELMs will mainly affect the divertor plate. Runaway electrons and VDEs could affect parts of the first wall coating as well as the underlying structural materials. For longer plasma instabilities such as VDEs, or for deeper energy deposition as in the RE case, high-Z wall materials are preferred to protect the coolant channels, since most of the energy will be absorbed near the surface and most damage will then occur to the coating rather than the structure [65, 66].

In particular, for tungsten, issues include melt layer formation and loss from "Giant ELM's" and disruptions [65-67]. However, it is encouraging that acceptable ELM etc. parameter windows exist for tungsten, per HEIGHTS code package analysis, although these could limit core-plasma operating space [66, 68]. A typical example of divertor surface erosion profiles during a disruption, shown in Figure III.7, is a result of the products of three time-dependent processes: direct impact energy deposition through the evolving divertor plasma/vapor cloud; secondary radiation of the hot plasma cloud; and heat conduction inside the divertor plate. Transient response analysis for the alternative materials shows similar trends during the intense transient-plasma power deposition, with some differences in the magnitude of melt layer thickness and erosion rates due to differences in thermophysical properties among these materials.

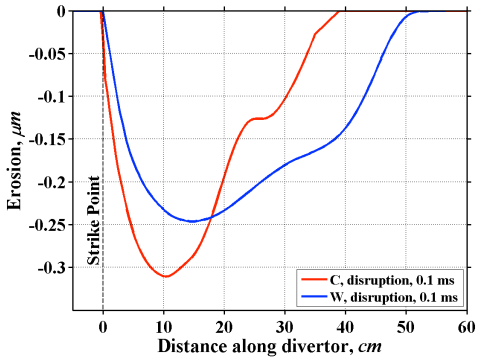

Figure III.7. Divertor surface erosion profile after the impact of a disruption; W and C surfaces; ITER divertor. HEIGHTS code package analysis. Erosion due to vaporization is not strongly material-dependent.

For example, based on our initial estimation, erosion of tantalum is predicted to be higher than tungsten. Tantalum has similar boiling characteristics as tungsten but much lower thermal conductivity. A higher evaporation rate is also expected for hafnium plasma facing material. Compared to tungsten, hafnium has a lower boiling point, heat of vaporization, and thermal conductivity. Molybdenum, in contrast, has comparable thermal conductivity to tungsten, and a higher heat of vaporization, and is expected to have slightly less evaporation but more melting. Therefore, erosion of molybdenum from melt-layer splashing can be higher than tungsten since a thicker melt layer could be developed. Other materials, such as niobium and zirconium, should more or less behave similarly to molybdenum.

Plasma transient events with longer energy loads, which correspond to VDE's or RE time spans of 10's of ms, and with their longer energy deposition range, could have severe effects on the structural materials and coolant tubes. The high thermal conductivity of tungsten and molybdenum surface materials can result in significant heating of the structural materials and can even cause melting of the structure and burnout of coolant tubes [22]. Material response due to runaway electrons also depends on the atomic number of the material [69]. High-Z tungsten will absorb RE energy near the surface layers

that can cause melting of the surface [70]. Lower-Z coatings such as Be and C could result in deeper RE penetration to the bulk that will cause heating of the structural materials and could increase risk of damage to coolant tubes depending on the RE energies. The high-Z alternative materials, as with tungsten, should be superior in this regard to beryllium and carbon.

For all materials, ongoing, detailed, integrated analysis of incident core plasma particle and energy distributions during various transient events is required to predict safe operating regimes and to determine proper requirements for mitigating techniques. The radiation properties and plasma opacities of the developed divertor vapor-shielding layer must also be assessed to determine the damage potential to the surrounding surfaces. This will require detailed consideration of opacity, line and recombination radiation, and related data/modelling for the alternative high-Z materials. To summarize the key point, plasma facing material response to plasma transients is a serious issue for tungsten, but acceptable plasma operational windows (e.g. for ELM duration/energy), appear to exist. Based on our initial analysis, there will be differences in the degree of response, and operating windows, for the alternative plasma facing materials, but there does not appear to be fundamental differences. However, issues such as degree of melt splashing, and radiation exposure to secondary nearby components, could differ significantly among various higher Z materials. Major modelling work and supporting experiments on transient response is clearly needed for fusion progress, for any of these materials.

A concern for some materials is hydride formation and associated coating integrity and tritium inventory. While requiring detailed study, we briefly note that hydride formation might be completely avoidable through proper choice of operating temperature. For tantalum, Ref. [71] reports essentially zero H/Ta content for > 873K — a modest temperature requirement under high-power loading. Also, tritium inventory, even with hydride formation, may be acceptable for a thin divertor coating. For example, for a 50 m^2 area divertor (such as the ITER outer divertor design), 1 mm thick Ta coating, 0.13 H/Ta hydride ratio per Ref. [71] results at 823K, and 50% T plasma, the Ta surface would contain about 1 Kg tritium in hydride form—a non-trivial but acceptable amount. In addition, the performance and microstructure evolution of different PFC materials during both normal and transient operation is very important in choosing the overall best material for the divertor design. Formation of fuzz like structures etc., seen on tungsten and molybdenum materials in some laboratory experiments, could be serious in terms of plasma contamination and erosion lifetime. This issue needs to be studied for all the proposed high-Z materials.

This identification and initial analysis of alternative high-Z plasma facing materials is encouraging showing: 1) environmentally attractive activation, with minimal or no waste disposal, for a commercial power plant divertor surface, using advanced recycling equipment, 2) acceptable sputtering erosion/redeposition performance, similar to a tungsten divertor, and 3) concerns about the transient response of the alternative materials but not fundamentally different than concerns for tungsten. This potentially expands the list of candidate solid high-Z facing materials from basically one (tungsten) to six, and could therefore provide a major design margin for future fusion reactors, against failure of any one material. This study is a start; considerable work is needed to advance the qualification of these alternative materials (and generally for tungsten as well) for divertor and first wall applications. Such work includes modeling, design, and supporting experiments for: a) plasma facing component sputtering and transient response for irradiated/evolving redeposited mixed material; b) surface temperature operating windows; c) possible helium effects, d) bonding and related thermo/mechanical issues, e) dust issues, and f) plasma edge solution variation effects on overall performance. We encourage fusion community interest in further studying these candidate materials.

IV. Support of DIII-D Tokamak Plasma/Surface Interaction Experiments

We analyze a DIII-D tokamak experiment where two tungsten spots on the removable DiMES divertor probe were exposed to 12 seconds of attached plasma conditions, with moderate strike point temperature and density (~20 eV, ~4.5×10^{19} m^{-3}), and high carbon impurity content (~3%). "Small" (1 mm diameter) and "large" (1 cm dia.) deposited samples were used for assessing gross and net tungsten

sputtering erosion. The analysis uses a 3-D erosion/redeposition code package (REDEP/WBC), with input from a diagnostic-calibrated near-surface plasma code (OEDGE), and with focus on charge state resolved impinging carbon ion flux and energy. The tungsten surfaces are primarily sputtered by the carbon, in charge states +1 to +4. We predict high redeposition (~75%) of sputtered tungsten on the 1 cm spot — with consequent reduced net erosion—and this agrees well with post-exposure DiMES probe RBS analysis data. This study and recent related work is encouraging for erosion lifetime and non-contamination performance of tokamak reactor high-Z plasma facing components.

Plasma facing component (PFC) sputtering erosion is a critical issue for fusion power. The General Atomics DIII-D tokamak with the Divertor Material Evaluation System (DiMES) manipulator probe [72] is a valuable facility for erosion/redeposition experiments and code validation, in particular due to enabling short duration (~1-5 plasma shots) controlled test surface exposures, with well diagnosed near-surface plasmas, and with post plasma exposure DiMES sample analysis capabilities at SNL Albuquerque. Accordingly, there has been a long history of modeling/analysis of DIII-D/DiMES sputtering/erosion experiments, with numerous surface materials and plasma conditions, e.g. [73].

A current worldwide fusion research focus is high-Z material PFC surfaces. Recent studies at DIII-D have examined molybdenum test sample sputtering and resulting Mo transport and Mo/C mixing [74-76]. A DIII-D/DiMES experiment with tungsten on a carbon substrate was also performed [76]. In terms of other devices, Ref. [62] analyzed a long-exposure campaign at C-MOD using a tungsten strip divertor. These and other analysis efforts, e.g. for ASDEX-U [77], and ITER [68], generally predict negligible high-Z material sputtering by the main hydrogen isotope plasma, predominant sputtering by plasma impurities (e.g. carbon in DII-D; boron in C-MOD; helium, beryllium etc. in ITER), high redeposition rates, and resulting low net erosion rates. Such performance is in fact critically needed for ITER, where only very low plasma contamination by sputtered tungsten can be tolerated, and for DEMO and commercial fusion reactors where, additionally, multi-year sputter erosion *lifetime* of PFC's is required. Continued experiments, simulation, and code/data validation of sputter erosion/redeposition, is thus a major need for fusion power research.

The DiMES-61 experiment [78] analyzed here had the attractive features of moderate near-surface plasma density and temperature, and high plasma carbon impurity content, with resulting well-measurable tungsten sputtering erosion. The experiment used the two-spot deposited metal technique, where a very small—in relation to sputtered particle transport distances—1 mm diameter spot is expected to have low redeposition of sputtered material, and thus permits a good measure of *gross* erosion, and where a larger 1 cm spot has higher redeposition, enabling code/data comparisons of the *net/gross* erosion ratio. Also, in contrast to other experiments, the DiMES-61 tungsten films were deposited on a molybdenum inter-layer, reducing complications from near-spot high-Z/low-Z material (W/C) surface mixing.

This work reports on analysis of the DiMES-61 tungsten samples gross and net erosion. Other issues for this experiment such as erosion of Mo, W/Mo mixing, and off sample W transport, remain subjects for future modeling. Although there are concerns about uncertainties in the plasma conditions we find good code/data agreement for the tungsten erosion. This adds to the confidence about predictions of acceptable sputter erosion/redeposition performance for future high-Z PFC's.

Figure IV.1 shows the DiMES-61 probe surface. The test sample was prepared by magnetron sputter deposition of Mo and W films onto a 25 mm diameter Si disk at Sandia National Laboratories. The W was deposited as 1 cm and 1 mm diameter W films, both ~30 nm thick. The purpose of the smaller spot was to obtain non-spectroscopic measurement of the gross erosion of W [74]. (A 1 mm diameter spot in the middle of the 1 cm sample was left uncoated by W in order to measure gross erosion of Mo. This does not materially affect the present analysis.) Unlike a previous experiment [76], where a carbon inter-layer was used to mask the Si substrate, this time a 20 nm thick Mo inter-layer was used in order to investigate a different set of mixed material effects. The sample was installed in a graphite casing ~5 cm in diameter and inserted in the lower divertor of the DIII-D tokamak using the DiMES manipulator. During the exposure, the plasma-facing side of the sample was level with the divertor tile surface within 0.1 mm.

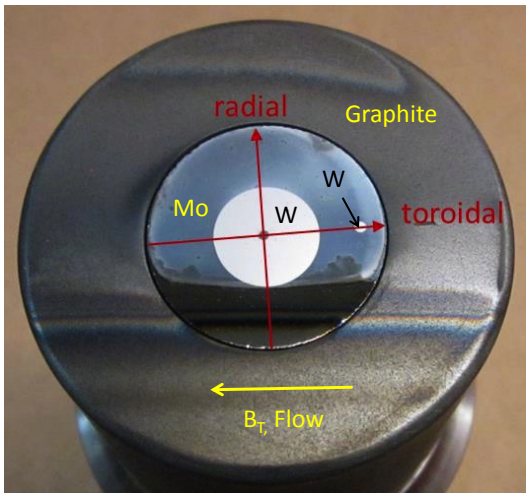

Figure IV.1. DiMES-61 5 cm diameter probe containing 1 cm and 1 mm diameter tungsten spots deposited over a molybdenum inter-layer on a silicon substrate. (Central 1 cm spot has a 1 mm dia. non-coating)

The probe was exposed to three deuterium plasma discharges, in a lower single null magnetic configuration (see Fig. 1(b) in [76] for the magnetic configuration and diagnostic arrangement). The outer strike point was moved to the inboard edge of the DiMES sample once stable plasma conditions were achieved, and kept there for ~4 s in each exposure discharge, giving a total exposure time of ~12 s. Discharges with reversed (counter-clockwise when seen from above) toroidal field (B_T) were used, allowing injection of 2.9 MW neutral beam heating power without transitioning into H-mode (thus avoiding a complicating effect of ELMs). Plasma flow to the divertor plates was toroidally co-directed with B_T (from right to left in Fig. IV.1). As in previous experiments the 1 mm spot was located upstream of the 1 cm spot to minimize deposition of W eroded from the larger spot on the smaller one. Local electron density (n_e) and temperature (T_e) at the major radius of the sample were measured by the divertor Langmuir probes and Thomson scattering system. WI and MoI emission from the sample region was monitored by an absolutely calibrated digital CMOS camera and a high resolution MDS spectrometer.
Net erosion and deposition was determined by measuring the areal density of the W before and after exposure to the plasma, using Rutherford backscattering spectroscopy (RBS) with 2 MeV He^4. (In addition, erosion of Mo by RBS, and coverage of deuterium and carbon by He^3 nuclear reaction analysis (NRA) was measured, as further described in [78].)

We used the process of empirical plasma reconstruction using the OEDGE and EIRENE codes [79, 80] to determine the plasma conditions at the outer divertor which best matched the available diagnostics. These diagnostics are Langmuir probe measurements of saturation current (J_{sat}) and T_e; Thomson scattering measurements of T_e and n_e, both at the divertor and upstream; as well as some limited hydrogen and carbon spectroscopic measurements. Empirical plasma reconstruction uses the diagnostic measurements of J_{sat} and T_e across the target as input boundary conditions to the 1-D, parallel to the field line, OEDGE plasma solver or Onion Skin Model (OSM). The OEDGE code then calculates the plasma conditions (n_e, T_e, ion temperature (T_i), parallel plasma flow speed ($v_{||}$), and parallel electric field) along the field lines on the computational mesh, using the experimental boundary conditions at the target as input, and usually making the following additional assumptions; that $v||=c_s$ (sound speed) at the target, and $T_i=T_e$ at the target. Toroidal symmetry of the plasma parameters is also assumed. The hydrogenic terms used in the plasma solver, typically ionization density, neutral density and energy loss terms, are calculated by the EIRENE code using the initial plasma solution from the OSM. The OSM is then run

iteratively with EIRENE until convergence of the calculated plasma values. The resulting 2-D plasma values, in the poloidal plane, are then supplied as input to the REDEP/WBC code package.

The target plasma conditions used for the tungsten erosion modeling across DIMES are shown in Figure IV.2. Initial plasma solutions using the T_e values measured by the Langmuir probes did not agree well with the Thomson measurements. Since the J_{sat} measurement is considered more reliable than the probe T_e measurement, the J_{sat} was left fixed while the target temperature was adjusted to obtain a better match between the calculated plasma and the other diagnostic measurements. Setting the target temperatures equal to 0.5 x the Langmuir probe temperatures provided better agreement with both the divertor and upstream Thomson measurements. Spectroscopic measurements of D_α were consistent with both T_e cases examined since the hydrogen emission coefficients are only weakly dependent on temperature in this range.

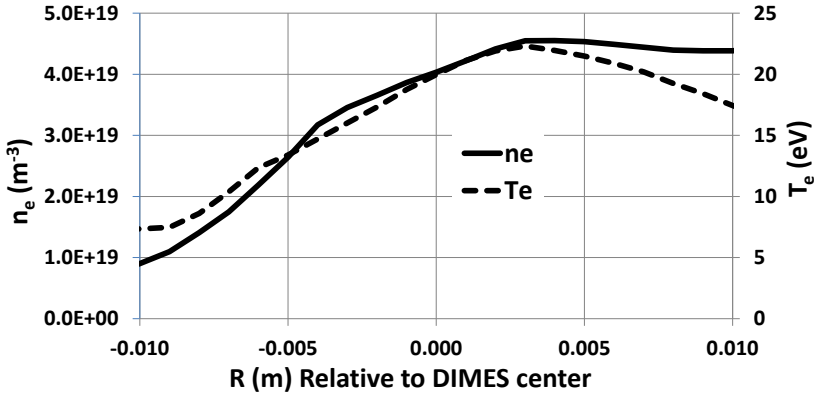

Figure IV.2. Plasma electron density and temperature radial profiles, at the target, along the inner 2 cm of the DiMES probe. ODEGE/EIRENE calculation.

In DIII-D the primary impurity species is carbon. Using the background plasma solution developed the impurity tracking portion of OEDGE (DIVIMP code) was used to model the large-scale carbon impurity production, transport and deposition. Carbon impurities are calculated at surfaces where plasma interactions cause both physical and chemical sputtering. All carbon particles launched were followed until deposited on surfaces, and the local flux and average energy at deposition were recorded. The carbon calculation results are summarized in Figure IV.3 for the DiMES region. The total carbon ion flux is found to be ~3% of the deuterium ion flux. CIII-4650A emissions measured at the target and calculated in the simulation agree within a factor of two, though the simulation is higher than the measured values. Low charge states of carbon dominate the flux. Physically sputtered carbon is responsible for about 1/2 of the $C3^+$ arriving at DIMES despite being a much smaller source of particles in the simulation. The average impact energies for both physical and chemically sputtered carbon are comparable since sheath acceleration is the dominant contribution to the carbon ion energies. The carbon neutral flux is very small and with low impact

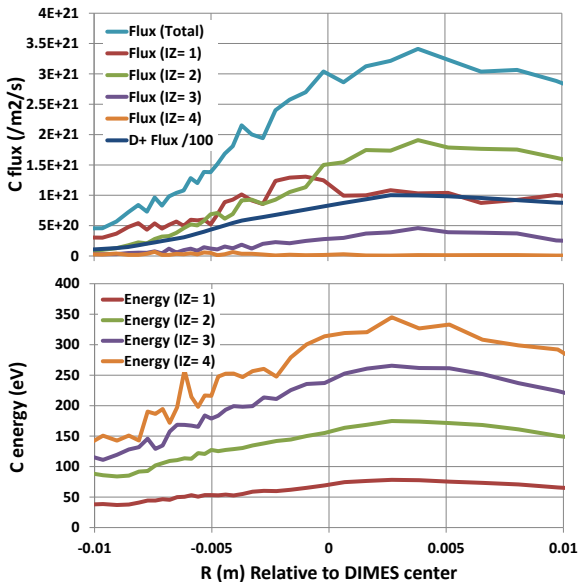

Figure IV.3. Carbon ion flux and average impact energy, per charge state, along the inner 2 cm of the DiMES probe. ODEGE/EIRENE calculation.

energy, such that the effect of carbon neutrals on tungsten erosion is negligible.

The 3-D, full kinetic, Monte Carlo, REDEP/WBC code package was used to model sputtering of the deposited tungsten spots, redeposition on the spots, and resulting gross and net W erosion. The general simulation technique is described in e.g. [57]. Briefly, the package computes the sputtering and transport of plasma facing surface atoms; ionization and resulting impurity ion transport due to velocity-changing and charge-changing collisions with the background plasma, and sub-gyro-orbit Lorentz force motion including detailed sheath effects; and resulting redeposition and self-sputtering. Inputs to the code package for this analysis are the above- described empirical plasma reconstruction 2-D plasma solution, with impinging carbon ion flux and energy profiles; magnetic field data; and DiMES probe and divertor geometry. Tungsten sputter yields and sputtered atom angular and energy distributions for D, C, and self-sputtering, were supplied by ITMC-DYN code [58] calculations, over the relevant energy range and incident angles for the respective incident particles.

We also used REDEP/WBC simulations to estimate the effect of DiMES-61 Mo sputtering and transport on sputtering of the W spots. For the plasma solution used, such W sputtering by Mo appears insignificant. Although certain other *mixed-material* effects were modeled for a recent DiMES experiment using molybdenum deposits on a carbon substrate [75], analysis of mixing and re-sputtering of transported tungsten in the Mo and C portions of the DiMES-61 probe was not done here, since this is not critical for the present purpose of computing W spot erosion only. Future work could productively assess these mixed-material effects and other aspects of the DiMES-61 experiment, resources permitting. Various REDEP/WBC redeposition parameters, spot-average erosion values, erosion profiles, and code/data comparisons are shown in Tables IV.1-IV.2, and Figures IV.4 -IV.5. The simulation shows zero sputtering of tungsten by the main plasma deuterium content, with incident D^+ energies below the W sputtering threshold. Tungsten erosion is thus due to the carbon plasma content with carbon ion charge states +1 to +3 dominating. For the 1 cm spot there is also a small (~4%) self-sputtering contribution. For the 1 mm spot self-sputtering is insignificant (≤1%) because of low redeposition.

Table IV.1. REDEP/WBC simulation of DiMES-61 experiment of 5/10/13; erosion/redeposition parameter summary for the 10 mm diameter tungsten spot. Values for the 1 mm dia. spot are similar.

Parameter	Tungsten 10 mm spot
Average sputtered energy, eV	11
Mean-free-path for sputtered atom ionization (normal to surface), mm	.51
Transit time* (ionization-to-redeposition), μs	.69
Charge state*	1.8
Energy*, eV	97 (85**)
Elevation angle*, degrees (from normal)	17
Self-sputtering coefficient*	.058

* average for redeposited tungsten ions on the spot

** standard deviation

Table IV.2. DiMES-61 probe tungsten samples average erosion summary and code/data comparison.

Parameter*	1 mm spot	10 mm spot
Gross erosion rate, nm/s	1.90	1.92
Redeposition fraction; on spot	.193	.742
Net erosion rate, nm/s	1.49	.496
Net erosion after 12 s plasma exposure, nm	**17.9 code** **10.5 data**	**5.9 code** **4.0 data**

Per Table IV.1, most sputtered W atoms are ionized within the magnetic sheath, with mean free paths of ~0.5 mm, comparable to the magnetic sheath width of order 1 mm (~3 x the D^+ ion gyroradius). Redeposition of the resulting W ions occurs due in part to the strong sheath electric field, with collisional friction with the incoming plasma and gyromotion effects also important. Redeposited W ions impact the surface at near normal incidence, at low charge states and fairly low resulting energy. Redeposition for the 1 cm spot is high at ~75%, thus implying an average gross to net erosion ratio of about 4. Even for the very small 1 mm spot there is a non-trivial redeposition fraction of about 20%. (The latter redeposition fraction is higher than for previous experiments due to the higher plasma density for DiMES-61.) As shown in Table IV.2, the predicted net erosion values for both spots, for the 12 s exposure time, averaged over the respective spot area, agrees within a factor of two with the RBS laboratory data. (The *very close* agreement for the 1 cm spot is possibly fortuitous considering various error bars—we consider anything within a factor of two to be an acceptable code/data match for validation purposes). Figures IV.4-IV.5 shows the code/data comparison of the net eroded tungsten profile for the 1 cm spot for both a toroidal and radial scan, through the spot center. The comparisons show reasonable quantitative and qualitative agreement, but with some discrepancy for the outer radial scan.

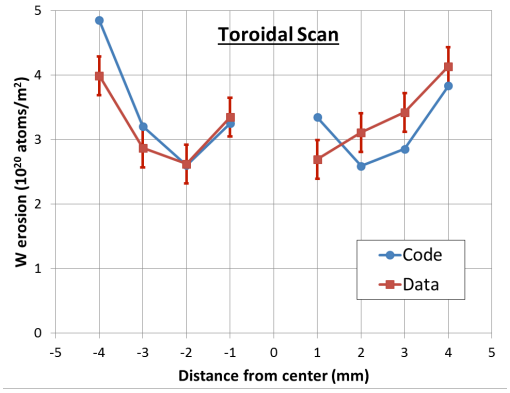

Figure IV.4. Net erosion profile along the DiMES-61 probe 1 cm tungsten spot; toroidal direction through spot center. REDEP/WBC-OEDGE/EIRENE simulation ("Code") vs. post-exposure RBS data

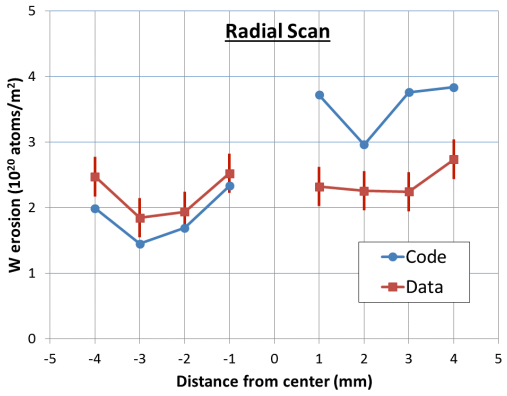

Figure IV.5. Net erosion profile along the DiMES-61 probe 1 cm tungsten spot; radial direction through spot center. REDEP/WBC-OEDGE/EIRENE simulation ("Code") vs. post-exposure RBS data

Summarizing the results in terms of the 1 cm spot *net to gross erosion ratio*, the simulation ratio is **0.26**. Due to the significant radial variation in carbon ion sputtering, and the non-zero 1 mm spot redeposition, there is some issue for this experiment in using the 1 mm erosion data as a pure measure of the large spot gross erosion, unlike for previous DiMES experiments. However, using some modest modeling-based assumptions/adjustments for the 1 mm spot data, (e.g. to account for the small spot redeposition fluence), the data-inferred net/gross erosion ratio is **0.29**. We thus have code/data validation for this important summary parameter. A final key analysis prediction is that no sputtered tungsten enters the core plasma, due to intense redeposition—as mentioned on the samples themselves, or somewhere on the probe/divertor. The DIII-D spectroscopic data for this experiment, in fact, shows no core plasma tungsten, however, the diagnostic sensitivity is below the detection limit for this limited-area erosion source.

Extrapolating the present results and previous DiMES studies to a tokamak fusion reactor, the relatively high redeposition fraction of ~75% for the quite small 1 cm dia. circular deposit implies a near 100% expected local redeposition for a continuous tungsten divertor surface, for similar plasma edge conditions, and clearly for the higher expected plasma densities in ITER and future reactors. Considering this and other tokamak analysis, e.g. [62], we have developed reasonable confidence in the basic picture of tungsten PFC sputtering—by plasma impurities only, with high redeposition of sputtered material and resulting very low net erosion, and with little or no core plasma contamination. In spite of the positive results to date a fully validated, predictive analysis of the critical plasma material interaction (PMI) response—for complete analysis of DIII-D etc. material erosion, transport, mixing, and self-consistent plasma response—will require improvements to plasma diagnostics and continuing experimental innovations, as well as use of advanced modeling/simulation tools, such as a fully coupled petascale computing PMI package, e.g. as discussed in [64].

Summary

We have developed multidimensional comprehensive models for extensive and integrated simulation of the evolved divertor/edge plasma during plasma instabilities and its self-consistent evolution in the entire SOL area with prediction of heat loads and erosion profiles on all nearby component surfaces. An important part of the upgraded HEIGHTS integrated package, i.e., radiation spectra with fine details and transport is developed and presented. Based on weighted Monte Carlo algorithms, the developed radiation transport module allowed full 3D simulations of radiation fluxes in the entire SOL area with detailed analysis of divertor spatial configuration (regions of interest). In coupling with the earlier developed

kinetic models of the escaping core plasma [26], the radiation transport model was used for the simulation of giant ELM and disruption in the current design of ITER device [47]. Detail surfaces thermal response due to radiation from the evolved divertor plasma was extensively modeled and analyzed. Calculation results are found to be in agreement with previous studies [18] regarding the significant increase of radiation fluxes and damage to divertor nearby components during disruptions. For the same core plasma impact energy, the radiation fluxes increase with the atomic number of the divertor material. Detailed radiation spectra and comparison of the emitted radiation fluxes of carbon and tungsten as divertor plate materials are calculated and analyzed. During a disruption on tungsten divertor plate significant damage was predicted to the open stainless steel legs of the dome structure in the current ITER design. Current ITER design should be modified to mitigate such effects.

We analyzed the erosion and transport of pre-deposited tungsten on a DiMES probe in the DIII-divertor using codes for the plasma background, erosion/redeposition, and sputter response. The simulation predicts an average net erosion rate, for a tungsten 1 cm dia. circular sample, of 5.9 nm after 12 s plasma exposures, similar to the data value of 4.0 nm, and with likewise reasonable agreement between code/data in-spot spatial erosion profiles. There is also good agreement for the net to gross erosion ratio of ~0.26, and related metrics. The important/general finding is the qualitative picture that redeposition significantly reduces the net erosion—as found by the present modeling and shown by the data. Since planned ITER divertor operating conditions appear fairly similar to this experiment—for plasma parameters, oblique incidence magnetic field geometry, and impurity flux (although with different expected impurity species)—the present results and related work have favorable implications for such future high-Z material divertor performance.

In view of the very successful DiMES series of experiments, and the substantial benefit to code validation, a major continued research program for DIII-D/DiMES is highly recommended. Among candidate research work is the use of DiMES to study different high-Z materials, different plasma conditions (e.g. to determine T_e operating limit to avoid self-sputtering runaway, radiative plasma with Ar, Xe, etc.), mixed materials (e.g. Be/W), and pre-irradiated materials (e.g. D and He exposed W with resulting surface ultrastructure).

V. Macroscopic Melt Layer Splashing and Losses

Introduction. Melting of metallic plasma facing components (PFC) such as tungsten (W) divertor, macroscopic melt motion, and melt splashing due to edge localized modes (ELMs) and plasma disruptions are important issues in fusion devices such as ITER. Under these off-normal transient events [81, 82], the high thermal energy can be deposited on localized areas of PFC [83, 84]. Among high-Z materials, pure W demonstrates the highest resistance against thermal loads under plasma disruption conditions [85]. It has high thermal conductivity, high melting point, and low sputtering [86]. It has been evaluated as a plasma-facing material for divertor plates in steady state magnetic fusion devices [85]. However, a critical problem with W is melting under intense thermal loads, melt layer formation, macroscopic melt motion, and splashing with ejection of melt droplets into a plasma [87-95]. The macroscopic melt motion and splashing due to plasma pressure or Lorentz force can cause severe erosion and unacceptable short lifetime of PFCs [96]. This also leads to plasma contamination by high-Z material and significant damage of PFCs. Approximately 15 g of molten W was lost from the tile in the outer divertor of Alcator C-Mod during ~100 discharges [97]. In the experiments carried out in the plasma edge of the TEXTOR tokamak, up to 3 g of molten W were redistributed forming mountain-like structures at the edge of the sample [98]. The ejection of molten W into the plasma core can further lead to significant plasma contamination and termination of tokamak plasma discharge [99]. Therefore, it is important to understand the physical mechanisms of macroscopic melt losses and possible ways of their mitigation.

Macroscopic melt motion and splashing with ejection of molten droplets into plasma are major concern in fusion devices. Melt motion and droplet ejection has been observed in the experiments carried out in TEXTOR tokamak [100-102], numerous plasma guns [103-113], and electron beam facilities [114].

Up-to-date, the W exposures to a hot plasma in the tokamaks have simulated steady state deep melting, although the transient melt exposures have been performed at JET in 2013. The plasma gun devices have been also used to study the transient shallow melting. Shallow melting is of particular interest for ITER and future reactors, since ELMs and disruptions are the most likely candidates for melting the surfaces. The disruption conditions in tokamaks cannot be always reproduced using the simulation devices. Although the relevant energy density can be achieved, other parameters such as pulse duration and particle energy can considerably differ in various devices [115]. Many facilities do not include the effects of a magnetic field. Therefore, the results of experimental studies in simulation devices should be carefully interpreted. Fine spray of W-melt is observed in recent TEXTOR experiments and was constantly present having W-melt macroscopic losses as splashes with continuous ligaments and large droplets [98, 116, 117]. The emission of fine melt spray was attributed to melt boiling with bubble bursting [118], while melt splashes with droplets are due to the development of Kelvin-Helmholtz instability [119]. A considerable amount of the melt layer can be swept away from the melt pool due to the melt motion under the plasma impact and external electromagnetic forces [108, 114]. The ejected molten material can accumulate at the pool's edge and splash out further resolidifying on the solid surface [113]. The formation of erosion crater and melt motion was studied using the QSPA Kh-50 plasma accelerator [106]. Large mountains of resolidified material are observed at the crater's edge. Long melt ligaments with breaking droplets at the ends were formed on the unexposed surface due to the melt outflow from the hills. It was concluded that the macroscopic motion of melt was driven by the plasma pressure gradient [106]. The formation of melt layer and its motion in the magnetic field was investigated in TEXTOR [101]. It was observed that the molten W has moved in the poloidal direction perpendicular to the magnetic field lines [100]. A deep erosion crater was developed with depth increasing poloidally up to 1 mm. A large blob of molten W was formed at the edge of W plate with two jets of width ~3 mm. These jets of molten W were splashed out on the plate within a distance of about 5 cm. The melt motion was attributed to the Lorentz force [101]. These experimental results demonstrate that the melt motion can lead to significant redistribution of PFC material during ELMs and disruptions.

Plasma disruption with energy deposition of ~10 MJ/m^2 during ~1 ms can result in a melt layer with depth ~100-200 μm [84]. It was predicted that only a few microns of melt is evaporated [83, 89]. For W target exposed to a plasma impact with an energy density ~30 MJ/m^2 during ~0.36 ms, W losses due to vaporization are less than ~1 μm [118]. The main theoretical approaches used to study the melt motion and splashing are the linear stability analysis [93, 94, 120, 121] and computational modeling [92, 119, 121-123]. The conditions for development and growth of surface waves at the plasma-melt interface were predicted using the inviscid stability analysis [119, 120, 123]. In agreement with these predictions, the growth of surface disturbances and their transformation into long W-melt ligaments that disintegrated into liquid droplets was observed using comprehensive modeling [119, 123]. The inviscid stability analysis [119, 120] was further extended to include the effects of viscosity, heat transfer, and mass exchange across the interface [121]. It is found that plasma viscosity has a destabilizing effect on melt layer. The surface waves with fastest growing rate have shifted toward shorter wavelengths with the critical velocity is greatly reduced. However, in this viscous stability analysis the short-length waves were stabilized by heat and mass transfer across the melt interface. The computational model [121] that includes heat transfer and vaporization effects was also developed implementing the open-source OpenFoam libraries [124]. The development of short waves with fine melt droplets stripped from wave tips and dragged away by the plasma flow is observed in the absence of melt evaporation. In the presence of phase change at the interface, it is found that unstable waves are suppressed due to melt evaporation [121].

During the past performance period on this project, the volume of fluid (VoF) model [125, 126] was coupled with magneto-hydrodynamic (MHD) model [127] in order to investigate the behavior of W-melt flow on a flat substrate [128], melt motion from a pool [129], splashing, and droplet ejection under ITER-relevant conditions. Both the viscous stability analysis and VoF-MHD modeling of coupled W-melt-plasma flows are performed. The viscous stability analysis was used to calculate the critical velocity and growth rate of waves on the W-melt surface as a function of wavelength. The onset of instability, critical plasma velocity, development and growth of dangerous waves are predicted. The effects of plasma

velocity and magnetic field, whether parallel or perpendicular to the direction of W-melt flow, on melt motion and splashing on a flat substrate and from a melt pool are studied using the VoF-MHD model. The motion of melt with velocity of ~1.7 m/s was observed in TEXTOR experiments [130]. Therefore, we use the velocity of W-melt ~2 m/s. The plasma flow velocity is uncertain. During ELMs in the DIII-D tokamak, the ELM plasma velocity is found to be ~0.5 km/s in the poloidal direction and ~10-20 km/s in the toroidal direction [131]. Higher plasma speeds are expected during plasma disruptions. Plasma gun compressors and accelerators can generate plasma streams with speeds higher than ~100-400 km/s [132, 133]. Therefore, the main purpose of this research was to investigate how the viscous plasma with increasing speed from 0 km/s to 5 km/s induces the development of waves on the melt surface, their growth, melt splashing and ejection of molten droplets. The volume of fluid fractions of melt and plasma, the distributions of pressure, velocity and magnetic field are reported. The distributions of hydrodynamic and magnetic pressure as well as the vector fields of velocity and magnetic field are investigated. The VoF-MHD modeling is also performed to investigate the motion and outflow of W-melt from the melt pool [129]. This research was an extension of the previous study on the motion and splashing of melt layers on solid substrates [128]. The impact of plasma flowing with different velocity on the development of waves on the W-melt pool surface is studied. The influence of a parallel or perpendicular magnetic field on the melt layer motion and splashing from a pool is investigated.

Development of running waves with large wavelengths is observed on the melt surface in the absence of plasma impact [128]. The magnetic field of 5 T that is parallel to the direction of melt motion completely damps these surface waves. When the magnetic field is perpendicular to the direction of melt motion, the small-amplitude standing waves are formed. The viscous plasma streaming with ~0.1-5 km/s over the melt surface develops waves that are not damped by the magnetic field which is either parallel or normal to the direction of melt motion. It is observed that the surface waves are generated much faster at higher plasma speeds and their wavelength decreases accordingly. The high-speed viscous plasma flowing with ~5 km/s produces small melt ripples that break up into droplets carried away by the plasma wind [128]. This is a major concern for magnetic fusion as a reliable source of energy production. The development of waves with certain wavelengths on the W-melt pool and formation of W-melt blob on the pool's edge are also observed in the absence and presence of an external magnetic field [129]. For the investigated speeds of viscous plasma, the parallel magnetic field of 5 T doesn't suppress W-melt motion and splashing from the pool, plasma-induced surface waves, and ejection of molten droplets. However, the Lorentz force induced by a perpendicular magnetic field accelerates the splashing of W-melt from a melt pool but only when the stream of viscous plasma becomes well coupled to the melt motion. Under the plasma impact with high velocity of ~5000 m/s, the W-melt doesn't undergo a significant motion disintegrating quickly into droplets dragged away by the plasma wind, independent of the presence or absence of a magnetic field [129]. This magnitude of plasma velocity is found to be in good agreement with that predicted by the viscous stability analysis.

Developed mathematical and computational models: We describe the viscous stability theory and VoF-MHD computational model developed to study the motion and splashing of melt layers from PFCs. The stability analysis provides an assessment of initial conditions for development and growth of surface waves, growth rates, and most dangerous wavelengths. The modeling predicts melt layer motion, plasma-melt interaction, and non-linear wave growth with ejection of molten droplets.

Viscous stability analysis In the majority of linear stability analyses conducted with potential flow, the fluids are usually considered as inviscid [119, 123, 134]. The theory of inviscid stability of tungsten and aluminum melts and the capillary droplet-ejection model as its limiting case have been recently developed by our group [120]. However, the plasma viscosity can also affect the melt stability within a narrow boundary layer at the interface between the plasma and melt. The theory of potential flow of inviscid plasma should be replaced with that of viscous plasma. The Kelvin-Helmholtz (K-H) instability of stratified gas-liquid flow in a channel was studied by Funada and Joseph using the approach of viscous potential flow [135]. This viscous theory works well for gas-liquid flows at low Reynolds numbers, especially when the liquid layer is thin [85]. We have incorporated this viscous K-H instability analysis

[135] in our problem of the plasma-melt motion and splashing. We used linearized continuity and momentum Navier-Stock equations with the assumption that the velocity can be expressed through a potential that leads to the Poisson equation. Due to this assumption, the Navier-Stock equations are completely satisfied since the viscous terms vanish, but the viscous stresses are not zero. Boundary conditions at the interface include the kinematic and dynamic conditions as well as conditions on the walls. The normal viscous stress enters into the dynamic boundary condition [135]. By applying the harmonic normal modes to the linearized Navier-Stock equations, the expressions for the relative velocity ΔV and growth rate σ_R of viscous instability are derived

$$\Delta V = |V_p - V_m| > \sqrt{\frac{(\mu'_m + \mu'_p)^2}{\rho'_m \mu'^2_p + \rho'_p \mu'^2_m}\left(\frac{g(\rho_m - \rho_p)}{k} + \gamma k\right)}, \tag{V.1}$$

$$\sigma_R = \pm\sqrt{\frac{k^2(\rho'_m \mu'^2_p + \rho'_p \mu'^2_m)}{(\mu'_m + \mu'_p)^2(\rho'_m + \rho'_p)}\Delta V^2 - \left(kg\frac{\rho_m - \rho_p}{\rho'_m + \rho'_p} + \frac{k^3\gamma}{\rho'_m + \rho'_p}\right)}, \tag{V.2}$$

where V_p, V_m, ρ_p, ρ_m denote the velocity and mass density of plasma and melt, $\rho'_p = \rho_p \coth(kh_p)$, $\rho'_m = \rho_m \coth(kh_m)$, $\mu'_p = \mu_p \coth(kh_p)$, $\mu'_m = \mu_m \coth(kh_m)$, μ_p, μ_m, h_p, h_m are the viscosity and thickness of plasma and melt, $k = 2\pi/\lambda$ is the wave number associated with small disturbances $\sim \exp(i(kx + \omega t))$, λ is the wavelength, ω is the frequency, g is the gravity constant, and γ is the interfacial surface tension. The viscous plasma has significant influence on the melt stability [41]. The expressions for critical velocity (1) and growth rate (2) of viscous plasma can be reduced to those of inviscid plasma by replacing μ_p / μ_m by ρ_p / ρ_m [135]. Analyzing Eqs (1) and (2), it can be shown that the critical velocity ΔV for viscous plasma-melt flows is always smaller than that for their inviscid counterparts [121]. It reaches a maximum when $\mu_p / \mu_m = \rho_p / \rho_m$ (an inviscid case). Therefore, the instability of melt layer can be induced by the flow of viscous plasma with significantly lower velocity.

VoF-MHD computational model The mathematical model is developed to treat the flow of liquid metal with free surface as well as the coupled flow of two fluids (plasma and liquid metal) under the influence of an external magnetic field. The model is based on a volume of fluid (VoF) approach [125, 126] implemented within the OpenFOAM (Open Field Operation and Manipulation) toolbox [124], a free open source CFD software package. OpenFOAM combines C++ libraries for different mathematical, numerical, and physical models. Various solvers and utilities can be created by combining these standard numerical tools with the physics models available in OpenFOAM. Moreover, custom solvers and new physics models can be developed and implemented for solving specific problems. Therefore, the OpenFOAM framework opens possibilities to develop new physics and computational models. As a starting point, we have utilized the VoF solver named interFoam [136]. The performance of this two-fluid solver was recently evaluated for a variety of validation test cases [137]. We have implemented the effects of thermal conduction and magnetic field in the algorithm of interFoam. The VoF-MHD model was benchmarked against the Shercliff and Hunts problems of liquid metal flow in a rectangular duct under the influence of an externally applied magnetic field [138, 139]. It is observed that with the increasing magnetic field, the velocity of liquid metal decreases and its velocity profile becomes flat in the duct core with thin Hartmann boundary layers at the duct walls. The numerical velocity profiles are found in a very good agreement with analytical solutions. The evolution of a single bubble rising in a liquid and undergoing shape deformations is also investigated. The results are found in a reasonable agreement with those reported in Ref. [140]. Modeling of a single bubble rising in liquid metal under imposed vertical magnetic field are also performed. In agreement with previous simulation results [141],

the bubble elongation in the direction of a magnetic field and the reduction of terminal bubble velocity are found for large Hartmann numbers.

The governing equations for unsteady, incompressible, immiscible two-fluid flow with heat transfer include the continuity, momentum, energy and volume fraction equations. They can be written as

$$\nabla \cdot \vec{u} = 0 \tag{V.3}$$

$$\frac{\partial \rho \vec{u}}{\partial t} + \nabla \cdot (\rho \vec{u}\vec{u}) = -\nabla p + 2\nabla \cdot (\mu \hat{\tau}) + \gamma \kappa \nabla \alpha_m + \rho \vec{g} + \vec{J} \times \vec{B} \tag{V.4}$$

$$\frac{\partial \rho c_p T}{\partial t} + \nabla \cdot (\rho c_p \vec{u} T) = \nabla \cdot (k \nabla T) + q \tag{V.5}$$

$$\frac{\partial \alpha_m}{\partial t} + \nabla \cdot (\alpha_m \vec{u}) + \nabla \cdot (\alpha_m (1 - \alpha_m) \vec{u}_c) = 0 \tag{V.6}$$

where $\vec{u}$ is the velocity field. In Eq. (4), $\rho = \alpha_m \rho_m + \alpha_p \rho_p$ is the density field with values of ρ_m and ρ_p for melt and plasma fluids, α_m is the volume fraction of melt, $\alpha_p = 1 - \alpha_m$ is the volume fraction of plasma, p is the pressure field, $\mu = \alpha_m \mu_m + \alpha_p \mu_p$ is the viscosity with components of μ_m and μ_p for melt and plasma fluids, $\hat{\tau} = (\nabla \vec{u} + (\nabla \vec{u})^T)/2$ is the viscous stress tensor, γ is the surface tension of melt, $\kappa = -\nabla \cdot (\nabla \alpha_m / |\nabla \alpha_m|)$ is the curvature of the interface, $\vec{g}$ is the acceleration due to gravity, $\vec{B}$ is the magnetic field, and $\vec{J}$ represents the current density. In Eq. (5), T is the temperature field, $c_p = \alpha_m c_{pm} + \alpha_p c_{pp}$ and $k = \alpha_m k_m + \alpha_p k_p$ are respectively the specific heat capacity at constant pressure and the thermal conductivity assuming the values c_{pm}, k_m and c_{pp}, k_p for melt and plasma fluids, $q = \vec{J} \cdot \vec{J} / \sigma$ is the Joule heating due to the electric current, $\sigma = \alpha_m \sigma_m + \alpha_p \sigma_p$ is the electric conductivity with values of σ_m and σ_p for melt and plasma fluids. In Eq. (6), $\vec{u}_c$ is the compression velocity, which is included for artificial interface compression [126, 142]. This extra compression contributes only in the interfacial region providing sharp interface and ensuring that α_m is limited between 0 and 1. Single velocity, pressure, temperature and magnetic fields are defined for plasma and melt fluids. Densities, volume fractions, viscosities, specific heat capacities, thermal and electrical conductivities are defined separately for each of fluids. The plasma-melt interface is tracked using volume fractions.

We have implemented the heat conduction Eq. (5) into the basic VoF model (Eqs (3), (4) and (6)) available in interFoam. Eq. (5) couples the velocity-temperature field. It also includes an additional source term q due the Joule heating. In the momentum Eq. (4) we have included the vector product [127]

$$\vec{J} \times \vec{B} = -\nabla \frac{B^2}{2\mu} + \frac{\vec{B} \nabla \vec{B}}{\mu} \tag{V.7}$$

that describes the Lorentz force acting on the flow of electrically conducting fluids. In Eq. (7), μ is the magnetic permeability. The first term on the right hand side of Eq. (7) describes the gradient of magnetic pressure. It can be combined with the gradient of hydrodynamic pressure in the momentum Eq. (4). The second term in Eq. (7) is the magnetic tension that acts to straighten the bent magnetic field lines. The magnetic induction equation describing the evolution of $\vec{B}$ can be written as [127]

$$\frac{\partial \vec{B}}{\partial t} + \nabla \cdot (\vec{u}\vec{B} - \vec{B}\vec{u}) - \nabla \cdot \frac{\nabla \vec{B}}{\sigma \mu} = 0. \quad \text{(V.8)}$$

Using the magnetic field $\vec{B}$ calculated from Eq. (8), the current density is then expressed as $\vec{J} = \left(\nabla \times \vec{B}\right)/\mu$. The electric field $\vec{E}$ can be determined from Ohm's law $\vec{J} = \sigma\left(\vec{E} + \vec{u} \times \vec{B}\right)$. The calculated $\vec{B}$ and $\vec{J}$ are used in Eqs (4) and (5) to compute the Lorentz force and Joule heating. It should be noted that in the present model, the Lorentz force is caused by the induced current $\vec{J}$ that is generated due to the melt motion and flow velocity variations. The induced electric field $\vec{E}$ is produced by this induced current and an electromotive field $\vec{E}_{em} = -\vec{u} \times \vec{B}$. The external currents such as the thermoelectric current due to thermal electron emission are not currently implemented in the VoF-MHD model. This implementation requiring a modification of boundary conditions will be performed in future developments of this model.

The momentum Eq. (4) and magnetic induction Eq. (8) are written in the form that can be solved within the OpenFOAM framework. Therefore, the VoF-MHD solver for the modeling of liquid metal motion and splashing without/with the impact of plasma was developed and implemented using the OpenFoam library. The magnetic pressure and tension terms (Eq. (7)) actually describing the Lorentz force are introduced in the PISO loop [136, 143] for the pressure-velocity coupling in the Navier-Stocks Eqs (3) and (4). The induction Eq. (8) is solved separately as an additional transport equation using the B-PISO loop that is similar to the PISO loop for the pressure-velocity coupling. A fictitious magnetic flux is introduced into the induction Eq. (8) in order to facilitate the divergence-free constraint on the magnetic field, $\nabla \cdot \vec{B} = 0$. This flux has no physical meaning, and at reaching the convergence it represents a small discretization error. The multidimensional universal limiter with explicit solution (MULES) [136] is used to solve the volume fraction transport Eq. (6).

Results on critical velocity and growth rate of surface waves: We first report the theoretical results from the viscous stability analysis on the onset conditions for development and growth of surface waves at the interface between plasma and W-melt. The onset of viscous instability is analytically studied using Eqs (1) and (2). In this analysis, it is assumed that the W-melt moves with velocity of ~2 m/s. The density of W-melt is $\rho_m = 16400\, kg/m^3$. W-melt thickness is $\sim 200\, \mu m$. The dynamic viscosity is $\mu_m \sim 7 \cdot 10^{-3}\ kg/(m \cdot s)$. The surface tension of W-melt is $\gamma = 2.48\, N/m$. The gravity constant is 9.81 m/s^2. The velocity of hydrogen plasma flowing over the W-melt surface was ranged from $0\, m/s$ to $5000\, m/s$. The number density of plasma is $\sim 10^{20}\ m^{-3}$ ($\rho_p \sim 1.67 \cdot 10^{-7}\ kg/m^3$) that is relevant to ITER conditions. The dynamic viscosity of plasma is $10^{-5}\ kg/(m \cdot s)$. The relative velocity ΔV and growth rate σ_R as a function of wavelength λ are shown in Fig. V.1.

The growth rates are illustrated for plasma velocities of 1000 m/s and 5000 m/s. The arrows in Fig. V.1 indicate the axis to which curve belongs to. The unstable region is located above the ΔV curve. The growing waves with critical wavelengths of ~3-8 mm can be generated by a plasma streaming with velocity higher than ~600 m/s. However, the wavelength of these waves are more than an order of magnitude larger compared to the thickness of melt layer, ~0.2 mm. The growth of these large waves on a thin melt layer may not occur. For a plasma flowing with ~1000 m/s, the fastest growing wavelength is ~600 μm (Fig. V.1). This is still about three times larger than the melt thickness of ~200 μm. The characteristic time ~$1/\sigma_R$ estimated from the growth rate is about ~0.2 ms (curve with square symbols). The flow of plasma with velocity of ~5000 m/s generates the surface waves with the fastest growing "dangerous" wavelength on the order of ~30 μm (curve with circles). The wavelength of these short waves is smaller than the thickness of W-melt, and the ejection of droplets is then expected from the W-

melt surface. The characteristic timescale of droplet development estimated from the growth rate curve is on the order of ~1 μs.

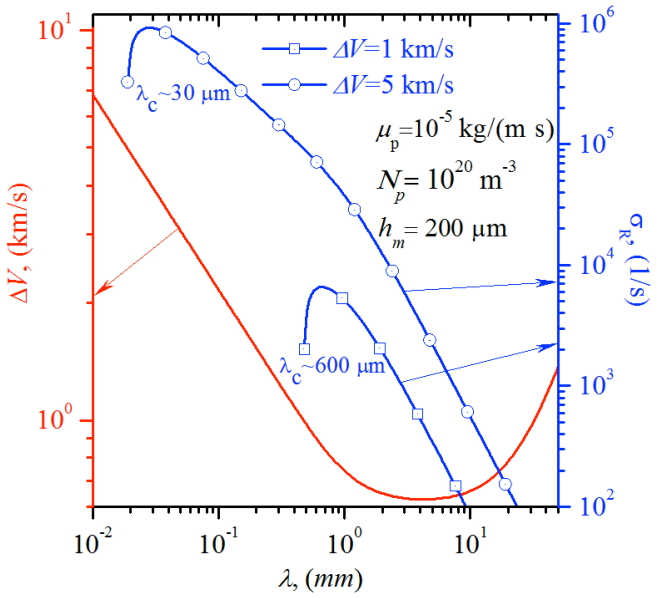

Figure V.1. Relative velocity (solid curve) and growth rates (solid curves with symbols) of waves on W-melt surface as a function of wavelength

Results on melt motion and splashing on a flat substrate. We describe here the numerical set-up of the problem, 2D computational domain, W-melt-plasma physical properties and parameters, and results on the motion of W-melt on a solid flat substrate without/with the impact of plasma. The modeling of plasma-melt flow is performed in 2D geometry, since the full 3D simulations require enormous computational resources.

Computational domain and numerical set-up The 2D computational domain is sketched in Fig. V.2. The size of computational domain is set to 5 mm in length and 1 mm in height. The interface between W-melt (in red) and plasma (in blue) is located at Y = 200 μm (Fig. V.2). The inlet and outlet of the computational domain are on the left and right sides, respectively.

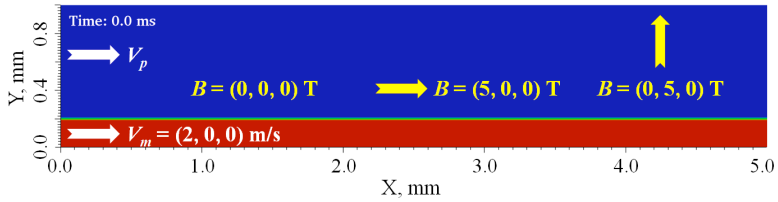

Figure V.2. Sketch of the 2D computational domain used in simulations of melt motion on flat substrate

The velocity of W-melt and plasma is prescribed at the inlet, and the boundary condition on the pressure is zero gradient. The fixed value is used for the pressure at the outlet, with zero gradient for velocity. The solid wall is located on the bottom. The non-slip boundary condition is used for velocity, with zero gradient for pressure. The top is a free boundary permitting both outflow and inflow of plasma. The parameters and physical properties of W-melt and plasma are as follows [121]. W-melt thickness is $\sim 200\ \mu m$. The molten W is kept at temperature $T_m = 3695\ K$. W-melt density is $\rho_m = 16400\ kg/m^3$. The surface tension of W-melt is $\gamma = 2.48\ N/m$. The dynamic viscosity is $\mu_m \sim 7 \cdot 10^{-3}\ kg/(m \cdot s)$. The specific heat capacity is $c_{pm} \sim 280\ J/(kg \cdot K)$. The heat conduction coefficient is $k_m \sim 80\ W/(m \cdot K)$. The

electric conductivity is $\sigma_m \sim 6.9 \cdot 10^5\ \Omega^{-1} m^{-1}$. The above parameters are defined at the melting temperature of W-melt. The velocity of W-melt is set to ~2 m/s. The velocity of hydrogen plasma streaming over the W-melt surface was in the range from $0\,m/s$ to $5000\,m/s$. The number density of plasma is $\sim 10^{20}\ m^{-3}$ ($\rho_p \sim 1.67 \cdot 10^{-7}\ kg/m^3$) that is relevant for ITER conditions. The plasma is held at the temperature of W-melt, $T_p = 3695\,K$. The dynamic viscosity is $10^{-5}\ kg/(m \cdot s)$. The specific heat capacity was estimated using the ideal gas law as $c_{pp} = \chi R_p/(\chi - 1) \sim 2 \cdot 10^4\ J/(kg \cdot K)$, where $\chi = 5/3$ is the adiabatic constant of monatomic hydrogen plasma. The thermal conductivity due to electrons is estimated as $k_p \sim 4.4 \cdot 10^{-11} (T_p[K])^{5/2}\ (\ln\Lambda/10)^{-1} \sim 3.65 \cdot 10^{-2}\ W/(m \cdot K)$, where $\ln\Lambda \sim 10$ is the Coulomb logarithm. The electrical conductivity is calculated using $\sigma_p \sim 1.5 \cdot 10^{-3} (T_p[K])^{3/2}\ (\ln\Lambda/10)^{-1} \sim 3.37 \cdot 10^2\ \Omega^{-1} \cdot m^{-1}$. The background pressure for the whole system is set to $p = 10^5\ Pa$. The applied magnetic field is $B = 5\,T$. The simulations are performed for three cases: 1) no magnetic field; 2) the direction of magnetic field is aligned with the flow direction; and 3) the direction of magnetic field is normal to the flow direction (Fig. V.2). For the specified geometry and physical properties, the Lorentz force dominates over the viscous and inertial forces for both plasma and W-melt, since the Hartmann and Stuart numbers are large ($Ha_m \sim 248$, $Ha_p \sim 102$, $N_m \sim 2.6$, $N_p \sim 10^4 - 10^6$). For W-melt, the hydrodynamic Reynolds number is large ($Re_m \sim 10^4$) meaning that the inertial forces dominate over the viscous forces. However, the viscous forces are prevailing over the inertial forces for plasma flow, since the hydrodynamic Reynolds number is small ($Re_p \sim 0.004 - 0.4$). The magnetic Reynolds number is small for both W-melt and plasma ($Rem_m \sim 0.08$, $Rem_p \sim 0.0002 - 0.02$) indicating that the induced magnetic field is negligible compared to the imposed magnetic field.

Motion of W-melt on a substrate in the absence of plasma effects First, we study a case when the plasma located above the W-melt layer is considered as motionless (velocity components are (0, 0, 0) m/s). The motion of W-melt is investigated on a substrate without the influence of magnetic field ($\vec{B}$ = (0, 0, 0) T) and when a magnetic field is parallel ($\vec{B}$ = (5, 0, 0) T) and perpendicular ($\vec{B}$ = (0, 5, 0) T) to the W-melt surface (Fig. V.3).

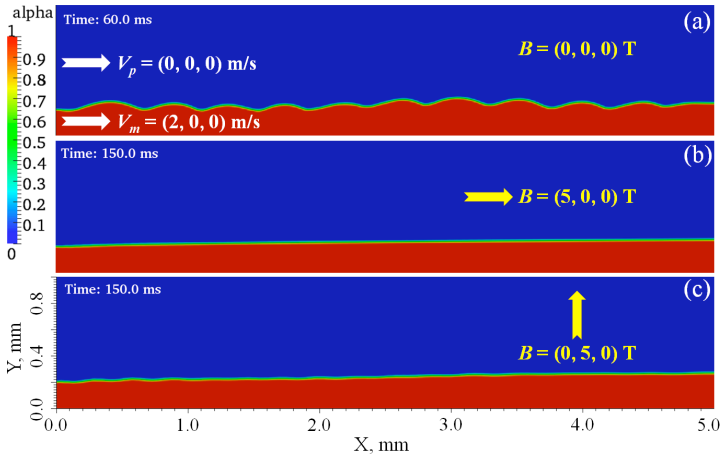

Figure V.3. Volume fraction (alpha) of W-melt in the absence of plasma stream (a) without magnetic field, (b) with an externally applied magnetic field parallel to the flow direction of W-melt, and (c) a magnetic field normal to the direction of W-melt flow. The velocity of W-melt is 2 m/s.

At $t = 0$, the velocity of W-melt has components (2, 0, 0) m/s. The interface between W-melt and plasma is flat. The volume fraction (alpha) of W-melt is shown in Fig. V.3 for different times. It is observed that in the absence of magnetic field, the running waves with wavelengths $\lambda \sim 400 - 500$ μm are developed on the melt surface after $t \sim 40$ ms. The steady-state motion of W-melt with wavy surface is shown in Fig. V.3(a) for $t \sim 60$ ms. When the externally applied magnetic field of 5 T and W-melt flow are in the same direction, the interface remains flat (Fig. V.3(b)). The development of surface waves is suppressed and they are not observed at long times ($t \sim 150$ ms). This is because the flow structures like vortices are affected by the Lorentz force (Fig. V.4). The Lorentz force acts normally on the wave crests smoothing out velocity variations in vortices and suppressing the development of surface waves. Our finding is in excellent agreement with previous theoretical and experimental results on the propagation of surface waves on liquid gallium [144]. It was observed in those studies that surface waves are completely damped when a magnetic field is imposed parallel to the propagation direction of liquid metal [144]. When the magnetic field of 5 T is imposed perpendicularly to the direction of W-melt flow, small-amplitude standing waves are generated after $t \sim 8$ ms. These small-amplitude waves on the W-melt surface are illustrated in Fig. V.3(c) at $t \sim 150$ ms. In this case the vortex evolution is damped by the Lorentz forces acting against the flow direction. The waves appear suddenly over the entire surface after ~8 ms and keep oscillating up and down. The timescale of wave development is about 5 times faster compared to that in the absence of magnetic field. In measurements [144], no damping of surface waves was found with a perpendicular magnetic field in the deep liquid metal. However, in our modeling the depth of W-melt is only $\sim 200\ \mu m$, and therefore waves are considerably damped. The pressure and velocity fields of W-melt flow are shown in Fig. V.4 at $t \sim 60$ ms. These correspond to the case shown in Fig. V.3(a).

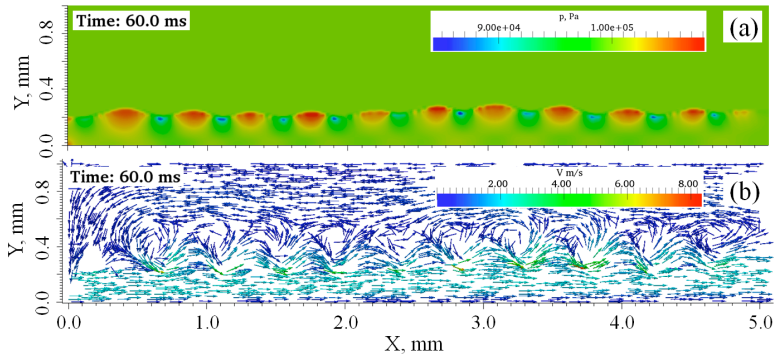

Figure V.4. Fields of (a) pressure and (b) velocity of W-melt flow for the case of zero plasma speed and in the absence of magnetic field (Fig. V.3(a))

It can be seen that the pressure deviates from background value (~10^5 Pa) at the W-melt surface (Fig. V.4(a)). The pressure is higher at wave crests and lower at melt troughs. The temperature field behaves similarly, since the temperature of melt and plasma is kept the same. Therefore, temperature fields are not reported. The vector field of velocity demonstrates vortices at the interface (Fig. V.4(b)). For clarity, the velocity vectors are shown using randomly spaced arrows. The W-melt moves downstream with velocity ~2 m/s. The velocity is close to zero on the bottom due to the non-slip boundary condition. Due to vortex development, the plasma is entrained into the motion in the opposite direction. At troughs, the velocity may reach locally up to ~8 m/s. The vortex structures are not observed at the interface in the presence of a parallel or perpendicular magnetic field (results are not shown).

Effect of plasma stream on W-melt surface To study the effect of plasma on the W-melt surface, we performed calculations considering the plasma flowing with velocities of 100, 1000, and 5000 m/s. The volume fraction of W-melt at 4 ms is shown in Fig. V.5 in the absence and presence of magnetic field. The calculation conditions are the same as those of Fig. V.3, but the plasma flows with speed of 100 m/s.

It can be seen that the stream of plasma with velocity of 100 m/s flowing over an W-melt layer that is moving with speed of 2 m/s generates the surface waves with wavelength of ~100 μm (Fig. V.5(a)). The waves are developed after ~1 ms on the entire interface. The magnetic field of 5 T that is either parallel or perpendicular to the direction of W-melt motion has insignificant effects on the development and propagation of waves (Fig. V.5(b) and (c)). The flatten portions of the interface are observed for the case of magnetic field of 5 T aligned with the direction of W-melt motion (Fig. V.5(b)). The small-amplitude waves are oscillating and their development is slightly delayed (developed after ~1.4 ms) when the magnetic field of 5 T is perpendicular to the direction of W-melt motion (Fig. V.5(c)). The map of pressure and vector fields of velocity and magnetic field are shown in Fig. V.6 for $t \sim 5$ ms. They correspond to the case shown in Fig. V.5(c). These fields of pressure and velocity are similar for other cases shown in Fig. V.5(a) and (b). We can see that the pressure is again uniform (~10^5 Pa) in the computational domain except the interface where pressure fluctuations are observed (Fig. V.6(a)).

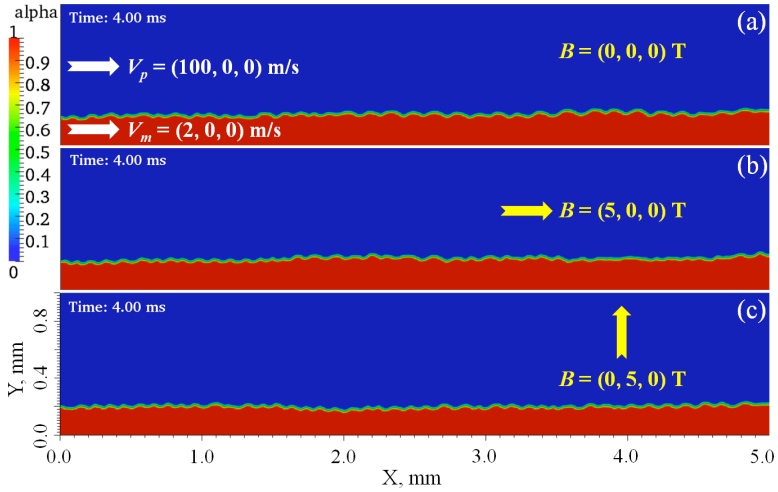

Figure V.5. Volume fraction (alpha) of W-melt (a) without magnetic field, (b) with an externally applied magnetic field parallel to the direction of W-melt flow, and (c) a magnetic field normal to the direction of W-melt flow. The velocity of W-melt is 2 m/s. The plasma flows with velocity of 100 m/s.

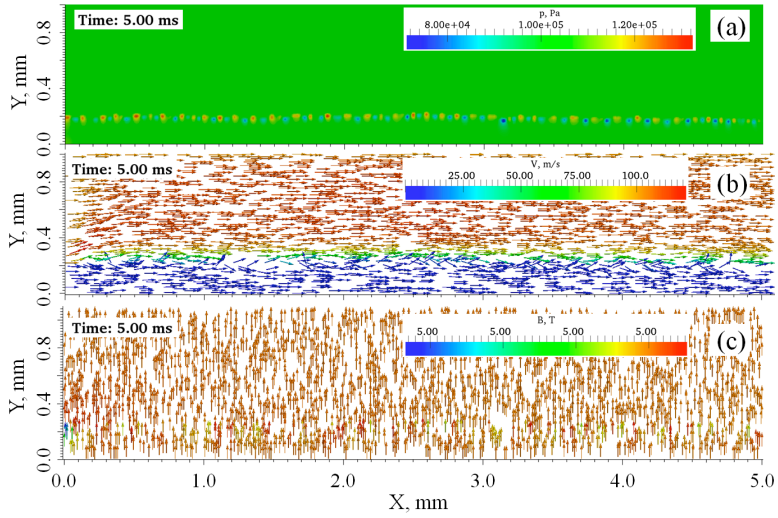

Figure V.6. Map of pressure (a) and vector fields of velocity (b) and magnetic field (c) for plasma flowing with velocity of 100 m/s in the presence of magnetic field that is perpendicular to W-melt layer (Fig. V.5(c))

However, the distribution of alternating high and low pressure vortices at wave crests and troughs is more compact compared to that of Fig. V.4(a). This is because the wavelength of surface waves is much shorter. The plasma flows with velocity ~100 m/s (Fig. V.6(b)). The speed of plasma is varied reaching ~120 m/s locally at some places. The thin shear layer is clearly seen at the interface between the plasma and W-melt where the velocity drops from ~100 m/s to ~2 m/s. The flow in the shear layer involves complex vortical structures. The vertical magnetic field of 5 T remains nearly intact (Fig. V.6(c)). The parallel magnetic field corresponding to the case shown in Fig. V.5(b) behaves similarly. There are very small fluctuations of magnetic field at the interface that are negligible (fourth-fifth digit after comma). The reason is that the magnetic Reynolds number is small, and thus the wave-induced magnetic field can be ignored.

The maps of volume fraction of W-melt impacted by a plasma with speed of 1000 m/s are shown in Fig. V.7 in the absence of an external magnetic field (Fig. V.7(a)) and in the presence of a horizontal (Fig. V.7(b)) and vertical (Fig. V.7(c)) magnetic field. It is observed that the plasma with velocity of 1000 m/s streaming over an W-melt layer moving with speed of 2 m/s initially induces a large single wave near the inlet. This large wave with a series of small waves behind it moves forward on the melt interface. It reaches the outlet at time less than ~1 ms. Thus, the surface waves develop much faster at higher plasma speeds (compare Figs V.5 and V.7). The magnetic field of 5 T that is parallel or perpendicular to W-melt doesn't prevent the development and propagation of surface waves. It is observed that a high-speed flow of plasma significantly thinners large portions of melt layer, especially when the magnetic field is perpendicular to the direction of W-melt motion (Fig. V.7(c)). In other regions, the melt thickness is increased. The short waves with a wavelength on the order of 20-40 μm are formed on the surface of W-melt. Thus, the wavelength of surface waves decreases with increasing velocity of plasma stream (compare Figs V.5 and V.7). The fields of pressure, velocity, and magnetic field (not shown) behave similarly to those of the plasma flow with velocity of 100 m/s (Fig. V.6).

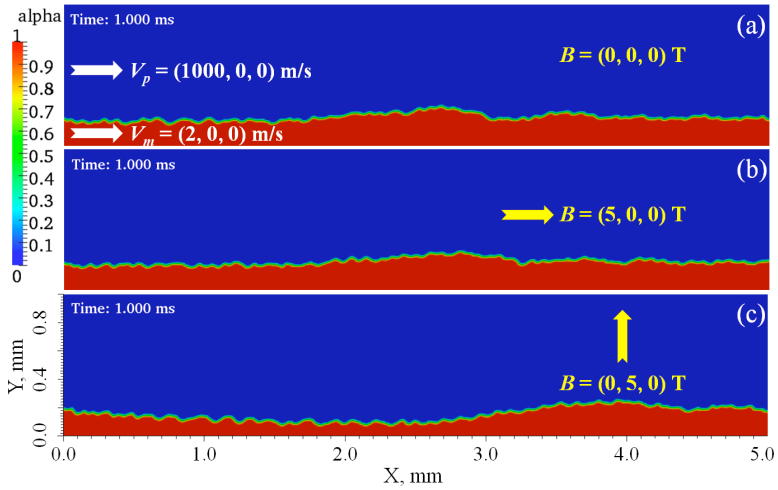

Figure V.7. Volume fraction (alpha) of W-melt (a) without magnetic field, (b) with an externally applied magnetic field parallel to the direction of W-melt flow, and (c) a magnetic field perpendicular to the direction of W-melt flow. The velocity of W-melt is 2 m/s. The plasma flows with velocity of 1000 m/s.

The entrainment of W-melt into the viscous plasma flowing with speed of 5000 m/s is shown in Fig. V.8. The growth of short-length waves and formation of droplets is initially observed near the inlet when the stream of viscous plasma with velocity of 5000 m/s impacts W-melt layer moving with speed of 2 m/s. The development of small ripples and their disintegration into droplets is then occurred on the whole interface of a melt layer within tens of microseconds. Fine droplets are sprayed from the melt and dragged

away by the plasma flow. The topology of the W-melt interface becomes very complex (Fig. V.8). The timescales of melt layer motion as a whole (tens ms, Fig. V.3) and wave development with droplet ejection (tens μs, Fig. V.8) are widely separated. Also, the wavelength of surface waves produced by W-melt motion itself with velocity ~2 m/s (Fig. V.3) and those generated by high-speed plasma streaming with 0.1-5 km/s is quite different. The horizontal or vertical magnetic field doesn't suppress droplet ejection and disintegration of melt layer.

The vector fields of velocity are shown in Fig. V.9 for time $t \sim 20$ μs in the absence (Fig. V.9(a)) and presence (Fig. V.9(b) and (c)) of a magnetic field. The background velocity of plasma is 5000 m/s. Shear regions, large vortical, and swirling flow structures can be seen in Fig. V.9. At some places, the local velocity of plasma is about 2-3 times higher than the background velocity. The melt is involved into a rotating movement of plasma by virtue of the vortical motion.

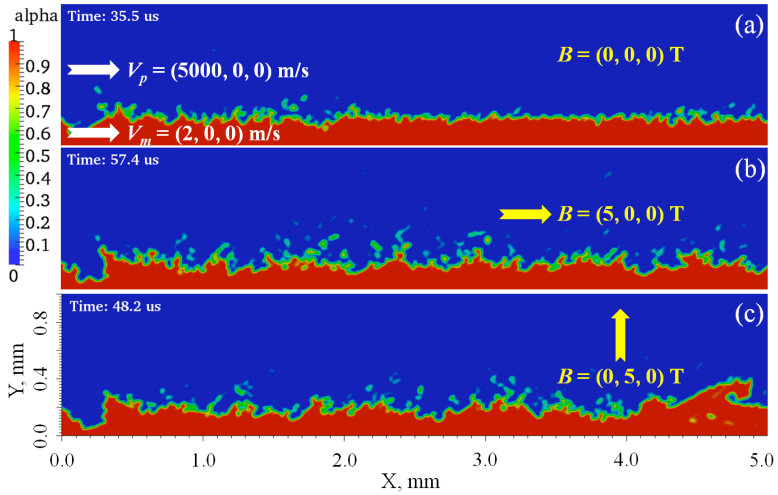

Figure V.8. Volume fraction (alpha) of W-melt (a) without magnetic field, (b) with an externally applied magnetic field parallel to the direction of W-melt flow, and (c) a magnetic field perpendicular to the direction of W-melt flow. The velocity of W-melt is 2 m/s. The plasma flows with velocity of 5000 m/s.

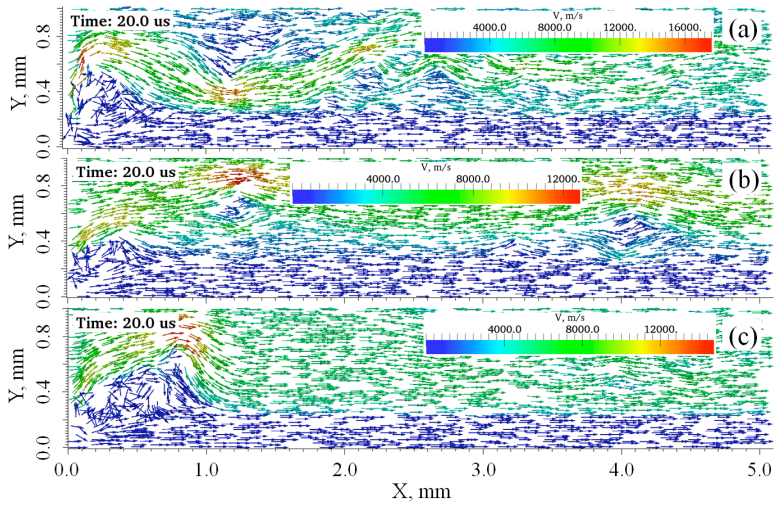

Figure V.9. The vector fields of velocity for plasma flowing with 5000 m/s in (a) the absence of magnetic field, (b) in the presence of parallel magnetic field, and (c) in the presence of magnetic field perpendicular to W-melt layer.

At the plasma-melt interface the boundary layer is developed which is highly irregular due to vortical structures. Within this boundary layer, the plasma velocity sharply drops from ~5000 m/s to ~2 m/s. Since the Reynolds number of plasma is small, the viscous plasma forces are very important in the boundary layer. Due to high velocity gradients, the destabilizing viscous stresses can overcome the stabilizing effect of surface tension. Small disturbances on the W-melt surface can grow and develop into fine droplets. These droplets are then entrained and carried away by the plasma flow (Fig. V.8).

Results on melt motion and splashing from a pool. The results of computational modeling on the melt motion and splashing from a pool, the impact of plasma stream with different velocity on the W-melt surface, and the effects of a magnetic field on W-melt motion are reported [129]. For moderate plasma velocities ($\leq$1000 m/s), the computational results are shown for a time period ~1 ms that is an overlap between the duration of ELMs (~0.1-1.0 ms) and plasma disruptions (~1-10 ms) [81].

Computational domain and numerical set-up A computational domain in 2D geometry ((x, y)-plane) is illustrated in Fig. V.10. The domain's length is 5 mm and the height is 1 mm. The interface between W-melt and plasma is at y = 200 μm. The W-melt is confined in a pool with the length of 3 mm and the depth of 200 μm. It was noted in Ref. [119] that for the modeling of viscous flows the periodic boundary conditions are not appropriate due to viscous dissipation at the interface and on the walls. The computational domain should include the inlet and outlet for W-melt and plasma. The simulations involving the boundary conditions with inlet and outlet were recently carried out for viscous W-melt-plasma flows [121]. Therefore, the velocities of W-melt V_m and plasma V_p are set to specified values at the inlet on the left-hand side of the computational domain.

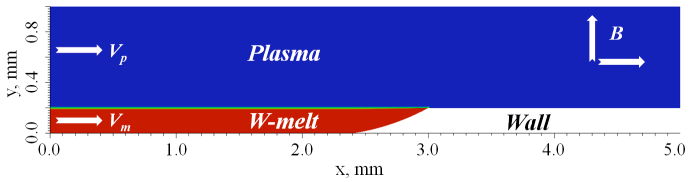

Figure V.10. Computational domain used in modelling W-melt motion and splashing from melt pool

The boundary condition for pressure at the inlet is zero gradient. At the outlet on the right-hand side of domain, the pressure is fixed to a background value. The boundary condition for velocity is zero gradient. At bottom wall, the non-slip boundary condition is used for velocity with zero gradient for pressure. The top of domain is a free boundary with both outflow and inflow of plasma. The parameters and physical properties of W-melt and plasma used in the modeling are described above for the case of a flat substrate and can be also found in Ref. [121]. The modeling is performed for three velocities of hydrogen plasma V_p ~100 m/s, ~1000 m/s and ~5000 m/s, respectively. It was found in the recent computational study that there is a strong influence of plasma speed on the stability of W-melt layer [48]. At ~5000 m/s and higher velocities, the instability of W-melt and droplet ejection is predicted from the viscous stability analysis. The externally imposed magnetic field is $B = 5\,T$. The estimated magnetic Reynolds number [128] is small for both W-melt and plasma ($Rem_m \sim 0.08$, $Rem_p \sim 0.0002 - 0.02$) meaning that the induced magnetic field is negligible compared to the imposed magnetic field. Therefore, the magnetic tension term in the expression for the Lorentz force can be neglected since $\nabla\vec{B}$ is very close to zero. The main contribution to the Lorentz force comes from the magnetic pressure. The simulation is carried out for three cases: 1) no magnetic field; 2) magnetic field is parallel to the flow direction; and 3) magnetic field is perpendicular to the flow direction (Fig. V.10).

***Motion and splashing of W-melt from a melt pool in the absence of a magnetic field**:* The fields of volume fraction of W-melt and plasma are shown in Fig. V.11. For this particular case, the influence of the magnetic field on W-melt motion is not considered. The W-melt moves with speed of 2 m/s. The plasma velocity is 100 m/s (Fig. V.11(a)), 1000 m/s (Fig. V.11(b)), and 5000 m/s (Fig. V.11(c)), respectively. At t = 0, the W-melt with an unperturbed interface is initially located in the pool formed due to an ELM or a disruption (Fig. V.10). As time progresses, the coupled flow of W-melt and plasma streamlines in the x-direction. The interaction between plasma and melt results in the generation of surface waves due to the shear force exerted by the plasma [129]. The snapshots of W-melt/plasma interface are illustrated for time moments of 1 ms (Figs V.11(a) and V.11(b)) and 44.4 μs (Fig. V.11(c)). It is previously observed that depending on the speed of plasma the effect of plasma on the melt motion is quite different [128]. For plasma flowing with velocities of 100 m/s and 1000 m/s, wavy structure is generated on the melt surface. Due to the melt motion and splashing from the pool, a large blob of W-melt with a maximum height of ~400 μm develops on the pool's edge. This kind of hill structures or leading edges with heights of several mm were reported in TEXTOR experiments [98]. The front of the blob is steep enough because of the non-slip boundary condition at the bottom wall.

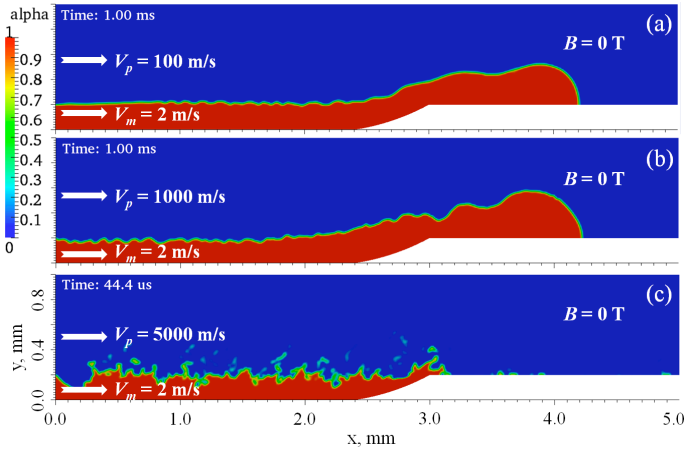

Figure V.11. Volume fraction (alpha) of W-melt for specified time moments in the absence of magnetic field effects. The velocity of plasma is (a) 100 m/s; (b) 1000 m/s; and (c) 5000 m/s. The velocity of W-melt is 2 m/s.

Further, the blob of W-melt displaces on the solid surface due to the melt inflow. It can be seen that the displaced melt moved about ~1.2 mm during ~1 ms (Figs V.11(a) and V.11(b)). A large wave develops on the blob near the pool edge. The distance of blob movement is nearly the same for plasma flow with velocity of 100 m/s and 1000 m/s. Thus, it can be concluded that the plasma stream with velocity $V_p \leq 1000$ m/s has little influence on melt motion. Surface waves with shorter wavelengths are generated on the melt surface as the speed of plasma increases. For plasma streaming with speed of 5000 m/s, the W-melt disintegrates into droplets in less than 0.1 ms (Fig. V.11(c)). The melt as a whole undergoes only insignificant movement during this short time. Thus, there is a strong impact of plasma flow on the behavior of W-melt in this case. Fine droplets are stripped and ejected from the W-melt surface and dragged away by a plasma wind. Small plasma bubbles are entrained and mixed with the melt. The topological structure of the interface is very complex. The ejected molten droplets that have fallen and redeposited on the solid surface can be seen in Fig. V.11(c).

The maps of the pressure and vector fields of velocity are shown in Fig. V.12. The pressure distribution is illustrated at time 1 ms for the case of plasma flowing with velocity of 100 m/s (Fig. V.11(a)). The background pressure is 10^5 Pa. Variations of pressure are seen at the W-melt-plasma interface as well as within a melt blob (Fig. V.12(a)). High and low pressure regions are alternately

formed at wave crests and troughs, respectively. The pressure is higher near the edge of pool (from 2 mm to 3 mm) and in some regions of melt blob. The zones of low pressure are seen within a melt blob near the solid surface (at 3.0 mm and 3.6 mm). The melt surface is generally depressed in regions of high pressure, whereas the interface is rising in areas of low pressure. These pressure fluctuations create waves with various wavelengths that propagate on the melt surface in the direction of plasma flow. Depending on the relative plasma-melt speeds and local pressure fluctuations, the generation of waves with different wavelengths occurs. Thus, the melt surface is composed of waves with various amplitudes, frequencies, and wavelengths. The interaction among these waves results in the formation of surface waves with an "average" wavelength. There is also strong coupling between the plasma flow and the motion of waves. In addition to the mentioned effect of plasma on W-melt, the disturbances in the melt surface (waveforms) induce perturbations in the plasma flow. The boundary layer is formed with vortex structures developed at the plasma-melt interface (Fig. V.12(b) and V.12(c)). The velocity decreases from the bulk plasma value (1000 m/s and 5000 m/s) to that of the melt motion (2 m/s) within this thin layer. In some regions, the local velocity of plasma stream is about 3-4 times higher compared to the background velocity. For high-speed plasma flow (Fig. V.12(c)), the complex vorticity and swirling flows in the boundary layer are responsible for the growth of short length waves, ejection of droplets, and melt disintegration.

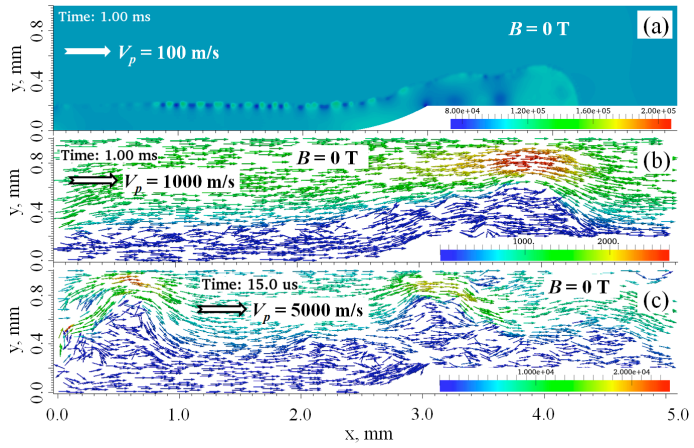

Figure V.12. Map of pressure (a) and vector fields of velocity for plasma flowing with speed of 1000 m/s (b) and 5000 m/s (c) in absence of magnetic field. In panel (a), the pressure in legend is in units of Pa. In panels (b) and (c), the units of velocity in legend are in m/s.

Motion and splashing of W-melt from a melt pool in the presence of a parallel magnetic field The influence of a parallel magnetic field of 5 T to the direction of plasma-melt flow is now taken into account. The simulation conditions are similar to those of Fig. V.11. The volume fraction of W-melt is shown in Fig. V.13. It can be seen that a magnetic field parallel to the direction of W-melt motion has little effects on development of melt blob on the edge of pool and generation of surface waves on the melt. This is because the Lorentz force doesn't affect the melt motion either in the positive or negative x-direction. It acts perpendicularly to the W-melt layer. Therefore, the effect of electromagnetic forces on the melt motion is insignificant in this case. It can also be seen in Figs V.13(a) and V.13(b) that during ~1 ms the location of melt blob is nearly the same as that found in the absence of magnetic field effects (Figs V.11(a) and V.11(b)). The height of W-melt swept away from the melt pool is ~300-400 μm. The waves on the melt surface are produced by the plasma stream. It is observed that the time-course and waveform structure of waves is the same in the absence and presence of a parallel magnetic field.

For plasma streaming with velocity of 100 m/s (Figs V.11(a) and V.13(a)), the development of surface waves begins near the edge of pool in the region from 2 mm to 2.5 mm. As W-melt splashes out of pool forming a melt blob, these waves with short wavelengths (~0.1 mm) propagate in the backward

direction toward the inlet. At time ~1 ms, portion of the melt layer (~0.8 mm) near the inlet still remains flat (Figs V.11(a) and V.13(a)). At later time ~1.4 ms, the melt surface in the pool is entirely covered by waves (results not shown). Shortly after that, the waves with longer wavelengths start to run downstream from the inlet in the forward direction. The melt blob leaves the computational domain through the outlet at time ~1.65 ms. Later after ~3 ms, the steady flow of W-melt is then established with characteristic wavelength is on the order of ~0.2 mm. For plasma flowing with velocity of 1000 m/s (Figs V.11(b) and V.13(b)), the observed dynamics of wave development is quite different from the previous case.

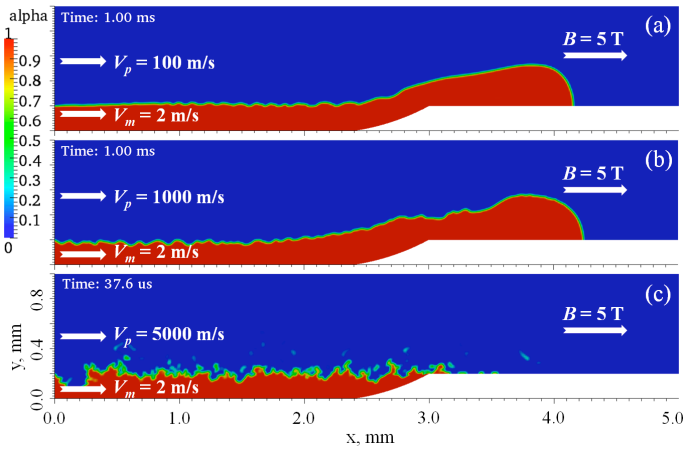

Figure V.13. Volume fraction (alpha) of W-melt for specified time moments in the presence of a magnetic field of 5 T parallel to the direction of plasma-melt flow. The velocity of plasma is (a) 100 m/s; (b) 1000 m/s; and (c) 5000 m/s. The velocity of W-melt is 2 m/s.

A single wave with growing wavelength (~0.1-0.2 mm) is shortly induced during ~0.02 ms near the inlet by the plasma flow. This wave propagates quickly on melt surface in the forward direction. A train of waves with shorter wavelengths is generated behind this single wave. At time ~0.2 ms, this structure of waves travels about ~1 mm. At this time, the melt blob is formed and the other structure of waves starts to develop near the edge of pool. These waves move in the backward direction. At ~0.4 ms, the two systems of waves collide. At later times, the waves running in the forward direction only survive. At time ~1 ms (Figs V.11(b) and V.13(b)), the wavy structure on the W-melt surface with wavelength on the order of ~0.1 mm is well developed. The melt blob is located at ~4.2 mm. For high-speed plasma streaming with velocity of 5000 m/s, a large melt disturbance develops during ~5 μs near the inlet. At ~10 μs, first molten droplets are ejected. At time ~15 μs, the small ripples with very short wavelengths start to develop and grow near the edge of pool in the region from 2.4 mm to 3 mm (Fig. V.13(c)). At ~30 μs, the surface of W-melt is completely covered by wavy ripples with ejection of droplets near the inlet and edge of pool. At later times, the droplets are ejected from the entire melt surface (Figs V.11(c) and V.13(c)) moving in the direction of plasma flow that is in agreement with observations in ASDEX Upgrade experiments [99]. During this short timescale ~40-50 μs, the W-melt layer initially located in the pool doesn't undergo significant motion or splashing at the pool's edge. Thus, we conclude that the magnetic field of 5 T that is parallel to a melt layer doesn't suppress the W-melt motion, plasma-induced development of surface waves, or the ejection of droplets.

The map of magnetic pressure is shown in Fig. V.14. For a magnetic field of 5 T, an estimate of magnetic pressure is $p_m = B^2/(2\mu) \approx 9.95 \cdot 10^6$ Pa. This is about two orders of magnitude larger than the background hydrodynamic pressure $p \approx 1.0 \cdot 10^5$ Pa. It can be seen in Fig. V.14 that the gradients of magnetic pressure are extremely small. For plasma flow with velocity of 100 m/s and 1000 m/s (Figs V.14(a) and (b)), the difference is negligible. The magnetic pressure is mainly varied at the interface between W-melt and plasma, within a melt blob, and near a solid wall at the edge of pool. The magnetic

pressure is also larger in the vicinity of the front of melt blob. For plasma streaming with speed of 5000 m/s, the disturbance of magnetic pressure is seen within a wide area (Fig. V.14(c)). However, the variation of magnetic pressure is still insignificant. These small variations mean that the pressure gradients due to a magnetic field are negligible. The reason is that the changes of a magnetic field due to the W-melt-plasma motion are very small as will be shown next later. Thus, we conclude that flow variations are mainly induced by the hydrodynamic pressure.

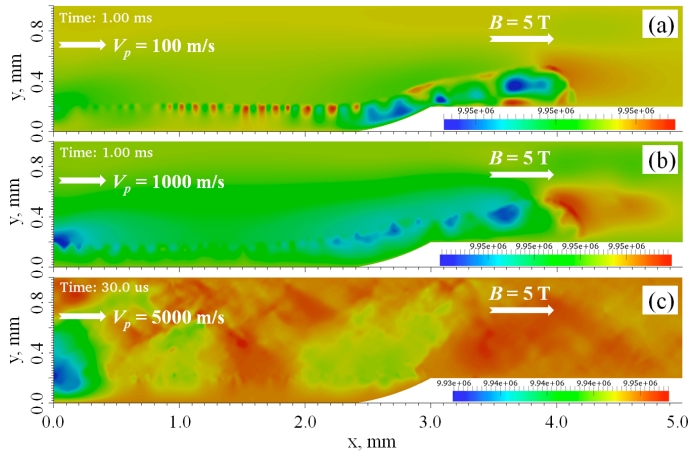

Figure V.14. Maps of magnetic pressure for plasma flowing with velocity of 100 m/s (a), 1000 m/s (b) and 5000 m/s (c). The 5 T magnetic field is parallel to the direction of W-melt-plasma flow. In legends, the pressure is expressed in units of Pa.

Motion and splashing of W-melt from a melt pool in the presence of perpendicular magnetic field The direction of the magnetic field is assumed perpendicular to the W-melt layer. In this case, the Lorentz force may act either along or against the direction of the W-melt-plasma flow, thus affecting its behavior. The results on the volume fraction of W-melt are shown in Figs V.15(a) and (b) at time ~1 ms for a plasma flowing with velocity of 100 m/s and 1000 m/s, respectively. The topological structure of the W-melt surface is illustrated in Fig. V.15(c) at time ~46.3 μs for a plasma streaming with velocity of 5000 m/s.

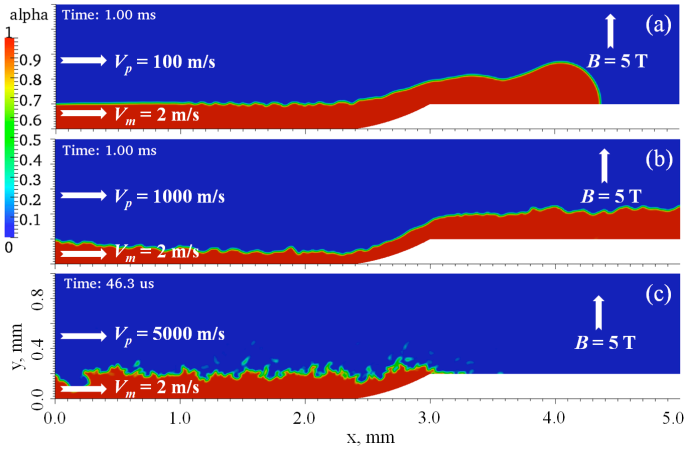

Figure V.15. Volume fraction (alpha) of W-melt for specified time moments in the presence of 5 T magnetic field perpendicular to the direction of plasma-melt flow. The velocity of plasma is (a) 100 m/s; (b) 1000 m/s; and (c) 5000 m/s. The velocity of W-melt is 2 m/s.

In the case of plasma flow with velocity of 100 m/s (Fig. V.15(a)), there is little change in the volume fraction of W-melt compared to the cases shown in Figs V.11(a) and V.13(a). The dynamics of melt motion, wave development, and formation of melt blob in a perpendicular magnetic field is similar. However, it is seen in Fig. V.15(a) that at time ~1 ms the front of melt blob is more advanced by ~0.2 mm and the length of the flat melt region near the inlet unperturbed by waves is about ~1 mm. Thus, during ~1 ms the impact of plasma with velocity of 100 m/s on W-melt is not significant. At this plasma speed, time ~1 ms is short enough for the wavy structure on the W-melt surface to become well developed. Plasma flowing with velocity of 1000 m/s over W-melt during ~1 ms generates well-developed wavy structure. Thus, during this time interval the flow of plasma is well coupled to the flow of W-melt. A perpendicular magnetic field of 5 T has a significant influence on the W-melt motion. Due to the Lorentz force affecting the coupled W-melt-plasma flow, the dynamics of W-melt (Fig. V.15(b)) is completely different compared to that shown in Figs V.11(b) and V.15(b).

As in the previous cases, a single W-melt wave is initially induced by the plasma flow near the inlet. However, it travels faster reaching ~1 mm during ~0.18 ms. At time ~0.3 ms, the waves are developed on the entire surface of W-melt. The melt blob is not formed at the edge of pool, but the W-melt layer with height ~200 μm and abrupt front moves on the solid substrate. The thickness of W-melt in the pool starts to fluctuate with a large wavelength of ~0.5-1.0 mm. The front of W-melt reaches a location of ~4.2 mm at time ~0.55 ms. This is almost two times faster compared to the cases shown in Figs V.11(b) and V.13(b). The front of melt is deformed with a spike of ~0.2 mm and height ~100 μm protruded forward on the solid substrate. At later times, the length of this melt spike increases and large wavy structures develop on the melt front. The W-melt reaches the right side of the computational domain at time ~0.8 ms. In previous cases (Figs V.11(b) and V.13(b)), this happens at time ~1.5 ms. After that, W-melt moves out through the outlet. It is seen in Fig. V.15(b) that at time ~1 ms the thickness of melt is about ~200 μm on the substrate outside the pool, but the W-melt is thinner inside the pool. We conclude that the coupled flow of W-melt and plasma is accelerated in the magnetic field perpendicular to the direction of their motion. For plasma streaming with velocity of 5000 m/s (Fig. V.15(c)), the surface of W-melt becomes disturbed during tens of microseconds due to plasma impact. As in previous cases (Figs V.11(c) and V.13(c)), the waves with very short wavelengths grow quickly on the W-melt surface breaking-up and ejecting droplets into the plasma. The melt doesn't undergo significant motion during this short time. Thus, at high plasma speeds ~5000 m/s no influence is predicted of a perpendicular magnetic field on melt layer stabilization.

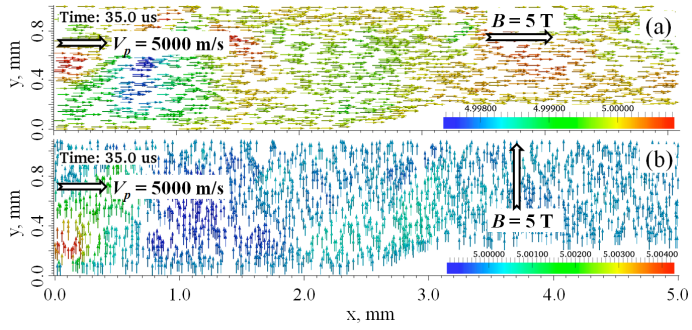

Figure V.16. Maps of magnetic field at time ~35 μs for plasma flowing with velocity of 5000 m/s in the presence of magnetic field that is (a) parallel and (b) perpendicular to W-melt layer. In legends, the magnetic field is expressed in units of T.

The fluctuations of a magnetic field that is parallel or perpendicular to the direction of coupled W-melt-plasma flow are illustrated in Fig. V.16 for time ~35 μs. It can be seen that compared to the externally imposed field of 5 T, the local disturbance of a magnetic field (induced field) due to the motion of W-melt and plasma is very small. In legends, the change is seen in a third digit after comma. The

reason is that the magnetic Reynolds number is small for both W-melt and plasma indicating the effects of magnetic advection are relatively unimportant.

Summary: Melt layer erosion and splashing of metallic plasma facing components in tokamaks during plasma instabilities is a very serious problem. The viscous stability theory is developed and applied to investigate the stability of W-melt in a melt pool under the impact of viscous plasma. The onset conditions of viscous instability, most dangerous wavelengths, and growth rates are predicted for ITER-like conditions. It is found that the viscous plasma streaming over W-melt surface with velocity of ≥ 5000 m/s can produce melt disturbances with the fastest growing wavelength on the order of ~30 μm. This wavelength is smaller than a typical thickness of melt layer ~100-200 μm. These short waves can then grow on the timescale of ~1 μs. To predict and simulate the behavior of tungsten material during plasma disruptions and giant ELMs, comprehensive and integrated VoF-MHD model is developed that combines the Navier-Stocks equations with heat conduction and magnetic induction equations. The VoF-MHD computational model is implemented in the framework of OpenFOAM package.

The modeling of coupled W-melt-plasma flow is performed on a flat substrate. The effect of plasma flow speed on the W-melt stability is investigated. In the absence of plasma stream, it is observed that surface waves are developed on flowing W-melt with wavelengths on the order of ~400-500 μm. These waves are suppressed by the magnetic field of 5 T aligned with the direction of W-melt motion. The small standing waves are observed when the magnetic field of 5 T is perpendicular to the direction of W-melt motion. In the presence of plasma stream, the magnetic field that is either parallel or perpendicular to the W-melt layer doesn't suppress the development and propagation of surface waves. At high plasma velocity of ~5 km/s, the growth of small ripples and their disintegration into droplets occurs on the whole surface of W-melt layer within tens of microseconds. It is generally observed that 1) surface waves generated due to W-melt motion itself with ~2 m/s and those produced by high-speed plasma flow with ~0.1-5 km/s have different wavelengths; 2) wavelength of surface waves decreases with increasing velocity of plasma stream; 3) surface waves develop much faster at higher plasma speeds; and 4) timescales of melt motion as a whole (tens ms) and droplet ejection (tens μs) are quite different. These effects of plasma on the W-melt motion are present on the typical timescales of ELMs (milliseconds), and therefore they are also valid under steady state operation conditions. More detail modeling and simulation coupled with well-defined relevant experiments to tokamaks conditions are critically needed to fully understand the consequences of melt layer behavior and splashing during abnormal plasma events.

The developed VoF-MHD code is also used to study the motion and splashing of W-melt from a melt pool on PFCs. In the absence of a magnetic field, it is observed that plasma streaming with velocity of ≤ 1000 m/s has little effect on melt motion and splashing from a pool. During ~1 ms, waves are generated on the W-melt surface and large blob of W-melt is formed on the pool's edge within ~1.2 mm. Plasma streaming with velocity of ~5000 m/s has strong impact on the behavior of W-melt. W-melt becomes disintegrated into droplets in less than 0.1 ms without significant movement and splashing from a pool. Droplets are stripped from W-melt and dragged away by the incident plasma wind. The presence of a magnetic field that is parallel to the direction of W-melt motion has no significant effect on generation of waves on melt surface and on formation of melt blob on pool's edge. For all three considered plasma speeds, waveforms and time-course of wave development are very similar to those in the absence of a magnetic field. However, the magnetic field perpendicular to the direction of W-melt motion produces Lorentz force that significantly affects melt splashing from pool when the flow of plasma with velocity of ~1000 m/s becomes well coupled to the flow of W-melt. For lower plasma speeds ~100 m/s, the melt acceleration is insignificant. At high plasma speeds ~5000 m/s, the W-melt disintegrates into droplets before it even moves. Therefore, we conclude that there is a certain regime when the flows of W-melt and plasma in a perpendicular magnetic field become well coupled and accelerated by the Lorentz force resulting in a large redistribution and disintegration of W-melt. This is a very serious concern for PFC lifetime as well as plasma contamination and reliable operation.

VI. Effect of Carbon Impurities on He^+ ion Irradiation induced Surface Morphology of Tungsten

Scientific background and motivation:

High melting point and relatively low sputtering yield makes tungsten (W) a potential candidate for plasma-facing components (PFCs) in the international thermonuclear experimental reactor (ITER) [145, 146]. During reactor operation, PFC materials will be exposed to high flux of energetic particles along with high heat loads[3]. These extreme conditions promote a considerable erosion of the PFC due to sputtering and thermal evaporation [145, 146]. Ultimately most of the eroded materials are expected to be deposited or implanted in the diverter materials [146-148]. W is selected for future diverter target plates and beryllium is selected for first wall components where a higher risk of contamination and plasma induced mixing are present [145, 148]. Several research groups around the world are extensively working to understand plasma induced mixing of several systems such as W-C [149, 150], W-Be, and W-Be-C [148], most of these studies were based on either simulation results or experimental procedures where conditions relevant to a magnetically confined fusion device were considered.

The sputtering yield of W bombarded by carbon ions at room temperature (RT) was dramatically decreased with carbon dose at certain angles [151]. The presence of carbon on W surface reduced the weight loss of W due to sputtering [151]. This observation motivated several other studies to work on this topic and addressed related phenomena at higher temperature [152, 153]. The enhanced diffusion of carbon at high temperature played a significant role in modifying the results primarily observed in the case of RT bombardment [153]. The temperature has a strong effect on the range distribution of carbon in W. At higher temperature, carbon atoms are expected to penetrate more in depth in the W sample as a result of the enhanced diffusion of carbon in tungsten [150, 152, 153]. Due to the decrease in carbon concentration near the W surface at higher temperature, W erosion rate (weight loss) was higher at higher temperature. Although W bombardment by carbon experiments was vital to show the impact of C-W mixing on changing the original physical properties specially sputtering yield of W surface, the experimental conditions used in such studies [151-153] were far from the conditions under which the W-diverter is operated, where simultaneous H isotopes and He are impinging with possible C contaminants that might generated from the (nearby) diverter-plasma striking plates. This later part was primarily suggested to be made of a special grade of graphite (CFC) before it was replaced by W [154]. Although currently there is no intention to use the CFC as a PFC in ITER (according to the updated ITER design) [155], still the existence of carbon contamination in any fusion device's plasma chamber is always a possible scenario.

More practical experimental setup was designed by Ueda et al. [149, 150, 156], where the tungsten sample was bombarded by hydrogen ions with a tiny percentage of carbon ions (~1%). Their results shows that, even at this small percentage of carbon contamination, the carbon concentration at the surface was dominant after a dose of about 3×10^{24} ion m^{-2} and at W surface temperature of 650^oC. They also found that a major part of the surface carbon was in a form of tungsten carbide (WC) [150]. WC is a very hard and brittle material and hence, its presence on the W surface could lead to degradation in the mechanical and thermal properties of the W. Similar carbon depth distribution was also obtained by simulation using ITMC-DYN models [157, 158]. It was found that temperature has large influence on the chemical state of carbon in W substrate. In fact, the presence of carbon in the form of WC was favorable at higher temperature (above 700K) [159], and hence, unreacted carbon was found only near the surface were the atomic concentration of carbon is higher than stoichiometric ratio of WC (1:1) [150]. Carbon is expected to be contaminant of the ITER's W diverter, and its presence on W surface is not limited to the negative impact on the mechanical and thermal properties of the W. Actually carbon is expected to play more important role in other issues such as the evolution of the W surface morphology during plasma exposure [148] and the impact of carbon on hydrogen isotopes retention of the W divertor [160, 161].

Tungsten surface morphology evolution during plasma exposure is an important factor need to be taken into account when considering safe and steady state operation of fusion devices. The formation of fine and brittle nanostructure (Fuzz) of W at the surface has been reported after the exposure to high doses of low energy He^+ ions or plasmas at elevated temperature [162-165]. The presence of such fragile

structure represents a potential serious threat for stable operation of the confined plasma. In fact, the introduction of minute percentage of a high Z material such as tungsten to the confined D-T plasma will lead to immediate plasma cooling (quenching) due to radiation energy losses. This scenario is expected if the extremely fragile tungsten fuzz structure washed out into the confined plasma during transient events such as plasma instability [147, 166]. The presence of carbon contaminants at W surface was found to reduce the ability of W surfaces to develop such structures [162].

Though extensive studies have been reported on W-C system, still the effects of PFC intermixing during plasma exposure on the original physical properties of the material are not well understood. Moreover the underlying physics of the W nanostructure (Fuzz) formation during He plasma exposure are still unclear. Further investigations have to be conducted in order to resolve these difficulties. In this investigation we are highlighting the role of a small percentage of carbon impurities (within the He ion beam) on the W surface response to a high dose of He irradiation. The response of the W surface during He^+ irradiation with various carbon at.% will be shown and discussed in detail, in following sections.

Experimental details:

The experiments have been performed in our *state-of-the-art* IMPACT (Interaction of Materials with Particles and Components Testing) laboratory at Center for Materials under extreme environments (CMUXE), Purdue University. Figure VI.1 shows the IMPACT facility. It has been designed to study *in-situ* dynamic heterogeneous surfaces at the nano-scale exposed to varied environments that modify surface and interface properties. The IMPACT system consists of 3 ultrahigh vacuum chambers (named IMPACT -1, -2, and -senior chambers) and the target of interest can be transported to each chamber for particular experiments without braking vacuum. Each chamber in the IMPACT system is designed for particular application. The philosophy behind experiments in IMPACT relies heavily on its ability to provide a wide array of characterization techniques and conditions that properly simulate complex environments. The IMPACT experiment achieves this by atomic-scale characterization of the evolution of elemental, chemical, and thermodynamic states of ultra-thin film surface and interfaces using complementary surface-sensitive characterization techniques.

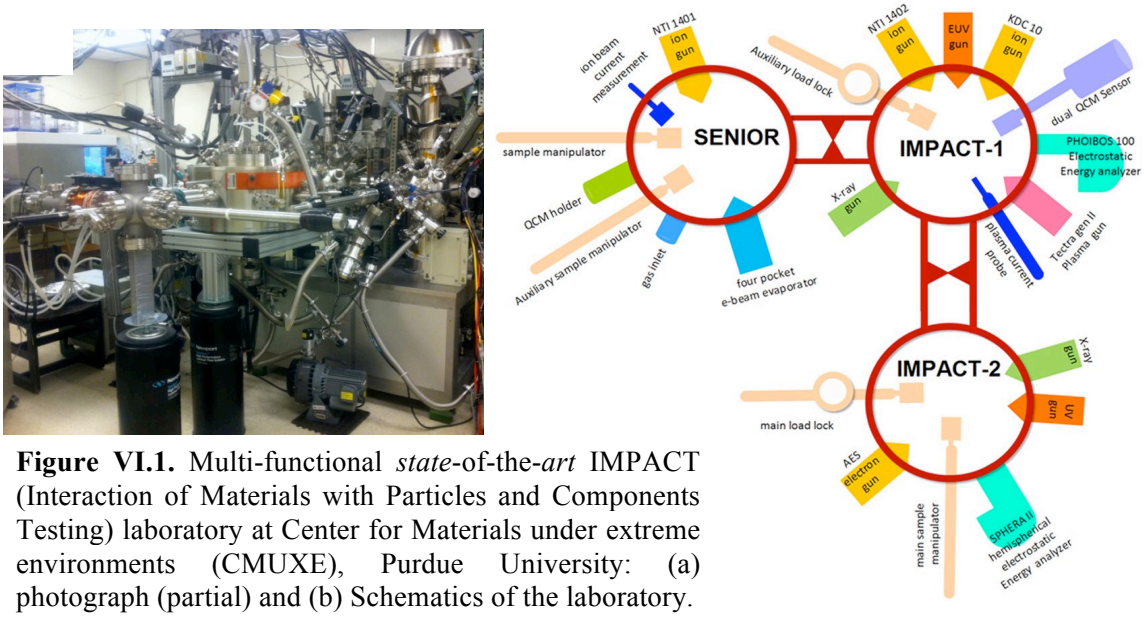

Figure VI.1. Multi-functional *state*-of-the-*art* IMPACT (Interaction of Materials with Particles and Components Testing) laboratory at Center for Materials under extreme environments (CMUXE), Purdue University: (a) photograph (partial) and (b) Schematics of the laboratory.

In-situ techniques used in the IMPACT include, but not limited to, LEISS with simultaneous forward and backward scattering modes, Direct recoil spectroscopy (to study impurity levels in the film), XPS, AES, EUVPS (13.5-nm), UPS, EUVR, and Mass spectrometry. UPS combined with EUPS and LEISS

can give chemical state and elemental information at the first 2-3 monolayers (ML), respectively. AES and XPS give similar information at probing depths from 2-3 monolayers down to about 10-15 nm into the bulk of a thin film. Both ion and electron spectroscopies are conducted using a highly sensitive hemispherical energy multi-channel analyzer. High-resolution depth profiles are obtained by using a unique low-energy ion source delivering 100 eV ions of any desired inert gas species at current densities of 2.5 $\mu A/cm^2$. Simultaneous to surface analysis of the irradiated sample, the total erosion flux is measured *in-situ* using an ultra-sensitive temperature-compensating quartz crystal nanobalance – dual crystal unit (QCN-DCU) with resolution better than 0.005 Å/sec. During ion etching the sample can be tilted at any desired angle with respect to its surface normal from 0-60 degrees with a resolution of better than 0.1 degrees. Dynamic effects induced by energetic charged particles can range from induced surface morphology evolution to physical sputtering. The IMPACT system consists of two electron analyzers. The electron analyzers are used for recording the photoelectron spectra (XPS, AES, UPS or EUPS) or scattered low energy ion spectra (LEISS).

W sheets having purity of 99.95% and thickness of 0.5 mm have been used for these experiments. All the samples were cut from the same sheet in 10mm×10mm size and after then mechanically polished to a mirror like surface. Prior to He^+ ion irradiation, every sample was sputter cleaned using 1 keV Ar^+ ions for 45 seconds at RT. For ion irradiation experiments, Kaufman & Robinson, Inc. (KRI)-KDC-10 ion-gun, which uses a direct-current (dc) discharge to generate ions has been used. The base pressure of the ultra-high vacuum (UHV) chamber was 1.0×10^{-9} torr, however the pressure during ion irradiation was 1.0×10^{-3} torr. The target (W sheet) temperature was 900^oC for all the samples. For inserting carbon contamination we used a mixture of He and CH_4 gas. The selected energy and fluence were 300eV and 1×10^{25} ions m^{-2}, respectively. He^+ ion irradiations have been done as function of C impurity. In this way five samples have been considered for the present study viz., (i) $He^+ : C^+ : H^+ :: 100 : 0: 0$, hereafter pure He^+ ion, (ii) $He^+ : C^+ : H^+ :: 97.5 : 0.5 : 2.0$, hereafter 0.5% C with He^+ ion, (iii) $He^+ : C^+ : H^+ :: 99.75 : 0.05 : 0.2$, , hereafter 0.05% C with He^+ ion (iv) $He^+ : C^+ : H^+ :: 99.95 : 0.01 :0.04$, hereafter 0.01% C with He^+ ion, (v) $He^+ : C^+ : H^+ :: 0 : 0 : 100$, hereafter pure H^+ ion. *In-situ* X-ray photoelectron spectroscopy (XPS) has been performed for pristine and all post irradiated W sample. During XPS measurements the photoelectrons were excited using x-ray source of *Mg-*K_α (energy=1253.6 eV) radiation source (SPECS XRC-1000) and the emitted photoelectrons were analyzed using omicron argus hemispherical electron analyzer using set of round aperture of 0.63 mm (for imaging-XPS) and 6.3 mm (for XPS). No samples charging were observed. After the completion of *in-situ* ion irradiation and XPS studies on the samples, they were taken out from UHV chambers for *ex-situ* Scanning electron microscopy (SEM) using JEOL and Hitachi S-4800 Field Emission SEM and cross-sectional focused ion beam (FIB) using FEI Nova 200 Nanolab Dualbeam FIB which is a combination of ultra-high resolution field emission scanning electron microscopy (SEM) and precise focused ion beam (FIB) etch and Pt deposition, studies.

Experimental Results and Discussion:

(A) Pure He^+ ion irradiation:

The first experiment was done using pure He^+ ion beam (flux=$3.0\text{x}10^{20}$ ion/m^2s) for 9 hours. Surface darkening was noticed on the sample surface after the pure He irradiation. The sample surface tends to change to dark or black color in response to the change in the surface optical properties due to the formation of very fine nanostructure (W fuzz). The surface darkening in our He irradiated sample can be observed by comparing the sample before and after He irradiation.

The surface structure of the irradiated sample was observed using SEM (Figure VI.2a). As we mentioned earlier, W fuzz was formed on the sample surface after a dose (1.0×10^{25} ion/m^2) of He irradiation. Figure VI.2a shows SEM image of the irradiated surface. The image is taken at 52° tilt to help observe the depth of the structures. Very fine nano-rods of W were formed on the surface. This surface morphology evolution due to pure He irradiation at elevated temperature was expected and is in agreement with other similar studies [163-165, 168]. The reason behind the formation of this nanostructure was justified by many different hypotheses [162-166, 169, 170]. In summary, it is believed that the formation of He

bubbles beneath the W target surface during the irradiation process plays a significant role in W fuzz formation. The growth and the coalescence of these He bubbles can significantly reshape the exposed surface and subsurface regions.

The chemical composition of the sample surface after irradiation was measured by XPS. The XPS spectrum of the irradiated surface shows a typical pure W spectrum. The wide XPS survey (shown in Figure VI.3) shows mainly W peaks in addition to a weak oxygen peak. We believe that the presence of oxygen on the sample surface is due to water adsorption that might be occurred in the vacuum chamber after the He irradiation process. This fact was confirmed by the absence of W oxide peaks in the high-resolution XPS spectrum of the W4*f* region presented in figure VI.2-f. As it can be seen clearly in this figure, only three peaks represent the pure state of W were found. The W $4f_{7/2}$ and $4f_{5/2}$ were located at 31.4 and 33.58 eV respectively. The shift between these two doublet peaks was found to be exact at 2.18 eV. This value of shift and the position of the W $4f_{7/2}$ peak were in agreement with the most accepted peaks positions in literature that represent the pure state of W [167]. The third small peak on the higher binding energy side of the W 4*f* doublet is also representing the pure state of W5*p* level.

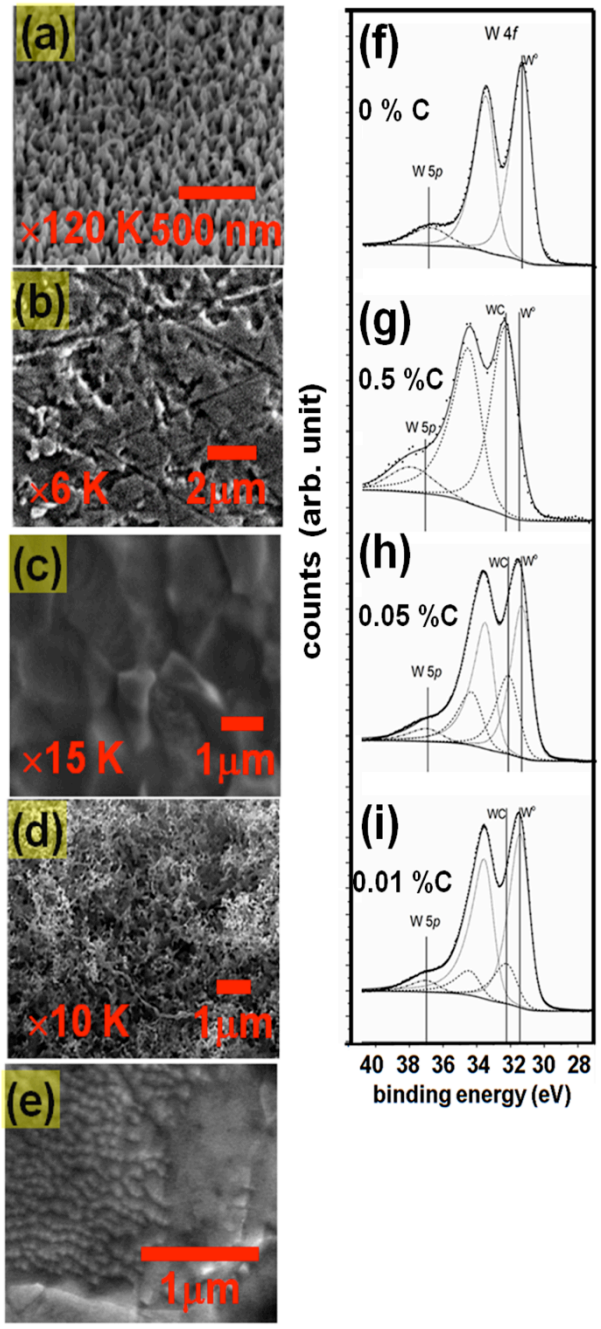

Figure VI.2: Scanning electron microscopy (SEM) (left column) and *in-situ* X-ray photoelectron microscopy (XPS) (right column) studies on helium ion induced surface morphology changes in tungsten at 900°C as a function of carbon impurity. The selected ion energy and fluence were 300eV and 1×10^{25} ions m^{-2}(with an ion-flux of 3×10^{20} ions m^{-2} s^{-1}), respectively. Five experiments have been done in various He^+ , C^+, and H^+ ions ratio (at.%) using same ion irradiation parameters: He^+ : C^+ : H^+ :: 100 : 0: 0 (a); He^+ : C^+ : H^+ :: 97.5 : 0.5 : 2.0 (b); He^+ : C^+ : H^+ :: 99.75 : 0.05 : 0.2 (c); He^+ : C^+ : H^+ :: 99.95 : 0.01 :0.04 (d); and He^+ : C^+ : H^+ :: 0 : 0 : 100 (e). note that, figure VI.1(a) was recorded at 52° tilt and rest of at 0° tilt. The corresponding high resolution *in-situ* XPS results for W4f doublets were shown in the right column (f)-(i).

Figure VI.3: *In-situ* core level survey XPS spectra of pure 300eV He^+ ion irradiated, using 1×10^{25} ions m^{-2} ion fluence (with an ion-flux of 3×10^{20} ions m^{-2} s^{-1}), tungsten surface at 900°C.

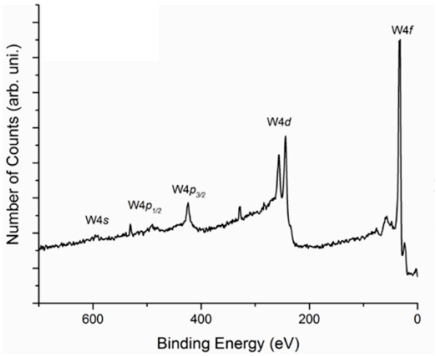

(B) He^+ ion beam irradiation with 0.5% C ions:

The next step is to introduce a small percentage of carbon ions into the He ion beam and study the W surface evolution after exposure to this mixed ion beam at 900^o of surface temperature. Primarily, we introduced about 0.5% carbon into our pure He ion beam. A new W sample was irradiated by this mixed ion beam for a total dose of $1.0x10^{25}$ ion/m^2. Shortly after the start of irradiation a visible carbon layer was developing on the sample surface. This carbon layer was increasingly darkened over the course of bombardment. After the end of the irradiation process, the sample was cooled down and the surface composition was measured by XPS. The wide XPS survey shown in shows that the sample surface was fully covered with pure carbon (figure VI.4a and b). The C1s region was scanned by high resolution XPS and shows a carbon 1s peak situated at 284.5 eV. This peak position emphasizes that the carbon layer was in a graphitic form. Upon removing the sample from the vacuum chamber, some of the carbon layer that was covering the sample surface was stripped without any physical intervention. The reason behind this unplanned and uncontrolled film removal might be due to pockets of low pressure He gas trapped beneath the carbon film. The carbon film removal occurs only in a narrow area around the sample center (ion beam center).

The partial removal of the carbon film from the sample surface facilitates the opportunity to measure the composition of the original sample surface (the original W surface) and to investigate the morphology evolution of the W surface beneath the carbon film. XPS is performed on the stripped area. Due to the fact that the stripped area is small and it represents a small fraction of the entire sample surface, a special measure has to be taken into account to precisely select this small area for the XPS data acquisition. Hence, an XPS image of the surface was taken. The XPS image allows to precisely choosing any part of the surface for further XPS spectral analysis. The XPS spectra of the stripped sample surface are shown in Figure VI.2 (g). The wide XPS survey presented in figure VI.4-c shows the coexistence of both C and W in the sample stripped area. Although the W signal is strong, the surface carbon composition still dominant with more than 90 at. % concentration compared to less than 10% of W exist on the stripped sample surface. On the other hand, the W 4f region presented in figure VI.2-g shows that the surface W was completely in the form of WC. The WC 4$f_{7/2}$ peak was found to be at 32.2 eV.

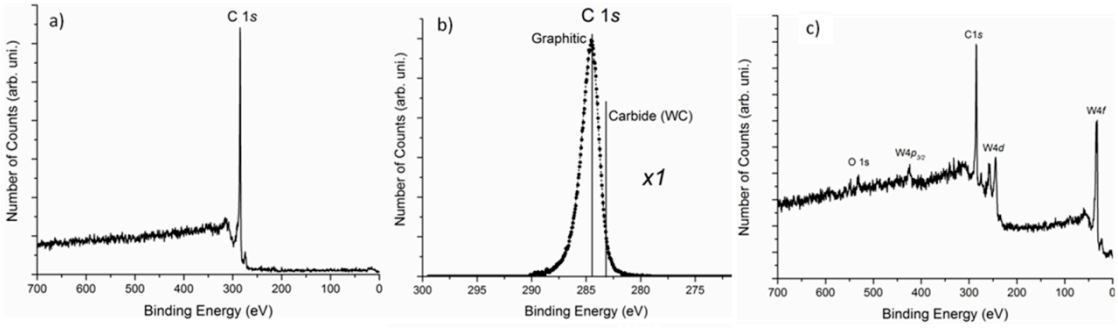

Figure VI.4: core level survey XPS spectra of 300eV He^+ ion with an impurity of 0.5% C irradiated, using 1×10^{25} ions m^{-2} ion fluence (with an ion-flux of 3×10^{20} ions m^{-2} s^{-1}), tungsten surface at 900°C. *In-situ* XPS spectra (a) and (b); *en-situ* XPS spectra (c).

The irradiated sample surface was examined by SEM as shown in Figure VI.2 (b). Figure VI.5 shows low magnification SEM image of the sample surface where part of the stripped area can be seen. The darker the area is the thicker graphite coat while the brightest one is the fully stripped area. This image

shows that the carbon film was actually a stack of multiple thin carbon films on top of each other. The brighter part of the image shows the fully stripped area where the original W surface can be seen.

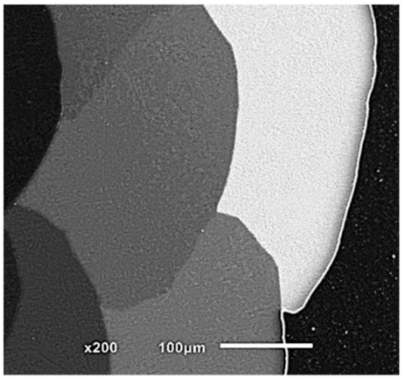

Figure VI.5: low resolution SEM image of 300eV He^+ ion with an impurity of 0.5% C irradiated, using 1×10^{25} ions m^{-2} ion fluence (with an ion-flux of 3×10^{20} ions m^{-2} s^{-1}), tungsten surface at 900°C (see text for more details).

A higher magnification images of this fully stripped area is shown in figure VI.2-b. As it can be seen in this image, the sample surface was severely modified (roughened) but the surface scratches originated during the sample surface preparing (mechanical polishing) are still noticeable. This newly developed surface roughness is most likely due to some residual pure carbon partial coverage supported by a thick layer of WC carbide formed beneath the surface. The main conclusion of this experiment is the existence of pure carbon on the sample surface that prevented the formation of W fuzz on the sample surface. Also we concluded that this percentage of carbon impurity within the He ion beam is very high. Our next step is to repeat the experiment with much lower carbon percentage.

(C) He^+ ion beam irradiation with 0.05% C ions:

A newly prepared sample was irradiated at high temperature (900^o) by a mixed He ion beam composed of 99.75% He, 0.2 H, and 0.05% C. Similar to the previous irradiation cases, the ion beam flux at the beam center was $3.2x10^{20}$ ion/m^2s and the irradiation was carried for 9 hours reaching a total ion dosage at the sample center of about $1.0x10^{25}$ ion/m^2 .The main observation after the irradiation is done was that the sample surface shows no change in its visible appearance. Unlike the cases of the pure He irradiation where the sample surface darkened by the formation of fuzzy layer and the other case of high carbon percentage irradiation where the surface was darkened by a formation of thick carbon film. In this case, after irradiation, the surface was still has a bright metallic appearance. The chemical composition of the sample surface after the irradiation was measured by XPS. A wide XPS survey for the irradiated sample (not presented) shows a typical W peaks with a little carbon peak without any other contaminants. The total carbon composition of the sample surface was found to be around 20%. More detailed look into the C1*s* and W4*f* of XPS spectral regions are presented in Figure VI.6 and VI.2h. The C1*s* region shown in figure VI.6 shows the presence of carbon on the surface. The carbon peak in this region was positioned at 283.2 eV. This peak position represents the most accepted peak position value for carbon in the form of WC. This finding emphasize that most carbon exist on the sample surface was actually in WC phase. Another shorter peak was needed to fit the higher binding energy side of the prominent WC peak as can be seen in Figure VI.6. This peak was found to be at 284.5, which represent the graphitic form of carbon. Thus, the XPS data in the C1s region shows that a major part of the surface carbon (63%) exists in WC phase and the remaining part (37%) was still in pure carbon (graphitic) phase. On the other hand, the W 4*f* region (figure VI.2-h) shows the coexistence of the W in a pure phase as well as in the carbide (WC) phase. Here, the presence of WC phase in the W 4*f* region confirms our finding in the C1s region.

The surface morphology of the irradiated sample was observed by SEM. As it can be seen in figure VI.2-c, the sample surface after irradiation was remarkably smooth without any distinctive features (compared to fuzz structured surface). This finding also confirms our previous observation of no visible

surface darkening was seen after irradiation. The reason behind the observed mitigation of the W fuzz formation might be due to the presence of WC on the sample surface.

(D) He^+ ion beam irradiation with 0.01% C ions:

The next W sample was irradiated by He ion beam with even lower carbon content. The goal of performing this irradiation is to see how the surface responds to less carbon contamination. This sample was also irradiated at 900^o C and by similar ion beam flux for similar ion fluence. The general appearance of the sample surface after irradiation shows no change in color similar to what we observed in the previous irradiation at higher carbon content. The sample surface composition after the irradiation process was measured by XPS. The wide XPS survey of the irradiated sample surface shows typical pure W peaks with very minor carbon peak. The total surface carbon composition was found to be less than 10%. More careful look into the C1*s* and the W4*f* regions are presented in figure VI.7 and VI.2(i). The XPS C1*s* region presented in figure VI.7 shows a minor presence of carbon in the form of WC with a peak positioned at 283.2 eV. This observation was also confirmed by the presence of WC peaks along with Pure W peaks in the W4*f* region as presented in figure VI.2(i).

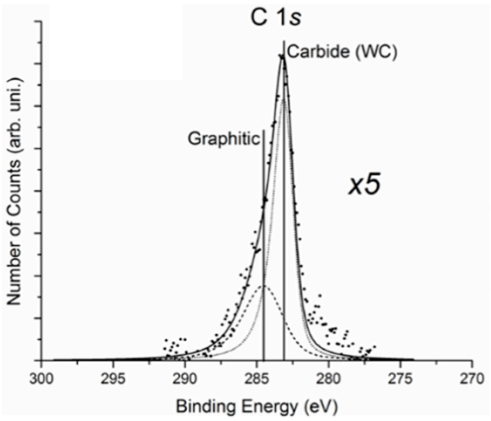

Figure VI.6: core level survey XPS spectra of 300eV He^+ ion with an impurity of 0.05% C irradiated, using 1×10^{25} ions m^{-2} ion fluence (with an ion-flux of 3×10^{20} ions m^{-2} s^{-1}), tungsten surface at 900°C.

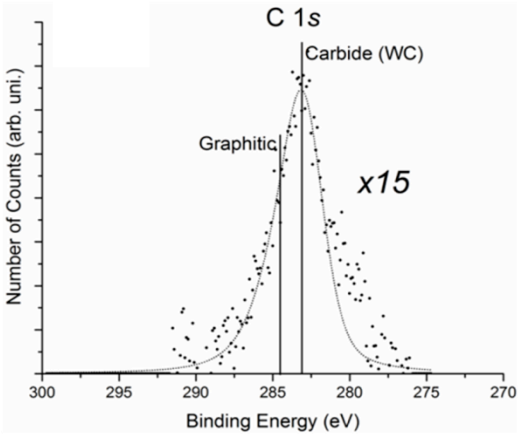

Figure VI.7: core level survey XPS spectra of 300eV He^+ ion with an impurity of 0.01% C irradiated, using 1×10^{25} ions m^{-2} ion fluence (with an ion-flux of 3×10^{20} ions m^{-2} s^{-1}), tungsten surface at 900°C.

The SEM images of the irradiated surface shows very interesting phenomena as presented in figure VI.8 a-c and VI.2d. The vast majority of the irradiated surface shows very good immunity against fuzz formation where the surface was found to be smooth with no fuzz formation. Only the W fuzz appears to grow in very limited and isolated area on the sample surface (fuzz islands). These fuzz islands were randomly dispersed on the sample surface with large variation in size, shape, and fuzz thickness. Figure VI.8-a shows an example for the vast majority of the sample surface where no W fuzz was formed in response to the mixed ion beam irradiation. SEM image of fuzzy islands is shown in Figure VI.8-b. As seen in this figure, the fuzzy island appears to grow in very limited area and surrounded by a smooth surface region. Similar structures were widely reported to form on a wide variety of W material grades after high fluxes of He plasma exposure [163,165,166,171,172]. It is also worthwhile to mention that not all of the fuzzy islands are having the same characteristics. Some of these islands are very thin and short (having short nano-fibers). Figure VI.8-c shows some examples for different fuzzy islands. The SEM image in figure VI.8-c shows a region of the surface were W fuzz was barely able to grow. In such regions, the surface exhibit the formation of dispersed very short nano-rods of W that grow above the surface and also surrounded by smooth areas.

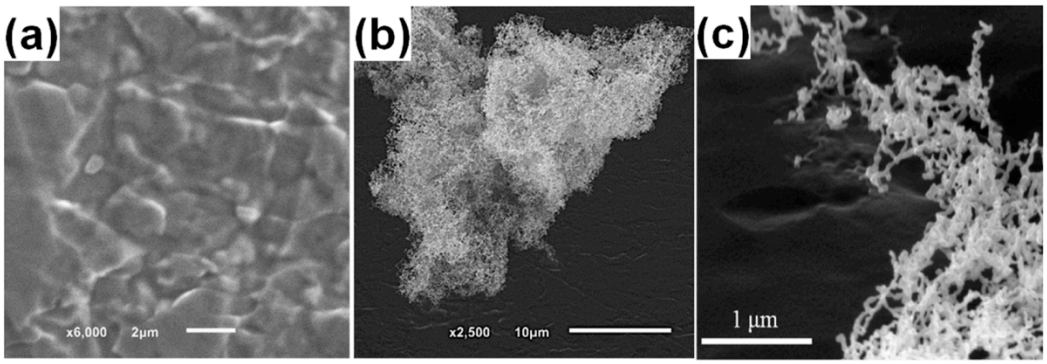

Figure VI.8: low and high resolution SEM image of 300eV He^+ ion with an impurity of 0.01% C irradiated, using 1×10^{25} ions m^{-2} ion fluence (with an ion-flux of 3×10^{20} ions m^{-2} s^{-1}), tungsten surface at 900°C (see text for more details).

Cross-sectional SEM image was made for one of the thickest fuzzy islands to take a closer look on the surface beneath the fuzz (Figure VI.9 a and b). As it can be seen in this image, the surface beneath the fuzz is still flat and smooth.

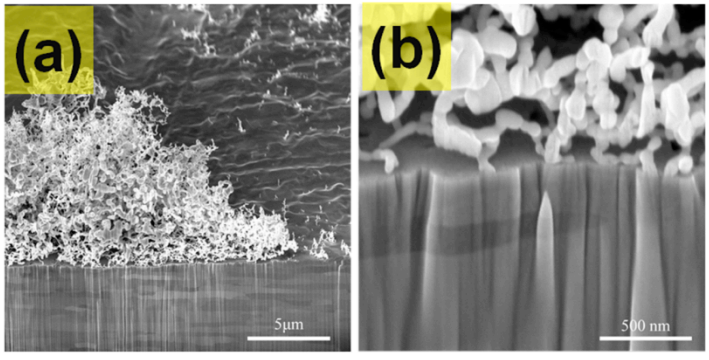

Figure VI.9: cross-sectional scanning electron microscopy (SEM) at 52° tilt using, focused ion beam (FIB) system, for 300eV He^+ ion irradiated W surface using 1×10^{25} ions m^{-2} fluence (with an ion-flux of 3×10^{20} ions m^{-2} s^{-1}) at 900°C. He^+, C^+, and H^+ ions ratio (at.%) are 99.95, 0.01, and 0.04 respectively.

Beside all of the different surface phenomena that we mentioned in this case of low carbon content He ion beam irradiation, in some limited areas, the surface also exhibit the formation of very long W nanoscopic fibers (nanowires-like) that tend to grow horizontally on the sample surface. These W nanowires were found to be always attached or very close to the fuzz covered areas. Most of these nanowires were branched into several nanowires, which altogether create what appears to be a network of nanowires covering the surface as seen in figure VI.10.

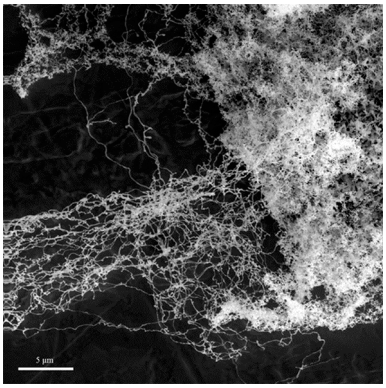

Figure VI.10: low resolution SEM image of 300eV He^+ ion with an impurity of 0.01% C irradiated, using 1×10^{25} ions m^{-2} ion fluence (with an ion-flux of 3×10^{20} ions m^{-2} s^{-1}), tungsten surface at 900°C (see text for more details).

The reason behind the formation of such nanowires under these conditions of He ions irradiation is not well understood. We believe that these nanowires is most likely formed due to the same mechanism of fuzz formation. The differences could be the fuzz root density. In the case of pure He irradiation, large number of W nano-rods was found to evolved above the surface with a high areal density (i.e., large number of nano-rods per unit of surface area). Due to the high number of these growing features, the rate of W atoms accumulation is to be distributed equally on all these features. Therefore, the average height of these growing parts of the surface is expected to be low. On the other hand, having much lower number of growing surface spots will results in high rate of growth and very long nano-fibers formation. In fact, the areal density dependence of the nano-rods length can be observed easily by comparing areal density of the nano-rods in thick fuzz islands (seen in the x-sectional SEM image presented in figure VI.9-a and b) to the areal density of the nano-rods that was formed in the case of pure He irradiation (presented in Figure VI.2-a). We believe that the factor dictates the areal density and the distribution of the growing surface spots is still not well understood.

(E) Pure H^+ ion beam irradiation:

The last sample was irradiated by a pure H ion beam at 900^o. The goal of performing this irradiation is to check whether the small percentage of the H in our previous irradiations will have any significance in terms of W surface morphology evolution. The H ion beam used in this sample irradiation experiment has a maximum flux at the beam center (sample center) of about $1.0x10^{21}$ ion/m^2s. The irradiation was carried for $1x10^4$ s giving a total H ion irradiation dose of about $1x10^{25}$ ion/m^2 at the sample center. The post-irradiation XPS measurement (not shown) shows nothing but a typical pure W sample with no contaminations. The sample also did not show any change in its physical appearance after the irradiation process. The post-irradiated surface appeared to have its original bright metallic finish without any darkening or discoloration. Low resolution SEM image show most of the sample surface was found to be clear with no distinctive features such as surface pinholes or blistering. Only in some very limited dispersed areas, the surface was found to form a kind of self-organized rippled structure as shown in figure VI.2e. This distinctive structure was found to be very frequent in many areas on the sample surface. The formation of this distinctive structure is most likely a crystal orientation dependent.

Summary

Several tungsten samples were irradiated by He ion beam with a various percentage of carbon ions. The W surface irradiated by pure He ion beam at elevated temperature exhibit the formation of wide spread W nano-fibers or fuzz. This phenomenon of He irradiation induced fuzz formation can be prevented in the presence of carbon contamination within the He ion beam. We found that, a thick graphitic like carbon layer was formed on W surface after irradiation by He ion beam mixed with 0.5% of carbon ions at 900^{o}C. The formation of such layer prevented the formation of W fuzz on the sample surface. Lowering the carbon ion percentage in the He ion beam by an order of magnitude (0.05% C) was also effective in preventing W fuzz formation. In this case of lower carbon content ion beam irradiation, much lower carbon composition reside on the sample surface and therefore, the formation of WC on the surface was the effective mechanism for W fuzz prevention. The effect of W fuzz prevention by WC formation on the sample surface was more noticeable when the sample was bombarded by He ion beam with even lower carbon ions content (0.01% C). In this case, the fuzz formation was prevented on the vast majority of the W sample surface. Also, W fuzz in this case was formed in limited and isolated areas dispersed randomly on the sample surface (fuzzy islands). W fuzz structure in such fuzz-covered areas was not uniform being thick in some areas and thin in others. We also observed the formation of very long W nano-fibers that appear to grow horizontally on the sample surface. The W surface shows very good resistance to morphology evolution when bombarded by high flux of pure H ions at 900^{o}C. In this case, the vast majority of the bombarded surface shows no changes after irradiation while a formation of self-organized rippled structure appears to form in very small and dispersed areas on the sample surface. More analysis is needed to fully understand W surface evolution and fuzz formation during He ion irradiation in the presence of minute carbon impurities.

VII. Chemical Compositional Analysis on Lithium Discharge Exposed Graphite and Silicon Samples – Work requested by GA for DIII-D

X-ray (XPS) and Auger electron (AES) spectroscopy studies

We performed these experiments at the surface characterization laboratory IMPACT of the Center for Materials Under Extreme Environment (CMUXE) at Purdue University. In the laboratory there is a set of three UHV chambers, which are connected to each other. The UHV chambers (~1.0×10^{-9} Torr) are equipped with a number of *in-situ* diagnostic tools for surface analysis, such as X-ray photoelectron (XPS), auger electron spectroscopy (AES), low energy ion scattering spectroscopy (LEISS), Extreme ultraviolet photoelectron spectroscopy (EUPS), and Extreme ultraviolet (EUV) reflectometer. In the present study, all the experiments were performed in the IMPACT-2 chamber (the schematic diagram is shown in Figure. VI.1).

XPS is a powerful technique to monitor the chemical states in the depth of 1-10 nm. It is the energy analysis of the photoelectrons created by X-ray radiation. This technique relies on the excitation of a material with a beam of X-rays and simultaneous measurement of the KE (kinetic energy) and number of the emitted electrons. The ability to perform XPS is valuable when studies regarding the chemical state of elements are of importance, since photoelectron lines shift when elements are in a chemically bound state compared to the pure element. These chemical shifts range from fractions of eV to a few eV. The resolution of chemical shifts is strongly dependent on the energy spread of the measured peak and the magnitude of the shift. The XPS spectra can be obtained within the top 1-10 nm of the analyzing material. The highest spatial resolution can be achieved by manipulating the X-ray source and/or detector parameters.

The X-ray source used in the IMPACT-2 system is a high intensity dual-anode (Mg and Al) optimized for XPS experiments. The anode base is made of silver to avoid any Cu-L_{α} stray radiation. The electron optics design of the anode and filament was made in such a way that the source housing

guarantees maximum X-ray intensity with very low cross-talk between the Mg and Al anodes. An Al radiation window that separates the anode volumes from the main chamber, is used to suppress Bremsstrahlung and to prevent the stray electrons (generated by the filament) to enter the energy analyzer. The main advantage of using a twin-anode is that the presence of two different excitation energies enables rapid distinction of Auger electron lines from photoelectron structures in a XPS spectrum. The Mg and Al anodes in the X-ray source are producing radiation lines at 1253.6 eV and 1486.6 eV, respectively. A flux of 10^{11}-10^{12} photons/sec emanates from the source, which translates into a photocurrent of 40 to 50 nA, depending of the material. The footprint of the X-ray beam can be changed by modifying the working distance, since the source is mounted on a z-manipulator. The natural line-width of the radiation is lower than 1eV, which is sufficient for XPS to determine binding energies of core levels within 0.2 eV. The X-ray source in IMPACT-2 is non-monochromatic and hence not collimated. So the X-rays flood the entire sample area (1×1 cm^2) and photoelectrons are emitted from all places in the sample. However, by maneuvering detector parameters high spatial resolution ~ 100µm is possible with our XPS.

During XPS measurements the photoelectrons were excited using a non-monochromatic X-ray source of *Mg-Kα* (energy=1253.6 eV) radiation source (SPECS XRC-1000) and the emitted photoelectrons were analyzed using Omicron Argus hemispherical electron analyzer using a round aperture of 6.3 mm. All experiments were performed at room temperature. The XPS spectra (figure VII.1) show the presence of O1s, C1s, and C1s peaks. However, in addition, we could observe one additional peak of Boron (may be some other element! as marked by question in the figure VII.1). The details are as below (Table VII.1). Our calculations, using Casa XPS, show ~ 12 at% Li in the sample.

Table VII.1: Binding energy (BE) and full width at half maxima (FWHM) found from Li1s, C1s and O1s peaks for Li witness sample.

S.N.	Component	BE (eV)	FWHM (eV)	Area	at%
1	Li1s	55.0	2.5	352.9	12.6
2	C1s	288.0	2.7	34310.9	72.7
3	O1s	535.0	2.9	19733.7	14.7

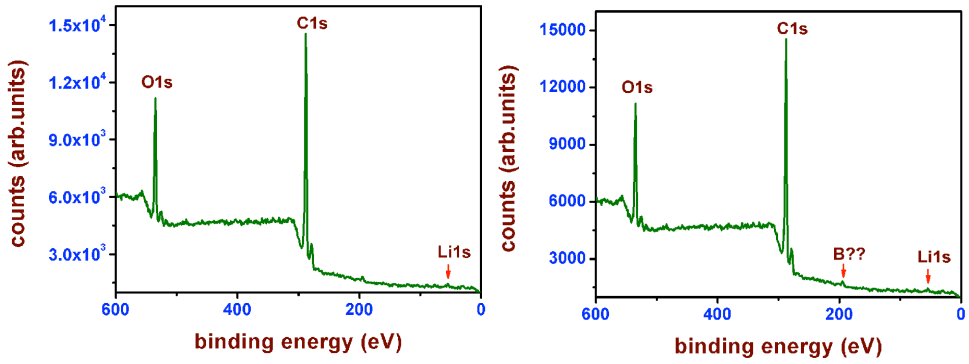

Figure VII.1. Core-level XPS spectra (top one, showing a?? mark for the presence of Boron, and below one is just the same spectra without a question mark) for Li witness sample.

We recorded the high-resolution XPS spectra as well for Li1s (figure VII.2), C1s (figure VII.3), and O1s (figure VII.4). These spectra were resolved into their respective components by a mixed Gaussian–Lorentzian (GL;m D 30) line-shape (where m D 0 is a pure Gaussian and m D 100 is a pure Lorentzian shape) using commercial CasaXPS peak fitting software. We could observe elemental Li, LiC_6, C-OLi,

C=O, and Carbonyl carbon in the above sample [173-176]. The details are described as below (Table VII.2).

Table VII.2: Fitting parameters [binding energy (BE) and full width at half maxima (FWHM) found from Li1s, C1s and O1s peak fitting for Li witness sample. Numbers inside small brackets in the BE column are the reference numbers in the list.

S.N.	Component	Li1s		C1s		O1s	
		BE (eV)	FWHM (eV)	BE (eV)	FWHM (eV)	BE (eV)	FWHM (eV)
1	Li	54.8 (1,3)	2.0				
2	LiC_6	58.6 (2)	2.6				
3	C-OLi			289.4 (3)	2.9	535.7 (3)	2.9
4	Carbonyl carbon			287.8 (4)	1.9		
5	C=O					534.9 (3)	2.1

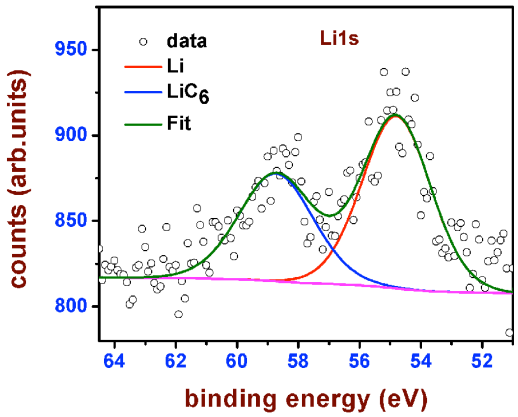

Figure VII.2. High resolution Li1s core-level XPS spectra (empty black circles) for Li witness sample. The spectra were fitted using commercial Casa XPS peak fitting software.

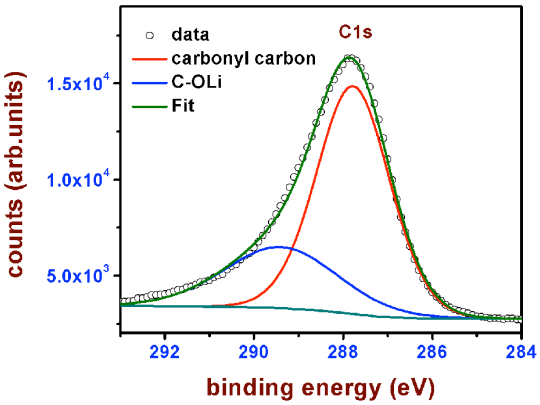

Figure VII.3. High-resolution C1s core-level XPS spectra (empty black circles) for Li witness sample. The spectra were fitted using commercial Casa XPS peak fitting software.

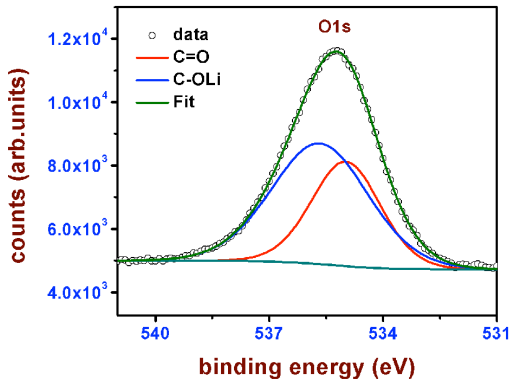

Figure VII.4. High-resolution O1s core-level XPS spectra (empty black circles) for Li witness sample. The spectra were fitted using commercial Casa XPS peak fitting software.

Another, popular technique for surface chemical element analysis is the AES. It cannot detect hydrogen or helium, but is sensitive to all other elements, being most sensitive to the low atomic number elements. Electrons of energy 3-5 keV are injected on a conducting surface and knock out core electron from an atom, resulting the creation of core hole. The atom then relaxes via electrons with a lower binding energy dropping into the core hole. The energy thus released by emitting an electron, which is called an Auger electron. After the emission of the Auger electron, the atom is left in a doubly ionized state. The line shape of core-valence-valence (CVV) spectrum is able to provide information about local chemical environment of the target atomic species. However, the CVV Auger intensity is commonly distorted due to losses such as elastic and inelastic scattering, interaction with collective oscillations (plasmons) and instrumental broadening. In fact, the types of electronic transitions during an Auger event are dependent on several factors, ranging from primary electron energy to relative interaction rates, though they are often dominated by a few characteristic transitions. Here in IMPACT we are using this technique with the help of an electron gun, where the emitted electrons are characterized by an electron analyzer. The Auger gun can produce electrons from 20 eV to 5000 eV. It can run with two different settings, either continuous running of the filament, or in constant current mode, which keeps a certain emission current. The emission current can be set up to 250 µA. Figure VII.5 shows the AES derivative spectra associated with Li KLL obtained from Li witness sample. Note that, since the kinetic energy of an Auger electron is independent of the type of primary beam (i.e. electrons or X-rays) and its energy, unlike the XPS the AES spectra were plotted on a kinetic energy scale. Further, since the AES peaks are superimposed on an important background of different types of secondary electrons, the AES spectra are represented in the differentiated (derivative) form. Figure VII.5 depicts the Auger peaks of Li at 40.5eV and 39.7eV [177,178].

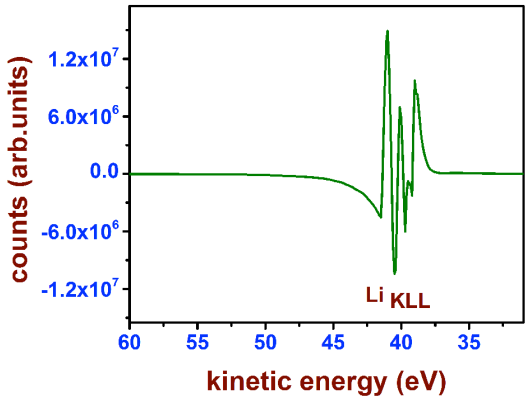

Figure VII.5. AES derivative spectra of Li KLL obtained from Li witness sample.

Laser induced breakdown spectroscopy (LIBS) studies

Laser induced breakdown spectroscopy (LIBS) was used to analyze the witness plate. Nd:YAG laser (1064 nm wavelength and 6 ns pulse duration) was used to ablate the sample with a spot size of ~ 1mm. Low laser pulse energy of 20 mJ was used for this sample. Plasma emission was spatially integrated and collected onto an optical fiber, which was connected to a spectrograph. A grating with 1200 grooves/mm was used for detecting Li emission at 670.7 nm. Figure VII.6 (a) shows Li emission after different number of laser shots. Emission intensity was highest after 1st laser shot and decreased after each laser shot. Li emission could be observed even after 20 laser shots, which shows considerable amount of Li layer deposited on the witness sample. Figure VII.6 (b) shows the integrated peak area for each laser shot. With proper calibration of the system using Li standards, LIBS signal intensity could be correlated to Li concentration on the witness plate.

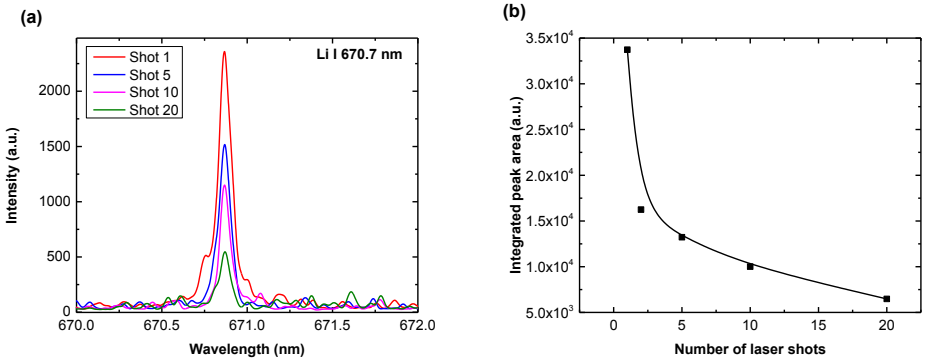

Figure VII.6. (a) Li (670.7 nm) signal intensity after different laser shots fired at the same location **(b)** Integrated peak area of Li for each laser shot. Laser pulse energy of 20 mJ was used for this study.

Figure VII.7 below shows the LIBS signal intensity obtained from 9 different locations on the witness plate. At each location five laser shots were fired and the signals from each laser shot was added together to obtain total Li signal intensity. It can be clearly seen that Li was uniformly distributed over different locations as measured using LIBS. For the 9 locations studied, relative standard deviation between the signal intensity was 7.1%.

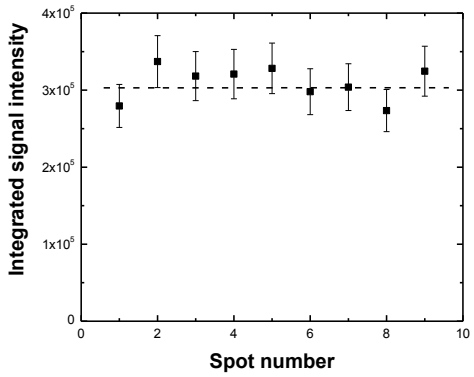

Figure VII.7. Li signal intensity measured at 9 different locations of the sample showing spatial homogeneity of the deposited Li on the witness sample. For each location, 5 laser shots were used and the signal intensity was added to obtain total Li signal.

Cross-section imaging using focused ion beam system:

To determine the thickness of the coated layer (Li in this case), cross-section imaging using dual beam focus ion beam/scanning electron microscope is an accurate tool. Figures VII.8(a) and 8(b) shows cross section secondary electron images of the coated layer. During the process, a 30 KeV Ga^+ beam is used (at a grazing angle) to create a rectangular cut in the sample. Then the cross-section is imaged using the combined electron microscope. The coated layer (Figure VII.8(b)) is uniform of ~ 1 µm.

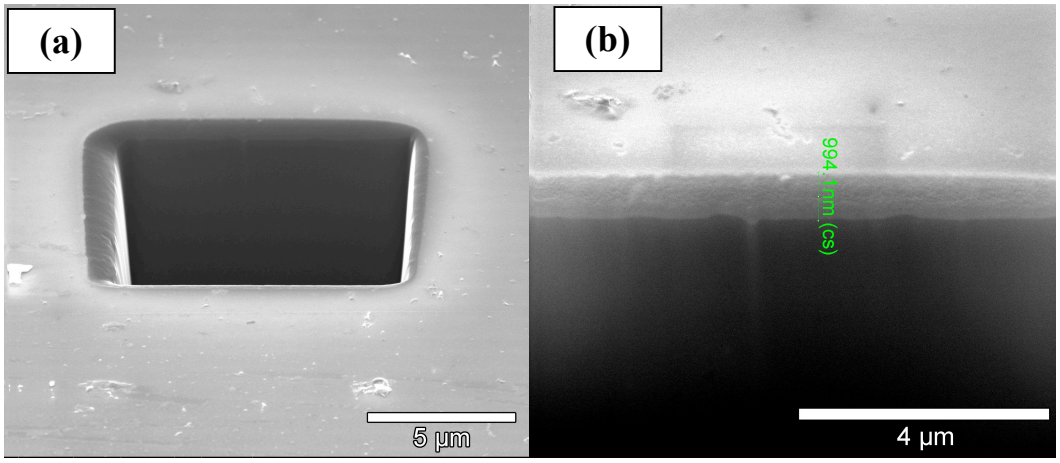

Figure VII.8. (a) Cross-section secondary electron image of the witness sample taken in a focus ion beam system. (b). Higher magnification cross-section secondary image showing a film thickness of ~ 1µm.

More detailed studies on additional samples

Analysis of witness samples using LIBS

Nd:YAG 1064 nm laser pulse at 25 mJ/pulse was used for ablating and analyzing the samples. Li neutral lines at 670.7 and 610.3 nm were used for analysis purposes. At least 6 locations on each sample was ablated and for each spot 10 laser shots were fired. Depending on the sample type, more than one shot was needed until no emission from Li was observed. For Control sample, 7-8 shots were needed while for sanded sample, Li signal was not visible after 2-3 shots. For Ethanol swipe as well as Ethanol_water sample, number of shots ranged from 4-6. Figure VII.9 below shows Li signal from single shot of different samples.

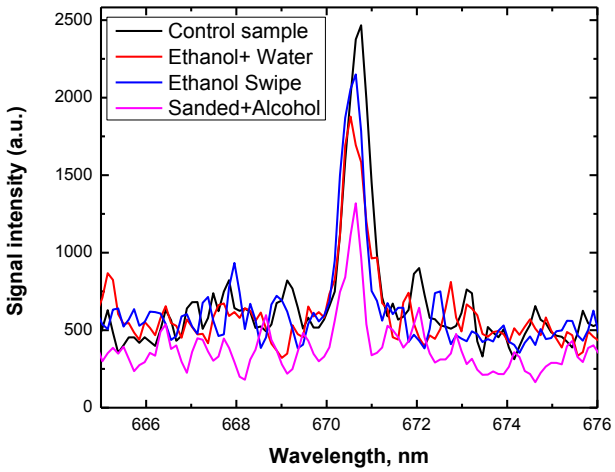

Figure VII.9. Li signal intensity from samples with different cleaning approaches.

Sanded sample showed lowest average Li signal although with large variability (~34%). There were some regions on the sanded sample where Li content was high while at other locations it was very low. Probably, non-uniform sanding as well as roughness of the sample could be reason for variability. A summary of Li signal from different samples is attached below in figure VII.10 and Table VII.3.

Table VII.3. Normalized Li content in Li witness samples.

	Normalized Li content
Control	**1**
Ethanol+Water	**0.713**
Ethanol Swipe	**0.839**
Sanded+Alcohol	**0.39**

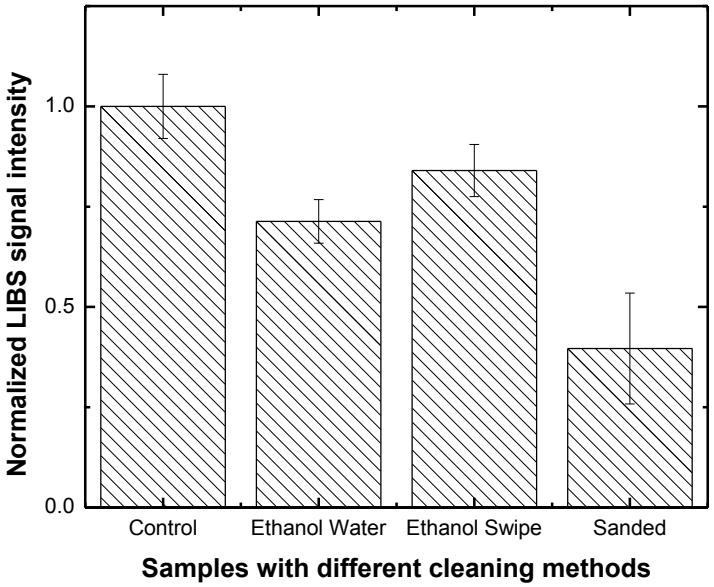

Figure VII.10. Normalized total integrated Li signal intensity from samples with different cleaning approaches. For each spot signal from multiple shots were added until no Li signal was observed. Error bars represent ± standard deviation.

X-ray photoelectron spectroscopy (XPS)

During XPS measurements the photoelectrons were excited using a non-monochromatic X-ray source of *Mg-Kα* (energy=1253.6 eV) radiation source (SPECS XRC-1000) and the emitted photoelectrons were analyzed using Omicron Argus hemispherical electron analyzer using a round aperture of 6.3 mm. All experiments were performed at room temperature. Though all of the four samples (control, Sanded_ Alcohol, Ethanol_swipe, and ethanol_water) show the evidence of Li, the amount of at% is significantly different from each other and minimum for ethanol_water sample. For evidence, the presence of at% of Li in control, sanded_ alcohol, Ethanol_swipe, and ethanol_water samples are 19.6, 12.8, 9.6, and 0.4 respectively (Table VII.4).

Table VII.4. at % of lithium, carbon, and oxygen in Li witness samples.

	Li1s	C1s	O1s
Control	**19.6**	66.4	14
Sanded_ Alcohol	**12.8**	83.5	3.7
Ethanol_swipe	**9.6**	74.9	15.5
Ethanol_ Water	**0.4**	82.1	17.5

Control Li witness sample

Figures VII.11(a) and VII.11(b)-(c) show the survey and high resolution (C1s, Li1s, and O1s) XPS spectra. These spectra were resolved into their respective components by a mixed Gaussian–Lorentzian (GL;m D 30) line-shape (where m D 0 is a pure Gaussian and m D 100 is a pure Lorentzian shape) using commercial CasaXPS peak fitting software. The relative atomic concentrations (at.%) of the components were calculated from the intensities of the respective spectral lines after background subtraction using Shirley's method. The results are summarized in table VII.5 and VII.6.

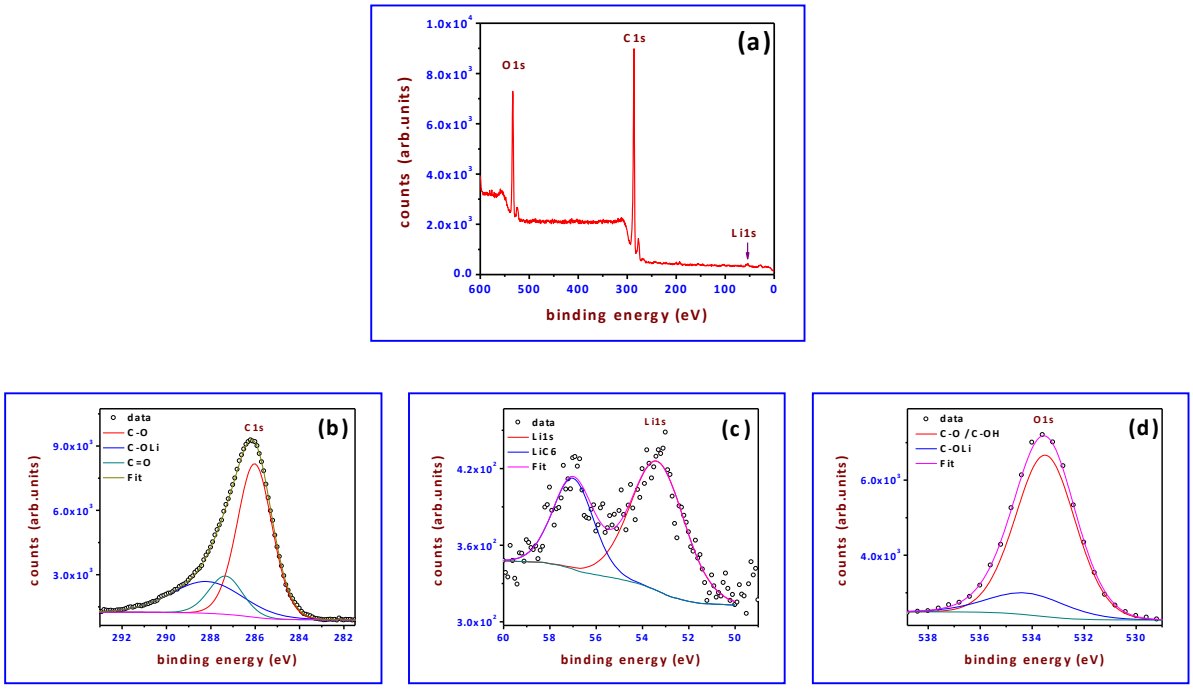

Figure VII.11. Survey (a) and high resolution (b, c, and d) core level XPS spectra for control Li witness sample.

Table VII.5. Binding energy (BE) and full width at half maxima (FWHM) found from Li1s, C1s and O1s peaks for control Li witness sample.

S.N.	Component	BE (eV)	FWHM (eV)	Area	at%
1	Li1s	53.6	1.5	425.4	19.6
2	C1s	286	2.6	24334.4	66.4
3	O1s	533.6	2.8	14641.3	14

Table VII.6. Fitting parameters [binding energy (BE) and full width at half maxima (FWHM) found from Li1s, C1s and O1s peak fitting for Control Li witness sample.

S.N.	Component	Li1s		C1s		O1s	
		BE (eV)	FWHM (eV)	BE (eV)	FWHM (eV)	BE (eV)	FWHM (eV)
1	Li	53.3	2.7				
2	LiC_6	56.9	2.1				
3	C-O			286.1	1.9	533.4	2.6
6	C-OLi			288.2	3.8	534.2	3.6
7	C=O			287.3	1.8		

Sanded_ alcohol Li witness sample

Figures VII.12(a) and VII.12(b)-(c) show the survey and high resolution (C1s, Li1s, and O1s) XPS spectra of Sanded_ Alcohol Li witness sample. Likewise the previous one these spectra were also resolved into their respective components by a mixed Gaussian–Lorentzian (GL;m D 30) line-shape (where m D 0 is a pure Gaussian and m D 100 is a pure Lorentzian shape) using commercial CasaXPS peak fitting software. The relative atomic concentrations (at.%) of the components were calculated from the intensities of the respective spectral lines after background subtraction using Shirley's method. The results are summarized in Table VII.7 and VII.8.

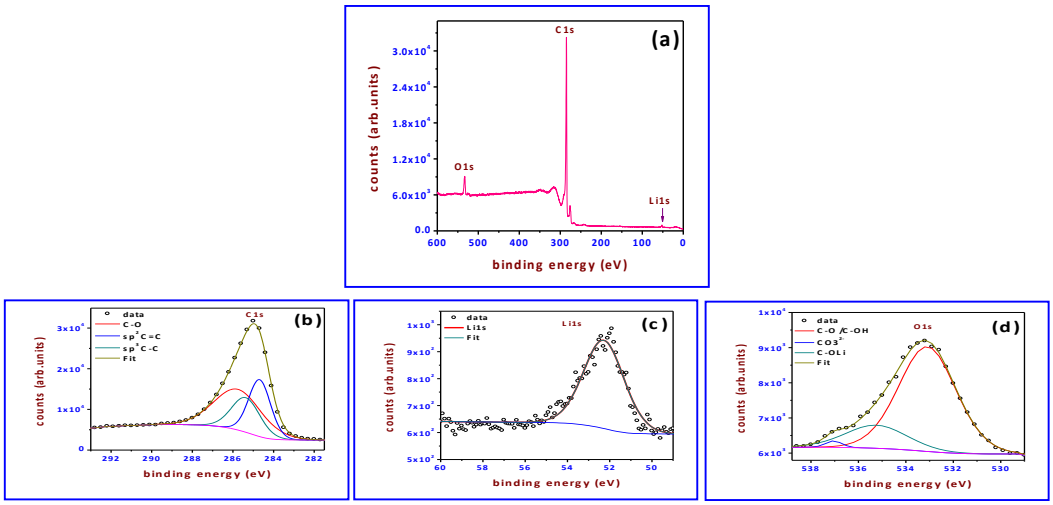

Figure VII.12. Survey (a) and high resolution (b, c, and d) core level XPS spectra for Sanded_ alcohol Li witness sample.

Table VII.7. Binding energy (BE) and full width at half maxima (FWHM) found from Li1s, C1s and O1s peaks for Sanded_ alcohol Li witness sample.

S.N.	Component	BE (eV)	FWHM (eV)	Area	at%
1	Li1s	52.0	1.7	740.9	12.8
2	C1s	285.0	2.1	81716.1	83.5
3	O1s	533.4	3.2	10291.3	3.7

Table VII.8. Fitting parameters [binding energy (BE) and full width at half maxima (FWHM) found from Li1s, C1s and O1s peak fitting for Control Li witness sample.

S.N.	Component	Li1s		C1s		O1s	
		BE (eV)	FWHM (eV)	BE (eV)	FWHM (eV)	BE (eV)	FWHM (eV)
1	Li	52.7	2.3				
3	C-O			285.8	2.7	533.1	2.8
4	Sp^2 C=C			284.7	1.2		
5	Sp^3 C-C			285.4	1.6		
6	C-OLi					535.3	3.1
8	CO_3^{2+}					537.1	0.8

Ethanol_swipe Li witness sample

Figures VII.13(a) and VII.13(b)-(c) show the survey and high resolution (C1s, Li1s, and O1s) XPS spectra of Sanded_ Alcohol Li witness sample. Likewise the previous one these spectra were also resolved into their respective components by a mixed Gaussian–Lorentzian (GL;m D 30) line-shape (where m D 0 is a pure Gaussian and m D 100 is a pure Lorentzian shape) using commercial CasaXPS peak fitting software.

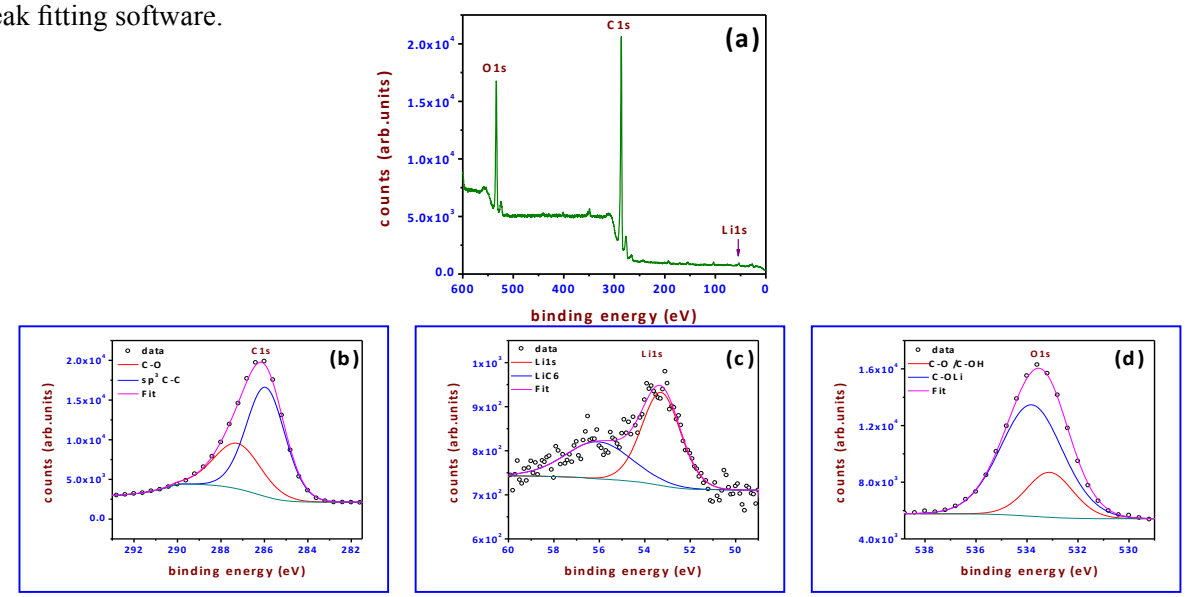

Figure VII.13. survey (a) and high resolution (b, c, and d) core level XPS spectra for Sanded_ Alcohol Li witness sample.

The relative atomic concentrations (at.%) of the components were calculated from the intensities of the respective spectral lines after background subtraction using Shirley's method. The results are summarized in Table VII.9 and VII.10.

Table VII.9. Binding energy (BE) and full width at half maxima (FWHM) found from Li1s, C1s and O1s peaks for Ethanol_swipe Li witness sample.

S.N.	Component	BE (eV)	FWHM (eV)	Area	at%
1	Li1s	53.2	1.8	410.6	9.6
2	C1s	286.2	2.6	53913.7	74.9
3	O1s	533.6	2.6	31628.6	15.5

Table VII.10. Fitting parameters [binding energy (BE) and full width at half maxima (FWHM) found from Li1s, C1s and O1s peak fitting for Control Li witness sample.

S.N.	Component	Li1s		C1s		O1s	
		BE (eV)	FWHM (eV)	BE (eV)	FWHM (eV)	BE (eV)	FWHM (eV)
1	Li	53.3	2.1				
2	LiC_6	56.1	3.4				
3	C-O			285.9	2.1	533.1	2.1
4	Sp^3 C-C			287.3	2.5		
5	C-OLi					533.8	2.8

Ethanol_water Li witness sample

Figures VII.14(a) and VII.14(b)-(c) show the survey and high resolution (C1s, Li1s, and O1s) XPS spectra of Sanded_ Alcohol Li witness sample. Likewise the previous one these spectra were also resolved into their respective components by a mixed Gaussian–Lorentzian (GL;m D 30) line-shape (where m D 0 is a pure Gaussian and m D 100 is a pure Lorentzian shape) using commercial CasaXPS peak fitting software. The relative atomic concentrations (at.%) of the components were calculated from the intensities of the respective spectral lines after background subtraction using Shirley's method. The results are summarized in Table VII.11 and VII.12.

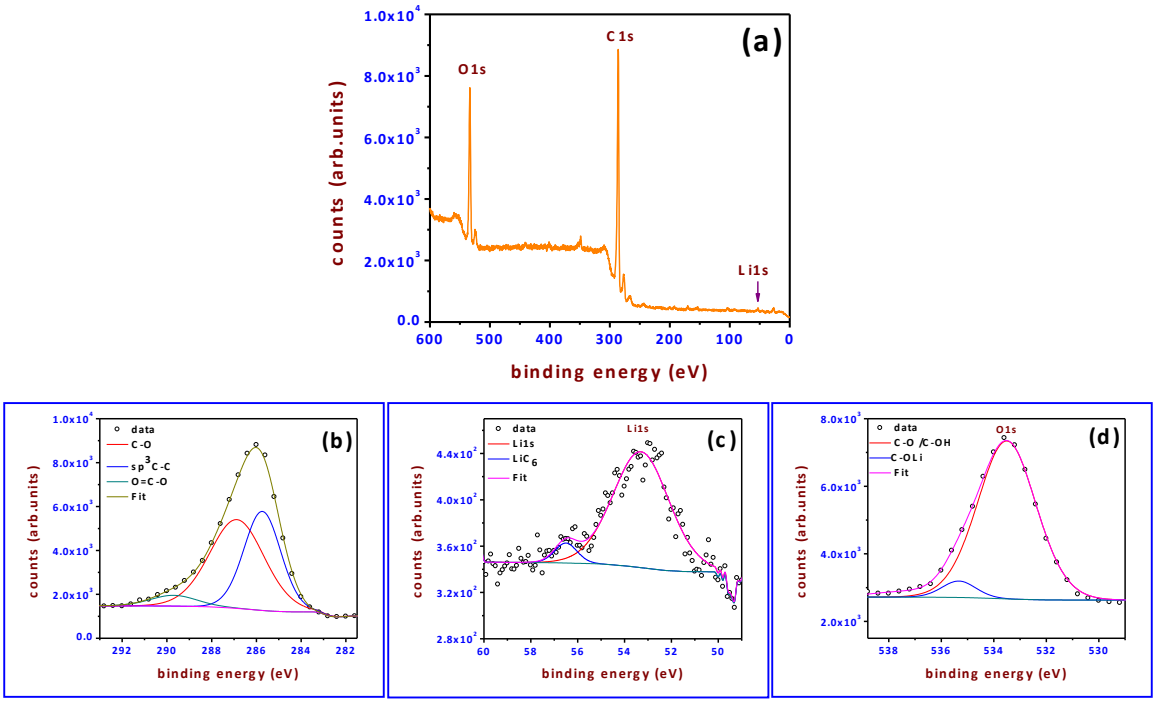

Figure VII.14. Survey (a) and high resolution (b, c, and d) core level XPS spectra for Sanded_ Alcohol Li witness sample.

Table VII.11. Binding energy (BE) and full width at half maxima (FWHM) found from Li1s, C1s and O1s peaks for Ethanol_water Li witness sample

S.N.	Component	BE (eV)	FWHM (eV)	Area	at%
1	Li1s	55.8	0.6	7.9	0.4
2	C1s	286.0	2.7	23661.7	82.1
3	O1s	533.4	2.7	14365.3	17.5

Table VII.12 Fitting parameters [binding energy (BE) and full width at half maxima (FWHM) found from Li1s, C1s and O1s peak fitting for Control Li witness sample.

S.N.	Component	Li1s		C1s		O1s	
		BE (eV)	FWHM (eV)	BE (eV)	FWHM (eV)	BE (eV)	FWHM (eV)
1	Li	53.3	2.8				
2	LiC_6	56.5	1.1				
3	C-O			286.8	2.8	533.5	2.6
4	Sp^3 C-C			285.7	1.8		
5	C-OLi					535.3	1.4
6	O=C-O			289.7	2.4		

Further studies on additional sanded and Di-vinegar_wiped samples

X-ray photoelectron spectroscopy (XPS)

We cleaned the same-sanded sample three times (on which we already performed XPS and LIBS studies previously), and labeled the sample as "Sanded_Alcohol_Twice", "Sanded_Alcohol_Thrice", "Sanded_Alcohol_Fourth". The XPS (and LIBS) has been performed after each cleaning. During XPS measurements the photoelectrons were excited using a non-monochromatic X-ray source of *Mg-Kα* (energy=1253.6 eV) radiation source (SPECS XRC-1000) and the emitted photoelectrons were analyzed using Omicron Argus hemispherical electron analyzer using a round aperture of 6.3 mm. All experiments were performed at room temperature. There is successive reduction in the Li at% after each sanding process, e.g., 8.9 at% (Sanded_ Alcohol_Twice) → 6.9 at% (Sanded_ Alcohol_Thrice)→ 6.5 at% (Sanded_ Alcohol_Fourth).

In addition, we performed XPS (and LIBS) in Di-Vinegar_Wiped [additional Li cleaning trail method. We clean one of the control sample using "Di-Vinegar_Wipe" and performed XPS (and LIBS)]. Interestingly, for Di-Vinegar_Wiped sample we observed 6.9 at% Li. For more details and comparison please see the Table VII.13.

Table VII.13. at % of lithium, carbon, and oxygen in Li witness samples

	Li1s	C1s	O1s	N1s
Control	**16.0**	74.6	8.2	1.2
Sanded_ Alcohol_First	**14.3**	68.2	15.4	2.1
Sanded_ Alcohol_Twice	**8.9**	86.6	4.5	-
Sanded_ Alcohol_Thrice	**6.9**	82.1	11	-
Sanded_ Alcohol_Fourth	**6.5**	88.6	4.9	-
Di-vinegar_wiped	**6.8**	77.4	15.8	-

Sanded_Alcohol_Twice Li witness sample

Figures VII.15(a) and VII.15(b)-(c) show the survey and high resolution (C1s, Li1s, and O1s) XPS spectra. These spectra were resolved into their respective components by a mixed Gaussian–Lorentzian (GL;m D 30) line-shape (where m D 0 is a pure Gaussian and m D 100 is a pure Lorentzian shape) using commercial CasaXPS peak fitting software. The relative atomic concentrations (at.%) of the components were calculated from the intensities of the respective spectral lines after background subtraction using Shirley's method. The results are summarized in table VII.14 and VII.15.

Table VII.14. Binding energy (BE) and full width at half maxima (FWHM) found from Li1s, C1s and O1s peaks for for **Sanded_Alcohol_Twice Li witness sample.**

S.N.	Component	BE (eV)	FWHM (eV)	Area	at%
1	Li1s	52.4	1.7	446.1	8.9
2	C1s	285.2	2.3	73380.3	86.6
3	O1s	533.2	3.2	11091.9	4.5

Table VII.15. Fitting parameters [binding energy (BE) and full width at half maxima (FWHM) found from Li1s, C1s and O1s peak fitting for **Sanded_Alcohol_Twice Li witness sample**

S.N.	Component	Li1s		C1s		O1s	
		BE (eV)	FWHM (eV)	BE (eV)	FWHM (eV)	BE (eV)	FWHM (eV)
1	Li	52.2	1.9				
2	LiC_6	54.0	5.1				
3	C-O			284.9	1.2		
6	C-OLi			289.2	2.5	533.2	3.0
7	C=O			285.7	2.8		
8	sp^2 C=C			284.1	0.9		

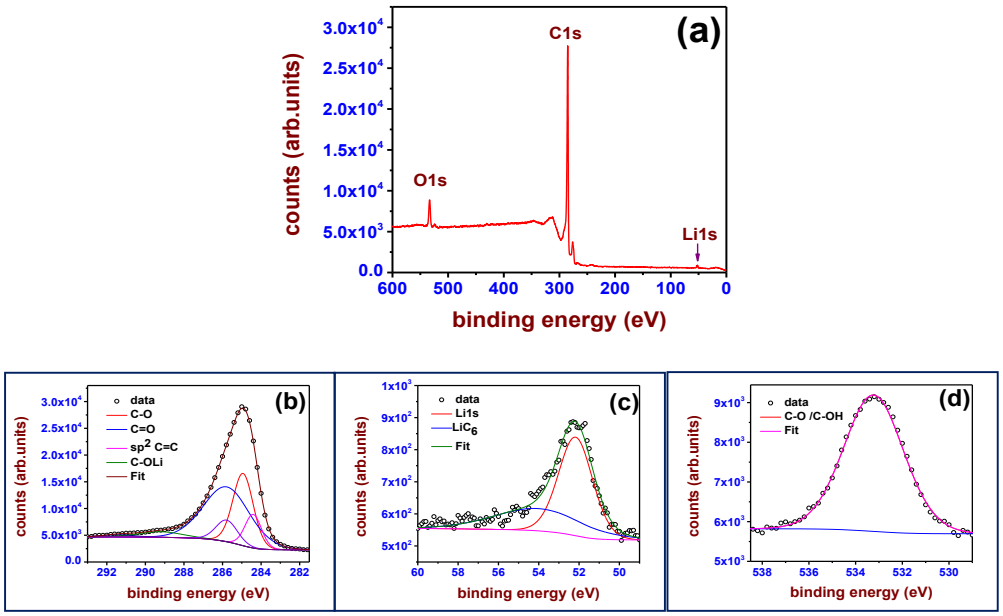

Figure VII.15. Survey (a) and high resolution (b, c, and d for C1s, Li1s and O1s respectively) core level XPS spectra for **Sanded_Alcohol_Twice Li witness sample.**

Sanded_Alcohol_Thrice Li witness sample

Figures VII.16(a) and VII.16(b)-(c) show the survey and high resolution (C1s, Li1s, and O1s) XPS spectra of Sanded_Alcohol_Thrice Li witness sample. Likewise the previous one these spectra were also resolved into their respective components by a mixed Gaussian–Lorentzian (GL;m D 30) line-shape (where m D 0 is a pure Gaussian and m D 100 is a pure Lorentzian shape) using commercial CasaXPS peak fitting software. The relative atomic concentrations (at.%) of the components were calculated from the intensities of the respective spectral lines after background subtraction using Shirley's method. The results are summarized in Table VII.16 and VII.17.

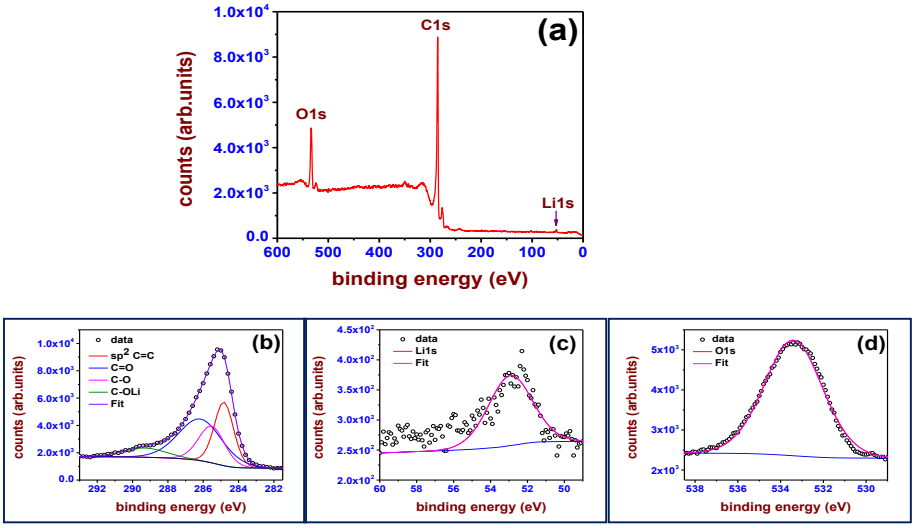

Figure VII.16. Survey (a) and high resolution (b, c, and d for C1s, Li1s and O1s respectively) core level XPS spectra for **Sanded_ Alcohol_Thrice Li witness sample.**

Table VII.16. Binding energy (BE) and full width at half maxima (FWHM) found from Li1s, C1s and O1s peaks for **Sanded_Alcohol_Thrice Li witness sample.**

S.N.	Component	BE (eV)	FWHM (eV)	Area	at%
1	Li1s	52.4	1.3	122.8	6.9
2	C1s	285.2	2.4	24329.3	82.1
3	O1s	534.0	3.4	9276.8	11

Table VII.17. Fitting parameters [binding energy (BE) and full width at half maxima (FWHM) found from Li1s, C1s and O1s peak fitting for **Sanded_Alcohol_Thrice Li witness sample.**

S.N.	Component	Li1s		C1s		O1s	
		BE (eV)	FWHM (eV)	BE (eV)	FWHM (eV)	BE (eV)	FWHM (eV)
1	Li1s	52.9	2.8				
3	C-O			285.5	1.2		
4	sp^2 C=C			284.8	1.2		
6	C-OLi			289.3	2.8	533.4	3.2
8	C=O			286.2	2.8		

Sanded_Alcohol_Fourth Li witness sample

Figures VII.17(a) and VII.17(b)-(c) show the survey and high resolution (C1s, Li1s, and O1s) XPS spectra of Sanded_Alcohol_Fourth Li witness sample. Likewise the previous one these spectra were also resolved into their respective components by a mixed Gaussian–Lorentzian (GL;m D 30) line-shape (where m D 0 is a pure Gaussian and m D 100 is a pure Lorentzian shape) using commercial CasaXPS peak fitting software. The relative atomic concentrations (at.%) of the components were calculated from the intensities of the respective spectral lines after background subtraction using Shirley's method. The results are summarized in Table VII.18 and VII.19.

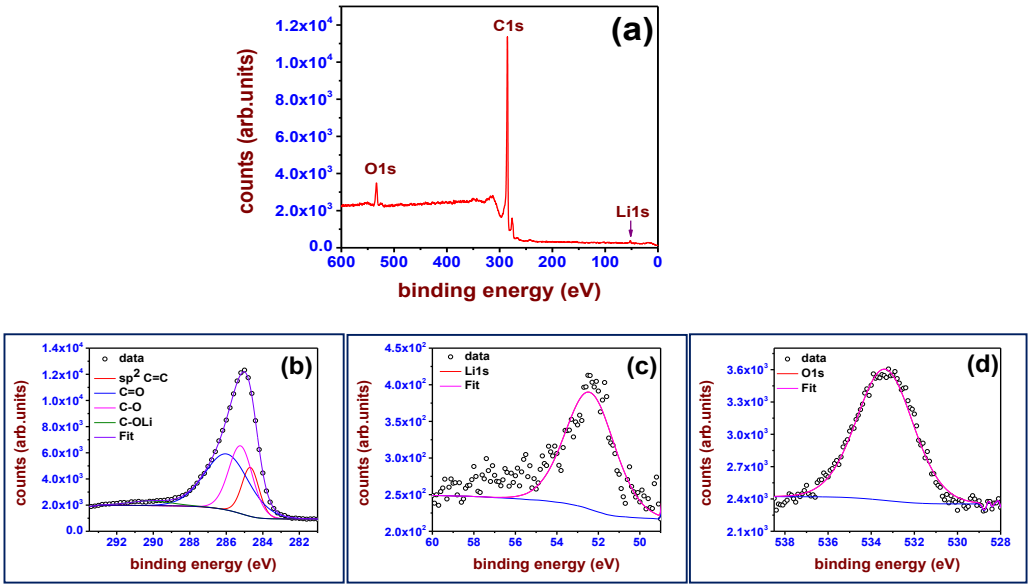

Figure VII.17. Survey (a) and high resolution (b, c, and d for C1s, Li1s and O1s respectively) core level XPS spectra for **Sanded_ Alcohol_Fourth Li witness sample**

Table VII.18. Binding energy (BE) and full width at half maxima (FWHM) found from Li1s, C1s and O1s peaks for **Sanded_Alcohol_Fourth Li witness sample**.

S.N.	Component	BE (eV)	FWHM (eV)	Area	at%
1	Li1s	52.4	1.3	117.8	6.5
2	C1s	285.2	2.2	27279.4	88.6
3	O1s	533.6	3.5	4359.0	4.9

Table VII.19. Fitting parameters [binding energy (BE) and full width at half maxima (FWHM) found from Li1s, C1s and O1s peak fitting for **Sanded_Alcohol_Fourth Li witness sample**

S.N.	Component	Li1s		C1s		O1s	
		BE (eV)	FWHM (eV)	BE (eV)	FWHM (eV)	BE (eV)	FWHM (eV)
1	Li	52.4	2.8				
3	C-O			285.2	1.5		
4	sp^2 C=C			284.6	1.1		
5	C-OLi			290.2	2.8	533.3	3.1
6	C=O			285.9	2.8		

Di-Vinegar_Wiped Li witness sample:

Figures VII.18(a) and VII.18(b)-(c) show the survey and high resolution (C1s, Li1s, and O1s) XPS spectra of Di-vinegar_wiped Li witness sample. Likewise the previous one these spectra were also resolved into their respective components by a mixed Gaussian–Lorentzian (GL;m D 30) line-shape (where m D 0 is a pure Gaussian and m D 100 is a pure Lorentzian shape) using commercial CasaXPS peak fitting software. The relative atomic concentrations (at.%) of the components were calculated from the intensities of the respective spectral lines after background subtraction using Shirley's method. The results are summarized in Table VII.20 and VII.21.

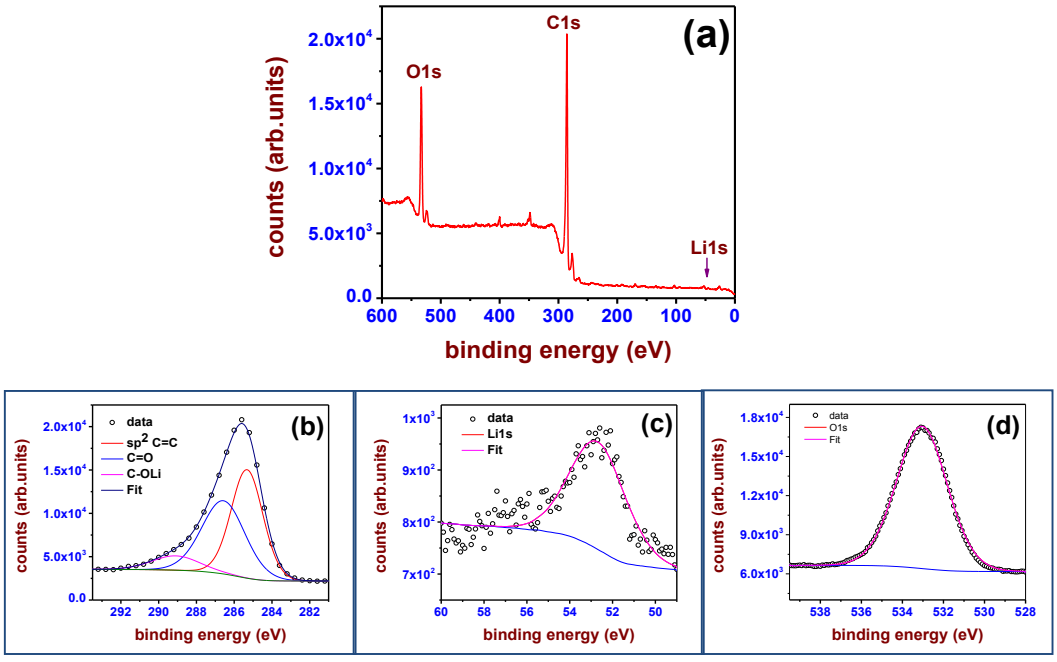

Figure VII.18 survey (a) and high resolution (b, c, and d for C1s, Li1s and O1s respectively) core level XPS spectra for **Di-Vinegar_wiped Li witness sample**

Table VII.20. Binding energy (BE) and full width at half maxima (FWHM) found from Li1s, C1s and O1s peaks for **Di-Vinegar_wiped Li witness sample**

S.N.	Component	BE (eV)	FWHM (eV)	Area	at%
1	Li1s	52	1.9	299.3	6.8
2	C1s	285.6	2.7	57069.7	77.4
3	O1s	533.2	3.0	33158.3	15.8

Table VII.21. Fitting parameters [binding energy (BE) and full width at half maxima (FWHM) found from Li1s, C1s and O1s peak fitting for **Di-Vinegar_wiped Li witness sample**

S. N.	Component	Li1s		C1s		O1s	
		BE (eV)	FWHM (eV)	BE (eV)	FWHM (eV)	BE (eV)	FWHM (eV)
1	Li	52.7	3.0				
4	sp^2 C=C			285.3	1.8		
5	C-OLi			289.1	2.9	533.1	2.9
6	C=O			286.5	2.6		

Laser-induced breakdown spectroscopy (LIBS)

We ablated following samples: Control, sanded twice, sanded four times and Vinegar wiped sample as described in the text above and analyzed LIBS signal.

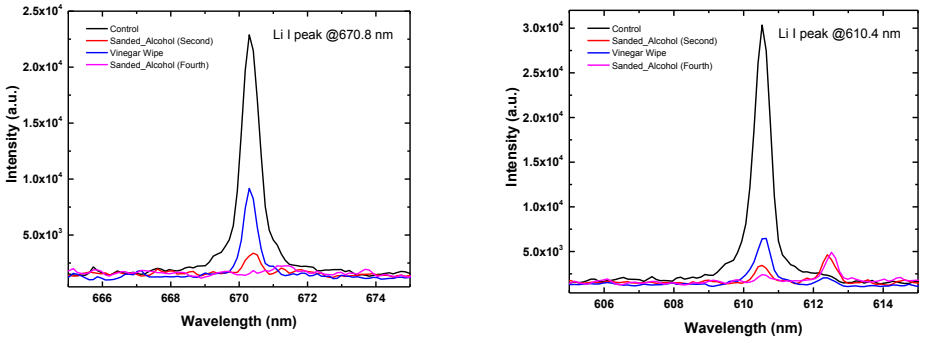

Figure VII.19. Li I LIBS emission peaks at 610.4 nm and 670.8 nm for samples after different treatments.

Two Li I peaks were analyzed- 610.4 nm and 670.8 nm. The reason two peaks were analyzed because at low Li sample content 670.48 nm peak was not sensitive enough to show the signal. Both the peaks from all the 4 samples are shown in Figure VII.19. It can be clearly seen that vinegar wipe did help in

reducing the Li content significantly. But sanding the sample proved to be most effective. By sanding four times as described above, Li signal was reduced by ~99% as compared to control sample (shown in table and figure below). It has to be added that this reduction does not confirm that all the Li is removed from the sample as Li signal might be below the detection limit of LIBS system. Although, Li is drastically reduced due to effective sanding. A combination of vinegar wipe and sanded sample can be a suggested way of completely removing Li from the sample.

Sample	Normalized integrated signal (610.4 nm)
Control	1
Sanded Twice	0.026
Sanded Fourth	0.013
Vinegar Wipe	0.180

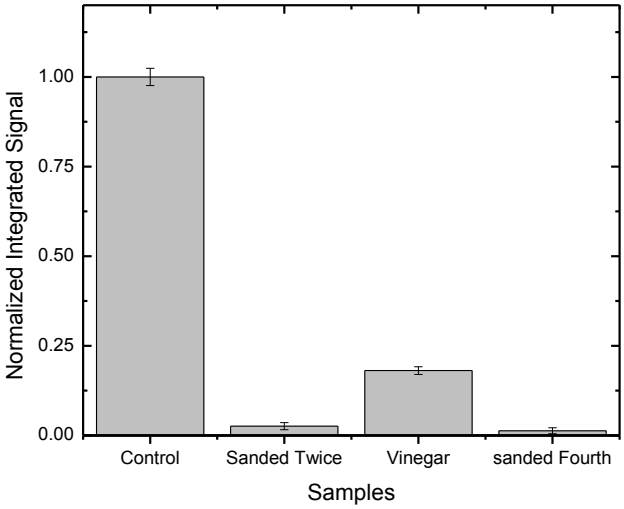

Figure VII.20. Normalized LIBS integrated signal for different samples. Signal was normalized to control signal. Signal here is defined as total integrated Li signal (610.4 nm) after background correction.

VIII. Recrystallization and Grain Growth Induced by ELMs-like Transient Heat Loads in Deformed Tungsten Samples

Tungsten has been chosen as the main candidate for plasma facing components (PFCs) due to its superior properties under extreme operating conditions in future nuclear fusion reactors such as ITER. One of the serious issues for PFCs is the high heat load during transient events such as ELMs and disruption in the reactor. Recrystallization and grain size growth in PFC materials caused by transients are undesirable changes in the material, since the isotropic microstructure developed after recrystallization exhibits a higher ductile-to-brittle transition temperature which increases with the grain size, a lower thermal shock fatigue resistance, a lower mechanical strength, and an increased surface roughening. This study was focused on careful determination of the threshold parameters for surface recrystallization, grain growth rate, and thermal shock fatigue resistance under ELM-like transient heat events. Transient heat loads were simulated using long pulse laser beams for two different grades of ultrafine-grained tungsten. It was observed that cold rolled tungsten demonstrated better power handling capabilities and higher thermal stress fatigue resistance compared to severely deformed tungsten. Higher recrystallization

threshold, slower grain growth, and lower degree of surface roughening were observed in the cold rolled tungsten [179].

In order to determine the threshold parameters, surface modification, and grain size evolution after recrystallization with increasing heat flux parameter, we conducted the power scan experiment with surface power density ranging from 0.49 GW/m^2 to 1.5 GW/m^2. Surface modification, grain size evolution, and thermal shock fatigue resistance under repetitive transient heat events were investigated in the pulse number experiment with the number of laser pulses increasing from 1 up to 1000 at the fixed power density.

Experimental setup

A long pulse neodymium-doped yttrium aluminum garnet (Nd:YAG) laser (GSI Lumonics) operating at 1064 nm and at 1 Hz repetition rate with a pulse width of 1 ± 0.1 ms was used to simulate the transient heat load events on the samples. All the experiments were performed at the base pressure ~ 10−5 Torr in a high vacuum chamber. To provide the same experimental conditions for each shot during the power load scan experiments, as well as during the pulse number scan experiments, all or most of the shots were done on the same target mounted on an XY translational stage. All the experimental runs were carried out at room temperature. The laser beam was allowed to pass through a window of the chamber and focused perpendicularly on the sample surface using a focusing lens (f = 40 cm) with a spot diameter of ~1 mm.

Materials characterization

For analyzing the surface modification, microstructure and grain size high resolution scanning electron microscopy (SEM) was performed using a Hitachi S4800 FESEM. Cross-sectional imaging was performed using an FEI Nova 200 NanoLab Dual Beam Focused ion beam/scanning electron microscope (FIB/SEM). Local crystallographic texture and grain boundary misorientation was acquired using electron backscatter diffraction (EBSD) on FEI XL-40 scanning electron microscope.

Results

The microstructure of the severely deformed tungsten by chip formation is summarized in Fig. VIII.1. The TEM image, shown in Fig. VIII.1(a) clearly shows the highly refined structure in this sample; grains as small as 50 nm can also be seen. The inset to Fig. VIII.1(a) shows the diffraction pattern from the area in the image; the arc shaped patterns are indicative of the preferred crystallographic (texture) in the sample. The cross-sectional SEM images in Fig. VIII.1(b) demonstrates that the grains in the severely deformed tungsten before laser-induced recrystallization were elongated and at an angle of around 45 degrees from the sample surface. The EBSD analysis of the sample surface is shown in Fig. VIII.1(c). The microstructure is primarily comprised of low-angle (<15^0) grain boundaries, as evident from the boundary misorientation plot. The pole figures also showed two partial texture fibers: <111> fiber and <110> fiber. These texture components arise as a result of simple shear deformation in machining.

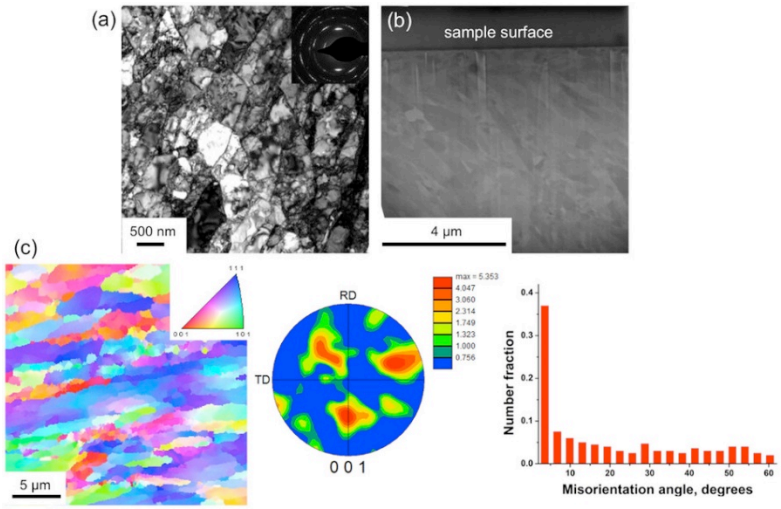

Figure VIII.1: Starting microstructure of severely deformed tungsten: (a) bright-field TEM image, (b) SEM image of the sample cross-section and (c) EBSD analysis (scan step size 0.2 mm).

Figure VIII.2 summarizes the cold rolled sample microstructure. Elongated, pancaked microstructure can be seen in Figs. VIII.2(a) and (b). The level of microstructure refinement in this sample is smaller than that seen in the severely deformed sample (Fig. VIII.1). The microstructure in this case can be seen to consist of elongated grains, 500 nm in width, which are further comprised of dislocation substructures within. The expected deformation strain imposed in these samples is lower compared to severely deformed samples. Grains in the cold rolled sample before laser irradiation were elongated and parallel to the sample surface (Fig. VIII.2 (b)). As evident from the EBSD analysis (Fig. VIII.2(c)), the microstructure indeed consisted of a large fraction (,0.4) of lowangle boundaries, similar to that observed in the severely deformed sample. The pole figures showed that the predominant texture component is the {001}<110> fiber.

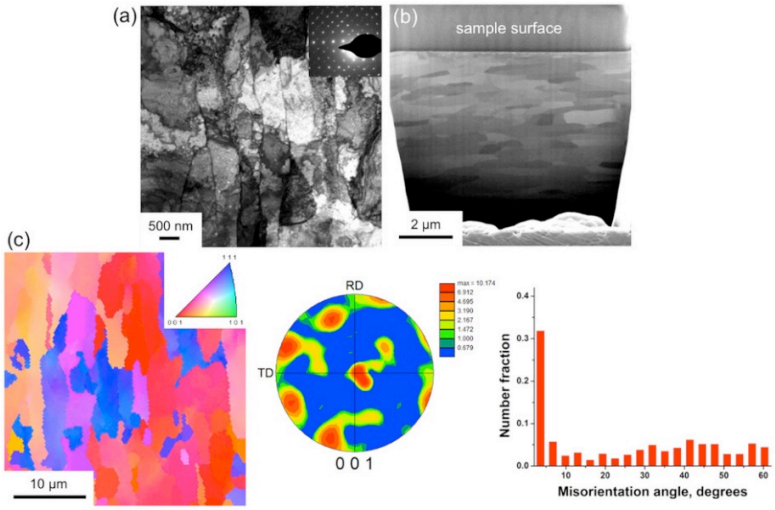

Figure VIII.2: Starting microstructure of cold rolled tungsten: (a) bright-field TEM image, (b) SEM image of the sample cross-section and (c) EBSD analysis (scan step size 0.25 μm).

Recrystallization. From the SEM and EBSD observations of the laser spots on the samples surface, the recrystallization heat flux threshold was found to be 15.4 MJ/m^2 s$^{1/2}$ for the severely deformed tungsten samples and 24.7 MJ/m^2 s$^{1/2}$ for the cold rolled tungsten ones. Figure VIII.3 shows the recrystallized microstructures of the severely deformed and cold rolled samples at these heat fluxes. As seen from the EBSD images, the microstructure transforms into equiaxed type, accompanied with increase in the fraction of high angle grain boundaries. Beyond the threshold heat flux, the recrystallized grain size was found to increase with the power load, as well as the number of pulses.

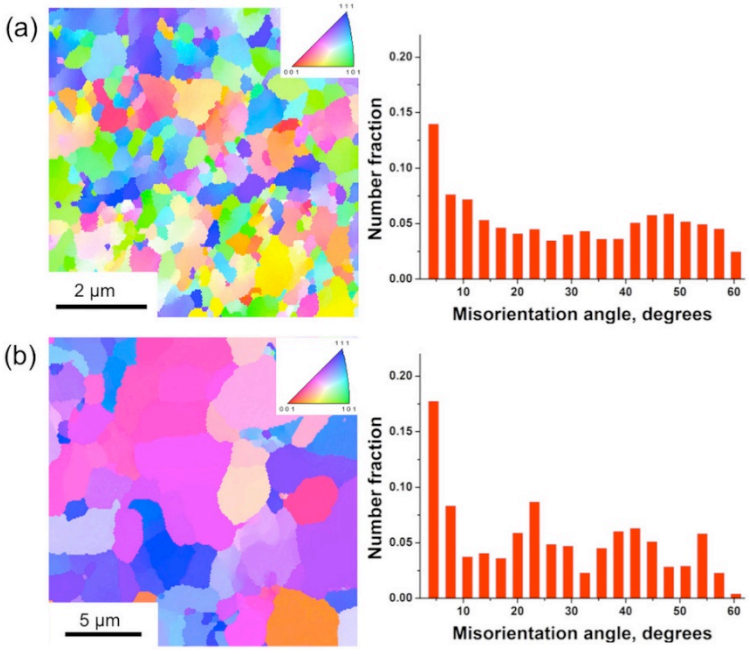

Figure VIII.3: Recrystallized microstructure (IPF map) and grain boundary misorientation distribution for (a) severely deformed tungsten after 100 shots at heat flux F = 15.4 MJ/m^2 s$^{1/2}$ (scan step size 0.05 μm) and (b) cold rolled tungsten after 100 shots at heat flux F = 24.7 MJ/m^2 s$^{1/2}$ (scan step size 0.15 μm).

Grain growth during power scan experiment: Figure VIII.4 shows the grain size evolution with increasing power density. It was observed for both types of tungsten samples that the grain size decreases radially from the recrystallized center outward, following the thermal gradient. The difference in grain sizes becomes more noticeable at higher heat fluxes. The corresponding grain sizes in the center and the edge of the irradiation spot are shown in the figure. The dashed lines show the average grain size trend. As seen in the figure, the average grain size of the severely deformed tungsten sample is larger than that of the cold rolled sample. Moreover, the grain size for the severely deformed tungsten sample seems to level off at higher power fluxes when surface melting occurs, whereas the grain size of the cold rolled sample continues to rise steadily without any sign of melting. Surface melting and crack formation was observed in severely deformed tungsten at heat fluxes above F= 36.3 MJ/m^2 s$^{1/2}$.

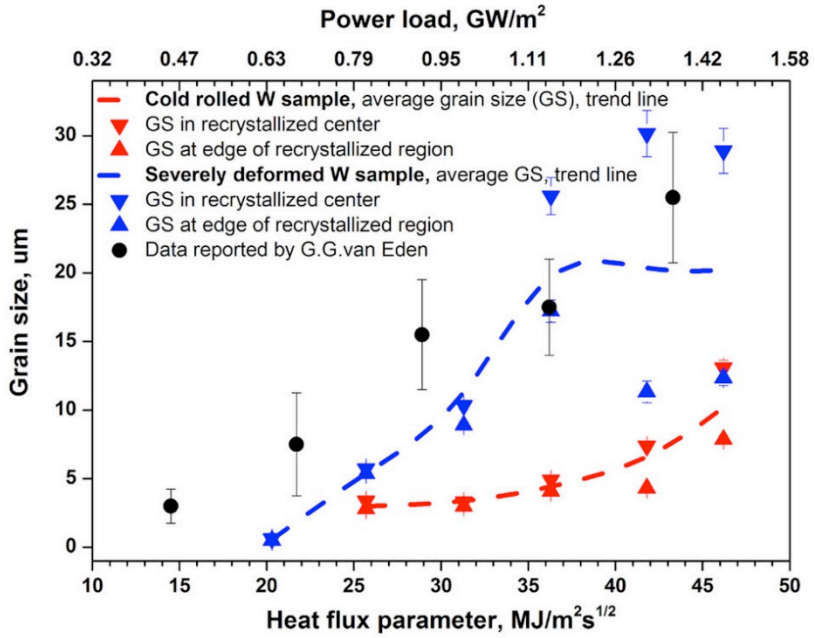

Figure VIII.4: Grain size evolution with power load in severely deformed and cold rolled tungsten samples

The grain size evolution with the number of laser pulses for both types of tungsten samples is shown in Figure VIII.5. Recrystallization after the first laser pulse was observed for both types of tungsten samples, indicating the extremely short (~millisecond) timescales of the thermally activated transformation processes. As evident from the figure, the average grain size increases with the number of pulses, accompanied by increasing grain size gradient from the center of the recrystallized region to its edge. The grain size of the severely deformed tungsten is greater than that of the cold rolled sample up to 250 pulses, and then seems to level off at increased number of pulses. In contrast, cold rolled tungsten exhibited a continuous grain size growth (albeit with decreasing rate) with the number of laser pulses (up to 1000 pulses). In summary, the propensity for grain growth with increasing power load or repeated pulse events is evidently more in the severely deformed samples compared to the cold rolled samples. Moreover, the cold rolled tungsten samples exhibited a low degree of surface roughening and no surface melting or crack formation, indicating its overall higher thermal shock fatigue resistance.

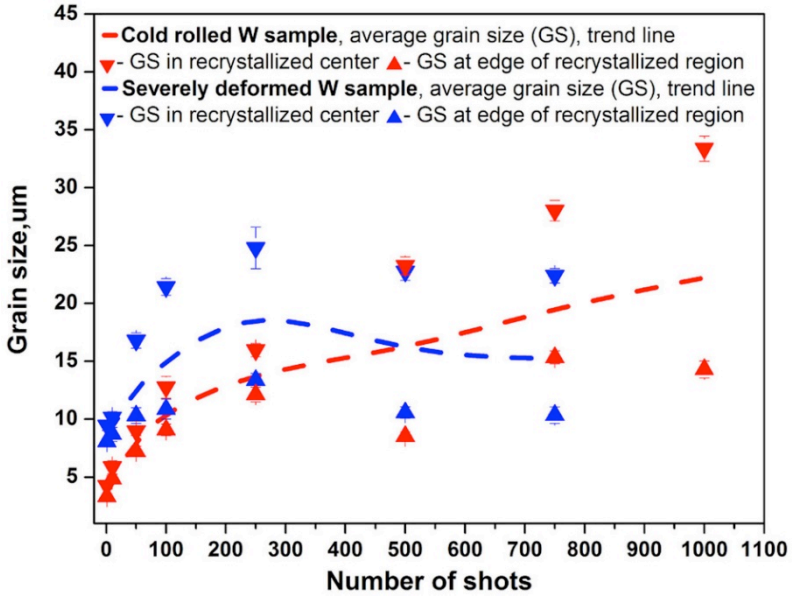

Figure VIII.5: Grain size evolution with number of pulses at a fixed heat flux of 35.7 MJ/m^2 s$^{1/2}$

Under large power loads or large number of pulse events, significant surface roughening of the recrystallized material has been observed in both the severely deformed and cold rolled samples. This is attributed to the repeated plastic deformation of the sample surface. Figures VIII.6 and VIII.7 show this phenomenon in the severely deformed and cold rolled tungsten, respectively. At 100 pulses exposure, appreciable changes in the surfaces morphology were first observed at F = 31.3 MJ/m^2 s$^{1/2}$. For the severely deformed tungsten samples, surface melting and cracking occurred when the heat flux parameter exceeded 36.3 MJ/m^2 s$^{1/2}$with a smooth, fully recrystallized surface inside the molten (and solidified) pool and some roughness outside the pool (Fig. VIII.6(b)).

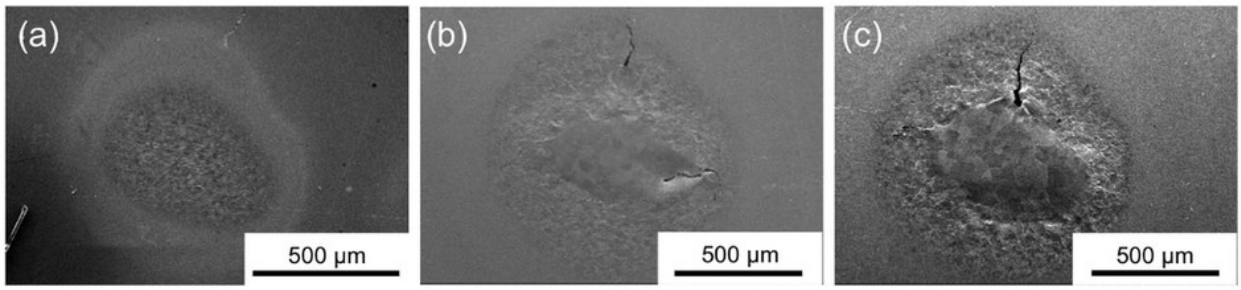

Figure VIII.6: Surface morphology evolution for severely deformed tungsten at heat flux parameter of (a) 31.3 MJ/m^2 s$^{1/2}$, (b) 41.8 MJ/m^2 s$^{1/2}$ and (c) 46.2 MJ/m^2 s$^{1/2}$.

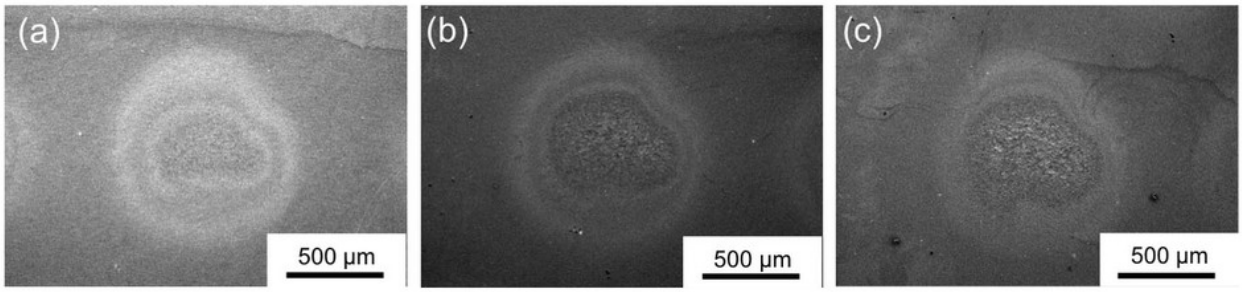

Figure VIII.7: Surface morphology evolution for severely deformed tungsten at heat flux parameter of (a) 31.3 MJ/m^2 s$^{1/2}$, (b) 41.8 MJ/m^2 s$^{1/2}$ and (c) 46.2 MJ/m^2 s$^{1/2}$.

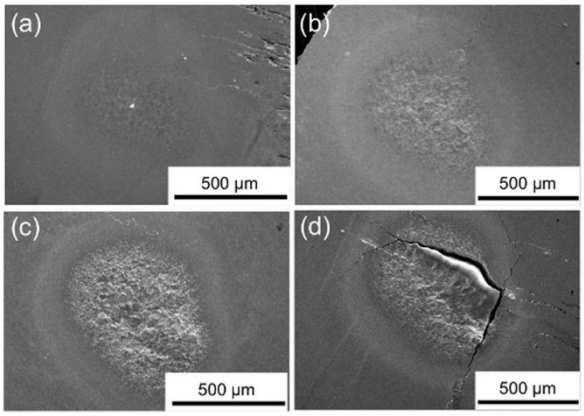

Figure VIII.8: Surface morphology evolution with number of laser pulses for severely deformed tungsten: (a) 10 pulses, (b) 100 pulses, (c) 250 pulses, and (d) 750 pulses.

The effect of increasing the number of pulses at a fixed heat flux F = 35.7 MJ/m^2 s$^{1/2}$, on surface morphology is shown in Figs. VIII.8 and VIII.9 for severely deformed and cold rolled tungsten, respectively. Surface morphology was altered to a higher degree with increasing number of pulses compared to increased power load. As evident from the figures, considerably faster surface roughening with the number of laser pulses was observed for the severely deformed tungsten compared to the cold rolled tungsten. Moreover, micro-scale cracks and surface melting occurred in the severely deformed tungsten samples at larger number of laser pulses. This observation again suggests the better power handling properties and thermal shock resistance of cold rolled samples compared to severely deformed samples.

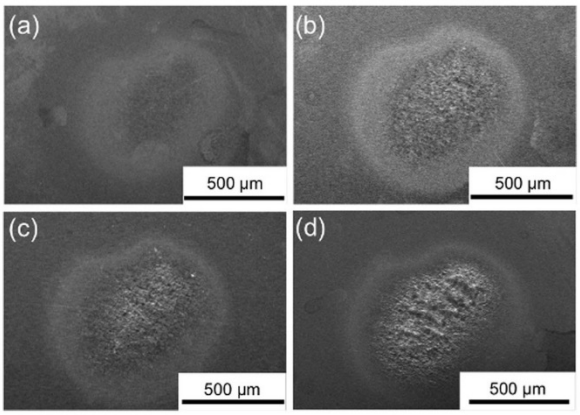

Figure VIII.9: Surface morphology evolution with a number of laser pulses for cold rolled tungsten: (a) 1 pulse, (b) 250 pulses, (c) 500 pulses, and (d) 1000 pulses.

IX. Models Extension: Model to Estimate Fractal Dimension for Ion-bombarded Materials

Comprehensive fractal Monte Carlo model ITMC-F [180] was developed based on the Monte Carlo ion bombardment simulation code, i.e., Ion Transport in Materials and Compounds (ITMC) code [181]. The ITMC-F studies the impact of surface roughness on the angular dependence of sputtering yield. Instead of assuming material surfaces to be flat or composed of exact self-similar fractals in simulation, we developed a new method to describe the surface shapes. Random fractal surfaces, which are generated by midpoint displacement algorithm and support vector machine algorithm are combined with ITMC. With this new fractal version of ITMC-F, we successfully simulated the angular dependence of sputtering yield for various ion-target combinations, with the input surface roughness exponent directly depicted from experimental data [182]. The ITMC-F code showed good agreement with the experimental data. In advanced, we compare other experimental sputtering yield with the results from ITMC-F to estimate the surface roughness exponent for ion-bombarded material in this research.

Model and methods

We used mid-point displacement algorithm [183] and support vector machine to generate fractal Brownian motion with values of roughness exponents obtained from experimental results. Fractional Brownian motion (fBm) is based on Brownian motion concept. Brownian motion is the simplest continuous-time stochastic process, which has an expectation equals zero and the variance equals time. Fractional Brownian motion is also a continuous-time process that starts at zero. The difference between Brownian motion and fBm is that the increments are independent in Brownian motion, however they are dependent in fBm by covariance function [183].

By using the experimental value, we can construct a rough surface corresponding to their target, and then obtain sputtering yields from simulating ions bombardment on these surfaces. We benchmarked our model with three different experimental data. Since our benchmark results have good agreement with experimental value, and have the same trend [182] with the simulation work given in [184] and in [185], we can use our model to estimate the roughness exponent that no experiments have predicted before. Now we construct material surfaces with roughness exponent from 0.05, 0.06, 0.07,. . .0.95 as one testing series to predict what is the most suitable value for the corresponding incoming ion and material surface with least error.

Results

To benchmark our model, we compare the roughness exponent we calculated with least error value to the roughness exponent from experiments. We plot each error values versus the roughness exponent from 0.05 to 0.95 to find out the roughness exponent with least error. In Fig. IX.1, we can see that the error is low around the roughness exponent equals 0.45, which is close to the regime of H = 0.53 ± 0.03 given in [186] for 5 keV argon bombarded iron. We also benchmarked the 1 keV argon ions bombarded silicon with H = 0.23 [187]. From Fig. IX.2 we can see the roughness exponents given in [187] are also in good agreement with the low error regime.

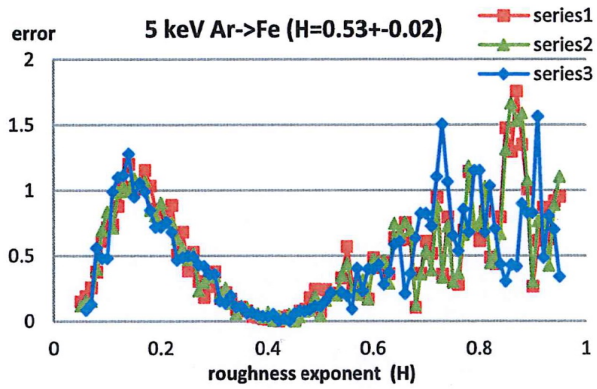

Figure IX.1. Roughness exponent test for 5 keV argon ions bombard on iron.

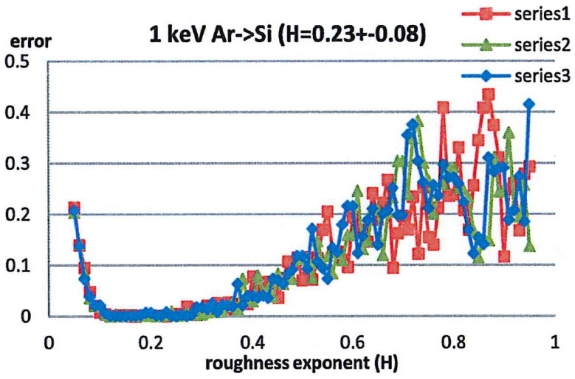

Figure IX.2. Roughness exponent test for 1 keV argon ions bombard on silicon.

Next we test the simulation result from [184]. In his VF-TRIM data for the self-sputtering of 1 keV Be, he used the fractal dimension equaled to 2.05, which means roughness exponent is 0.95. We used this value to construct the fractal surface and simulate the sputtering yield and compared to the experimental data. Fig. IX.3 shows that ITMC-F result is in good agreement with VF-TRIM compared with the experiment data. In our test of roughness exponent from 0.05 to 0.95, we found that the smallest error is in H = 0.95 regime, which is similar and in agreement with VF-TRIM setting.

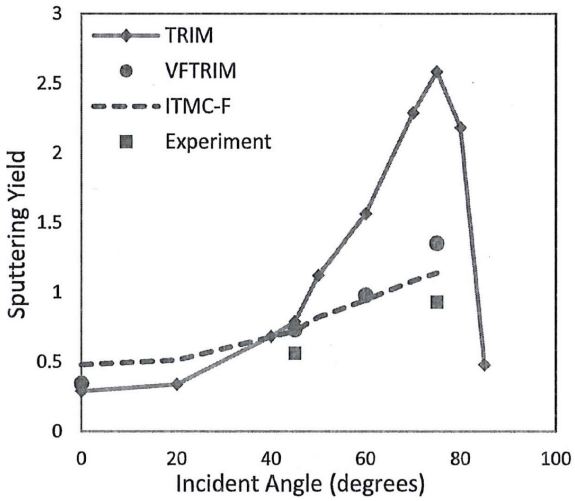

Figure IX.3. ITMC-F data for the self-sputtering of 1 keV Be as a function of incident angle with TRIM, VFTRIM and experimental data.

X. Modeling Hydrogen Isotope Behavior in Fusion Plasma-facing Components

Hydrogen diffusion driven by temperature and pressure gradients

We focused on understanding hydrogen isotope retention in plasma-facing materials in fusion devices [188]. Three common simulation methods are usually used to study this problem that includes Monte Carlo, molecular dynamics, and numerical/analytical methods. A system of partial differential equations describing deuterium behavior in tungsten under various conditions is solved numerically to explain recent data compared to other methods. The developed model of hydrogen retention in metals includes classic, intercrystalline and trapped-induced Gorsky effects. The bombardment and depth profile of 200 eV deuterium in single crystal tungsten are simulated and compared with recent work. The total deuterium retention at various temperatures and fluences are also calculated and compared with available data. The results are in reasonable agreement with data and therefore, this model can be used to estimate deuterium inventory and recovery in future fusion devices.

Model and methods

Hydrogen isotopes spatial distribution in metal can be generally divided into three regions: near-surface region (I), sub-surface region (II), and bulk (III). The near-surface region has higher concentration due to the incoming hydrogen being implanted and trapped in a few nanometers thickness layer. The sub-surface region shows the classic peak profile of atomic diffusion in metal lattice. In the bulk region, the concentration becomes more flat and slowly decaying and does not change much as hydrogen diffusion extends into the bulk. In order to explain such spatial profile and the ‘‘uphill diffusion’’ in region II, the classic Gorsky effect is utilized. The Gorsky effect is a diffusion relaxation process first predicted by W.S. Gorsky in 1935 [189], and is observed 30 years later in experiments by Schaumann and Alefeld [190] and Cantelli [191]. The Gorsky effect occurs when two conditions are fulfilled: First the point defects need to produce host lattice distortion and change the metal volume, which is true for almost every defect. Secondly, the defect mobility needs to be high enough in order to be observed [191]. Therefore, Gorsky effect is mostly seen in hydrogen-metal systems. For instance, if we bend a beamlike sample, the result would be a stress gradient in the sample and cause interstitial atoms to migrate from the compressive side to the stretching side.

A possible explanation of hydrogen concentration peak in region II could be that there is a stress field between region I and region II. This stress field ought to be generated from the host lattice distortion by implantation trapped hydrogen in near-surface. Thus, we proposed this stress field as trapped-induced Gorsky effect (TGE). TGE could result in an uphill diffusion that is similar to Gorsky effect. The difference is that Gorsky effect depends on external bending stresses while TGE depends on internal lattice distortion. With lattice distortion it would increase the stress and decrease trap sites between region I and region II.

Most of the traditional diffusion equations solved in this work are the general Fick diffusion equations and boundary conditions developed for the diffuse code described elsewhere [192] which is the first continuum code for hydrogen transport in wall established by M.I. Baskes. The diffuse code utilizes the diffusion equations for solving ion distribution in materials, with numerous conditions and examples such as those given by Wilson et al. [193]. However the pressure gradient is not considered in the common Fick's first and second laws which describe diffusion driven only by concentration gradient. We modified the diffusion equations and consider now the diffusion driven by temperature and pressure gradients.

Results

Deuterium retention at 200 eV in PCW at various temperatures

Simulation result is compared with experimental data using 200 eV deuterium incidents on polycrystalline tungsten (PCW) from Alimov and Roth [194] and Ogorodnikova et al. [195], and also compared to modeling result by Ning et al. [196]. Used parameters are 200 eV deuterium ions with flux ~$4x10^{19}$ m^{-2} s^{-1} and fluence 10^{24} D m^{-2}. From Fig. X.1 we can see that our result is in good agreement with other research. Alimov's result is lower compared to others because they again used NRA method and only count the retention from surface up to 7 μm, thus the difference becomes larger as temperature increases.

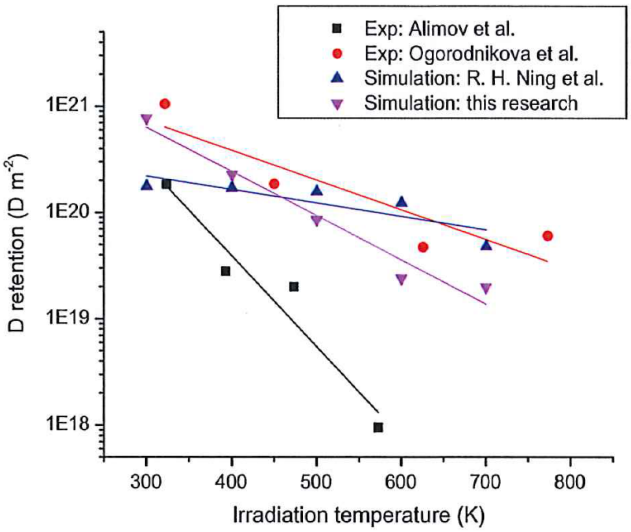

Figure X.1. Deuterium retention in polycrystalline tungsten at various temperatures

Deuterium retention at 200 eV in tungsten with various fluences

We modeled the single crystal tungsten (SCW) exposed to 200 eV deuterium ions with flux (10^{19} m^{-2} s^{-1}) to various fluences (10^{21}/10^{25} D m^{-2}) at 300 K. All results are compared with the experimental data from Alimov and Roth [197], Ogorodnikova et al. [195], Golubeva et al. [198, 199] and Ning et al. [198]. The details of these experiments are slightly different in the tungsten types used, measurement methods, and temperature. In Fig. X.2 we see that all the results are in a band region. Since the conditions are not

exactly same for all presented work, it is hard to make a detailed conclusion. Alimov et al. use NRA to measure deuterium concentration and calculate the retentions amount from surface up to 7 μm, while TDS does not have a depth restriction. In the meantime, our model sums up all the deuterium in tungsten for up to 200 μm, so the amount is slightly larger than other results.

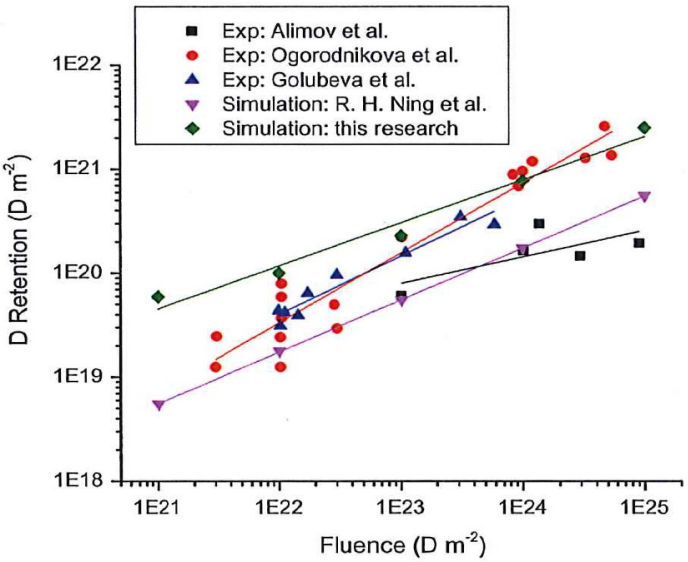

Figure X.2. Deuterium retention in tungsten with various fluences

Hydrogen diffusion on tungsten reconstructed (0 0 1) surface

A kinetic Monte Carlo (KMC) algorithm has been developed to study the hydrogen diffusion on tungsten reconstructed (0 0 1) surface in the temperature range 220–300 K [200]. The hydrogen diffusion coefficients predicted by the developed KMC code match the experimental values very well at low hydrogen coverage of a fraction of monolayer. A diffusion coefficient formula as a function of temperature and hydrogen coverage was derived from KMC simulations. Due to the very low probability of hydrogen occupying the long bridge adsorption sites, the rates of hydrogen atom having 3 or 4 neighbors are found to be zero for hydrogen coverage much less than a monolayer, while the rates of hydrogen atom having 0–2 neighbors are linear with respect to the hydrogen coverage. The calculated average rates of hydrogen located at the long bridge (LB) sites are very close to zero for low hydrogen coverage. Hydrogen only starts to occupy the LB sites after almost all short bridge (SB) sites are occupied.

Model and methods

To simplify the geometry and model, the lattice shown in Fig. X.3 is rotated 45◦counterclockwise, and the XY coordinate axes are reestablished. Fig. X.4 illustrates the simplified KMC diffusion model. The side length of the square lattice is $a/\sqrt{2}$, where a is the tungsten lattice constant (3.165˚A). In Fig. X.4, the odd rows are defined as LB sites, while the even rows are defined as the SB sites. The hydrogen could travel along the same bridge, or jump between adjacent bridges. There are four possible diffusion paths as indicated by the arrows in Fig. X.4. To describe the effects of temperature and neighbor interactions among hydrogen atoms, the transition state theory (TST) is applied to the model.

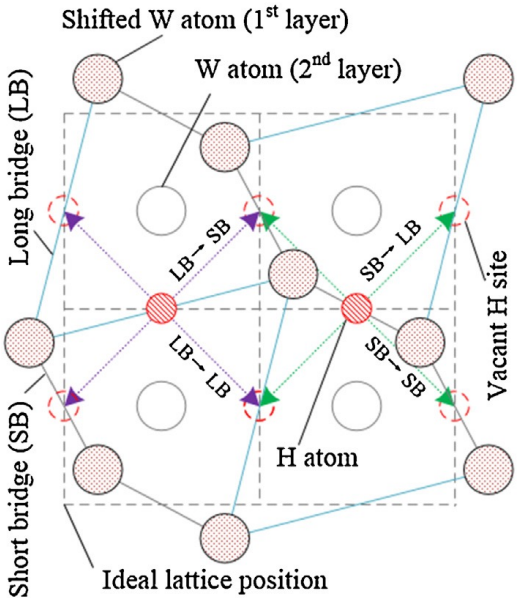

Figure X.3. Top view of W (0 0 1) reconstructed surface with hydrogen atoms (small circles) at the short bridge and the long bridge adsorption sites. First layer tungsten atoms (large circles with red dots) are shifted to {1 1 0} direction.

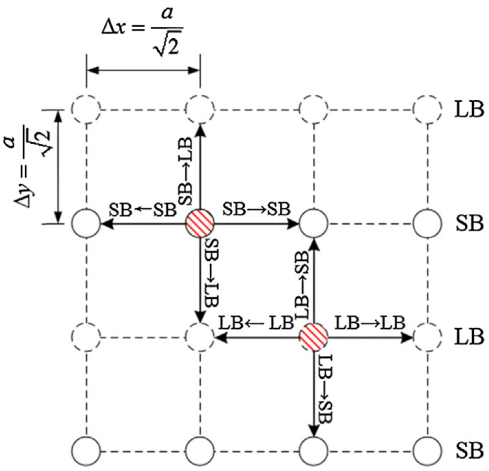

Figure X.4. KMC model for hydrogen diffusion on tungsten reconstructed (0 0 1) surface simulation. a: ideal tungsten lattice constant. Odd row: long bridge; even row: short bridge. Red circles: occupied hydrogen adsorption sites; hollow circles: vacant hydrogen adsorption sites.

Results

The activation energy (energy barrier) in TST formulas is the input of the KMC method, while the activation energy in Arrhenius equation is the calculation result obtained from the linear regression of the calculated diffusion coefficients. The activation energy remains unchanged for different H coverage, which meets the expectation, because the energy barrier used in the model remains the same. The H coverage only affects the pre-exponential factor D_0. Experimental fitted D_0 and E_a at the coverage of 0.08 ML are available for comparison, and they are plotted in Fig. X.5. Very good agreement between KMC and experiment results can be seen, indicating the developed model and code are both correct.

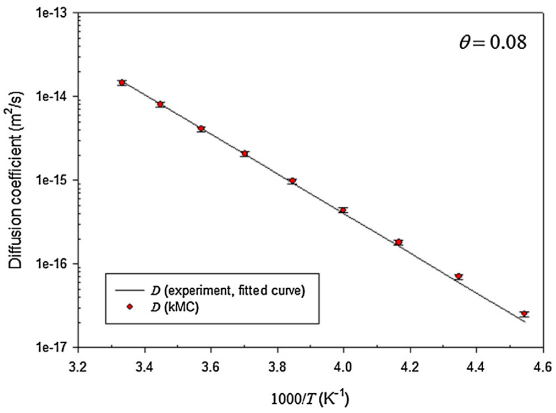

Figure X.5. Comparison of diffusion coefficients between KMC simulation and experimental results (fitted to Arrhenius' equation) at the coverage of 0.08 ML

XI. Atomic Scale Calculations of Tungsten Surface Binding Energy and Beryllium-induced Tungsten Sputtering

Tungsten surface binding energy was calculated using classical molecular dynamic simulations with three many-body potentials [201]. We presented the consistency in tungsten sputtering yield by beryllium bombardment between molecular dynamic LAMMPS code and binary collision approximation ITMC code using the new surface binding energy (11.75 eV). The commonly used heat of sublimation value (8.68 eV) could lead to overestimated sputtering yield results. The analysis of the sputtered tungsten angular distributions show that molecular dynamic accurately reproduced the [1 1 1] most prominent preferential ejection directions in bcc tungsten, while the distinct shapes by typical MC codes such as ITMC code is caused by the treatment of amorphous target. The ITMC calculated emitted tungsten energy profile matches the Thompson energy spectrum, while the molecular dynamic results generally follow the Falcone energy spectrum.

Results

The MD calculated tungsten SBE using EAM, EAM-FS, and Tersoff potentials are 11.56, 12.00, and 11.69 eV, respectively. The remaining energies of the ejected W atoms of all cases are lower than 0.01 eV. The ejected W atoms are tracked till the vertical distance between the ejected atom and the surface is much greater than the potential cut-off distance, to ensure that those atoms will not return back. The calculated SBE from three potentials are close to each other, and the average value of 11.75 eV is considered as the W SBE, which will be used in the subsequent BCA simulations. It is 35.4% greater than the tungsten heat of sublimation energy (8.68 eV), i.e., falling in the range of 30–40% mentioned earlier. Fig. XI.1 displays the Be-induced tungsten sputtering yield calculated by ITMC with default and new SBE and LAMMPS with three many-body potentials. In this region of incident energies, the sputtering yield can be treated as linear with incident energy. The fitted linear curves are drawn in Fig. XI.1 as well and they are extended to the axis. All three MD potentials yield similar results. Sputtering yield by ITMC with default SBE is overestimated, about two times greater than the MD results. Using the MD predicted tungsten SBE, the ITMC code produces identical sputtering yield as MD method. This consistency indicates correct SBE calculation procedure and value. The extensions of the sputtering yield curves show that the threshold for Be → W physical sputtering is around 60 eV.

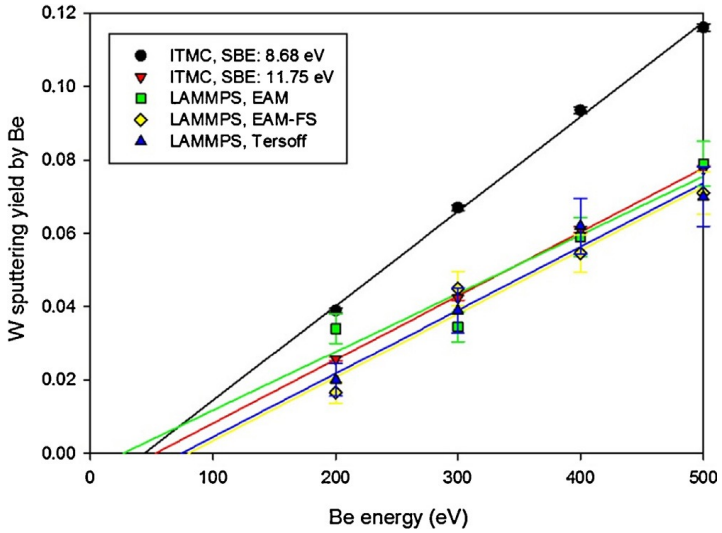

Figure XI.1. Tungsten sputtering yield by beryllium bombardment calculated by ITMC with default and new SBE and LAMMPS with three many-body potentials.

XII. Particle-in-cell Methods in Predicting Materials Behavior during High Power Deposition

HEIGHTS-PIC package has been developed to solve a multi-dimensional plasma evolution after an intense energy deposition from plasma instabilities impinged on the PFC [202-204]. The purpose of such package is to develop another path for the solution of the integrated and complicated physical models involved using the PIC technique and to additionally benchmark HEIGHTS package. Detailed physical models of plasma - solid-liquid-vapor interactions with the presence of a strong inclined magnetic field have been developed in a self-consistent model coupled with radiation MHD models. Plasma ELM/disruption modeling is presented and explained in detail as well as the new approach proposed into the PIC technique. Results for ELM and disruptions reproducing the MK200 plasma gun experiments are presented and discussed with special attention onto the advantages and flexibility of this new PIC approach regarding choice of the computational mesh and computational time versus aimed results accuracy.

Simulation results and benchmarking

The PIC model of the off normal event effect on the divertor/target plate using a MK200-like geometry and ITER-like geometry confirmed similar analysis about the erosion depth, profile, and plasma behavior [18, 21, 22, 205-207]. In evaluating the conditions present in the MK-200 UG facility, particular attention has been given to interpret numerically both the beam shape and its working characteristics along time. Several evolutions of the beam along time have been tested and here a 10 μs linear rise is presented. It is assumed for the simulations run with HEIGHTS-PIC that the beam has a Gaussian shape power density profile with full width half maximum of 7.0 cm. The peak of the power density is equal to 35 MW/cm^2 and the total working time for the plasma gun is set at 50 μs as in the facility in Troisk [205-207]. The mock-up geometry is shown in Figure XII.1.

The peak power density is reached after 10 μs for the linear rise and immediately for the step rise remaining constant for the next 35 μs. The last part of the time evolution has an exponential decay until the end of the simulation. In the simulations results here reported, the beam is considered perpendicular to the target as well as the magnetic field having an intensity of 2 T [208]. The total energy provided in such a way is roughly 52 kJ which is close to the one provided by the real machine for such conditions. In our simulations, the target is assumed to be at an initial temperature of 0.36 eV in order to speed up the calculation. The neutral vapor close to the target is instead assumed to have a low initial density (i.e., 10^{14}/cm^3). The initial diffusion coefficient is taken to equal to $D_\perp = 15 m^2/s$ [209]. The target plane has a measure of 10 by 10 cm while the perpendicular projected plane where the evolution of plasma vapor cloud will be followed is 10 cm (as the target) by 15 cm.

Several simulations have been run using both different initial sample particle loadings and computational mesh. Being the solution of the radiation transport equation the longest in terms of computational time (93 to 95% of the total time), it is important to establish in function of the aimed accuracy of the result, the trade-off point between number of sample particles initially loaded and coarseness of the computational mesh used. The interplay of the three very complex phenomena (impact of plasma on the surface with formation of a vapor cloud, radiation from the vapor cloud, and heat conduction into the divertor plate) exerts different roles according to the impact duration of disruption or off-normal event. The prediction of the final erosion onto the target plate as well as the amount of material (carbon in this case) released into the Tokamak and able to reach eventually the bulk plasma is very important. Figure XII.2 shows the final plate surface erosion profile obtained with the above mentioned data and with different computational grids used in simulations.

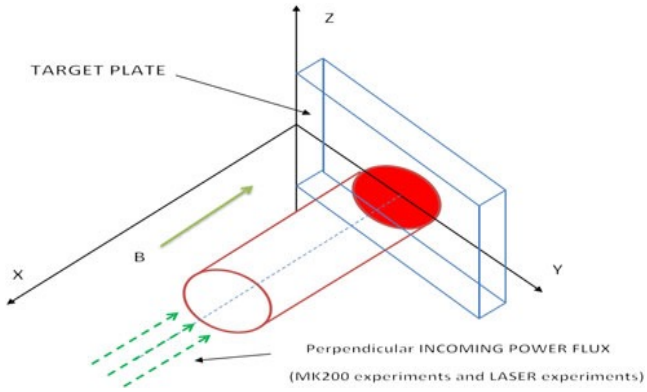

Figure XII.1. Basic geometrical scheme used in HEIGHTS-PIC benchmarking with MK200 experiments.

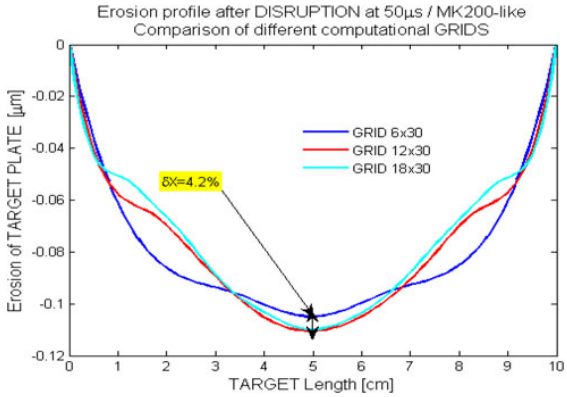

Figure XII.2. Calculated geometrical erosion evolutions along the plate in MK200-like conditions simulations using HEIGHTS-PIC (6 × 30, 12 × 30, 18 × 30 grids).

The maximum erosion is in the same order of magnitude of the one experimentally determined with the MK200 experiments (= 0.1 μm over 15 shots) [205-207]. The crater looks approximately symmetrical as expected. Examining Figure XII.3, it is evident that initially most of the energy is spent in heating up and vaporizing the material. The erosion reaches quickly a plateau point, where then most of the vapor acts as a screen with respect to the target plate. As more energy is damped, more ionization takes place leading to a slow linear increase of the erosion itself due to the expansion of the plasma vapor cloud. The ionized particles in fact start moving along the magnetic field lines.

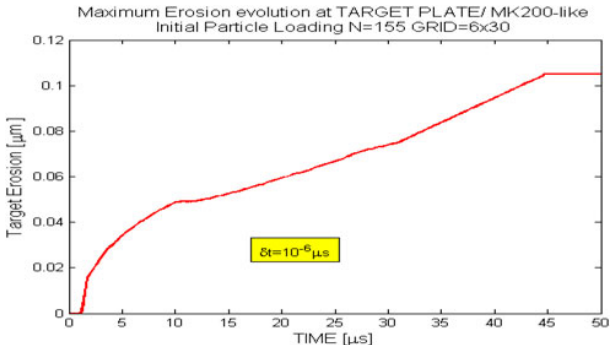

Figure XII.3. Plate erosion rate at plate center after full disruption impact in MK200-like conditions

In order to have more benchmarking comparisons, HEIGHTS-PIC has also been compared with the original HEIGHTS package for ELM conditions in Tokamaks [18]. Using ITER-like geometry, the evolution of an ELM event has been simulated for 100 μs. Carbon material divertor was assumed as target plate. The magnetic field intensity used is 5 T and the inclination of the field with respect to the target plate is 5°. The ELM impinging plasma has been simulated assuming an exponential beam shape with the maximum power density profile at the strike point. For the total duration, 12.6 MJ of energy (roughly 10% of the total pedestal energy) are supposed to reach the target plate. The e-fold length of the power profile above the plate is in such conditions of 6.7 cm. At the strike point the power density profile peaks at 4.6 MW/cm2 with a minimum at the e-fold length of 1.692 MW/cm2. The ITER major radius is of 6.5 m while the assumed initial plasma temperature is of E0= 3.5 keV. The computational domain taken into

account extends then for 6.7 cm along the target plate and for 15 cm perpendicular to it: 300 cells are used in the following ELM simulation making the cell dimensions of 0.67 cm for 0.5 cm. No poloidal magnetic field is assumed in HEIGHTS-PIC simulations.

Erosion of the divertor plate is highly influenced by the beam intensity, duration, and geometrical distribution above the target. Recent studies have pointed out that the plasma energy flux reaching the target plate through the scrape off layer has a non-symmetrical shape similar to an exponential decay. The time considered for a typical ELM event (100 μs) is too small to allow significant heat transfer through the material, so that most of the energy released is spent for the carbon erosion and its hydrodynamics movement in the plasma-vapor cloud above the surface.

As expected, the maximum final erosion depth for the longer pulse is larger when compared to the shorter ELM (Fig. XII.4). Though for the areas of the target plate further from the striking point erosion is consistently less due to much less power flux effectively reaching the plate (Fig. XII.5). It is interesting to note also that the shift in position of the maximum depth is absent in HEIGHTS-PIC simulation because no poloidal field is present in the actual model and the diffusion across the magnetic field is not so pronounced to provoke erosion where the plate is not directly reached by the impinging beam. The trend compared with HEIGHTS is in good agreement in shape, magnitude and time evolution.

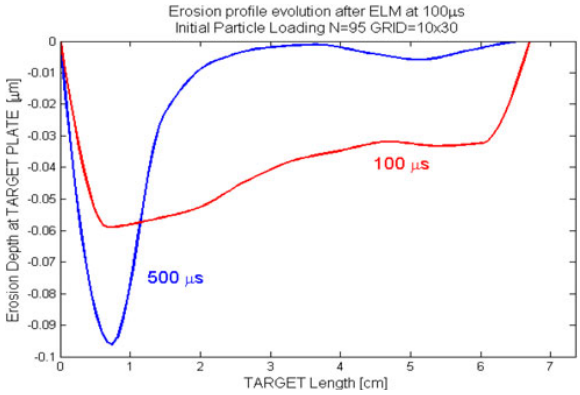

Figure XII.4. HEIGHTS-PIC calculated erosion for different ELM pulses.

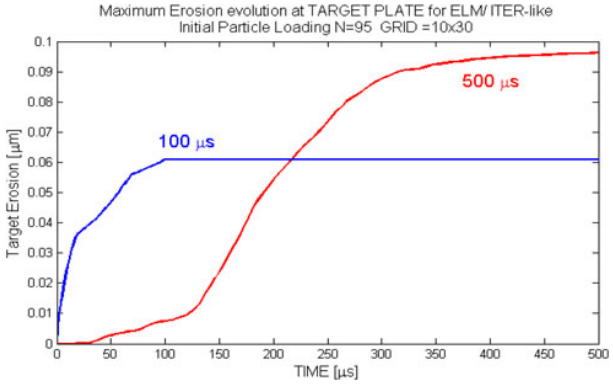

Figure XII.5. HEIGHTS-PIC calculated erosion evolution for different ELM pulses.

XIII. Analysis of Materials Using Lasers – Plasma Shielding and Radiation Effects

Plasma shielding effect is well known mechanism in laser-produced plasmas (LPP) reducing laser photons transmission to the target and, as a result, significantly reducing target heating and erosion. Shielding effect is less pronounced at low laser intensities, when low evaporation rate together with vapor/plasma expansion processes prevent establishment of dense plasma layer above the surface. Plasma shielding also losses its effectiveness at high laser intensities when the formed hot dense plasma plume causes extensive target erosion due to the radiation fluxes back to the surface. The magnitude of emitted radiation fluxes from such plasma is similar or slightly higher than laser photon flux at the low shielding regime. Thus, shielding efficiency in LPP has a peak that depends on laser beam parameters and target material. Similar tendency is also expected in other plasma operating devices such as tokamaks of MFE reactors during transient plasma operation and disruptions on chamber walls when deposition of the high energy transient plasma can cause severe erosion and damage to plasma facing and nearby components. Detailed analysis of these abnormal events and their consequences in future power reactors is limited in current tokamak reactors. Predictions for high power future tokamaks are possible only through

comprehensive, time-consuming, and rigorous modeling. We developed scaling mechanisms, based on modeling of LPP devices with their typical temporal and spatial scales, to simulate tokamak abnormal operating regimes to study walls erosion, plasma shielding, and radiation in MFE reactor conditions. We found analogy in regimes and results of carbon and tungsten erosion of the divertor surface in ITER-like reactors with erosion due to laser irradiation. Such approach will allow utilizing validated modeling combined with well-designed and well-diagnosed LPP experimental studies for predicting consequences of plasma instabilities in complex fusion environment, which are of serious concern for successful energy production.

Our HEIGHTS package is designed for detailed simulation of LPPs. The HEIGHTS package includes models for three-dimensional description of energy deposition, vapor/plasma shielding cloud formation/evolution and MHD processes, thermal conduction in material and in plasma, atomic physics processes and resulting opacities, detailed photon radiation transport, and the interaction between plasma/radiation and target material. We extensively benchmarked and utilized the package in modeling and optimization of LPP sources for extreme ultraviolet (EUV) lithography, the current leading method for the manufacturing of the next generation computer chips [210, 211]. We considered several lasers, materials, and target configurations to develop efficient sources for EUV photons production. In the processes of optimization, shielding effect of plasma produced from small liquid tin droplets (leading target material for EUV production) and resulting EUV source performance were investigated in great details [211]. For example, we studied the effect of various laser parameters and wavelengths on the conversion efficiency (EUV photon yield vs. incident laser energy) of such devices and found that CO_2 lasers having longer wavelength, regardless of pulse intensity have several advantages over Nd:YAG lasers. Shielding effect also explained the higher conversion efficiency of dual-beam LPP sources when Nd:YAG laser with shorter wavelength was used for pre-plasma production followed by CO_2 laser heating this optically thin pre-plasma for efficient EUV photons generation.

In this work we studied the shielding effect in LPPs of carbon and tungsten targets. These materials are considered as the main coating materials of PFCs in tokamaks in the areas where intense heat fluxes from the disruptive plasma are expected. In spite of the differences in time scales, energy source, and intensities of transient events between MFE reactors and nanosecond laser devices we found analogy in plasma evolution, conversion of source energy to radiation, and shielding efficiency among these systems. Taking into account the relative simplicity and well-controlled laser devices for accurate modeling and precise measurements compared to the complex fusion reactors, such approach can be used for the investigation of various materials and compounds in regard to the erosion dynamics, shielding efficiency, components lifetime, radiation to nearby components, and potential chamber contamination issues in a much cheaper and significantly faster way.

Vapor shielding effects

Modeling results of plasma instabilities during ELMs and disruptions, with anticipated ITER parameters, showed that the initial layer of evaporated carbon from the divertor surface can reduce plasma heat flux to the surface by more than 20 times protecting, thereby, the divertor surface from further high erosion and damage [18, 24]. For ITER disruption scenarios, with 126 MJ total impact energy (100% pedestal energy) on the carbon divertor plate, the maximum unshielded energy density of 5 kJ/cm^2 could result in the evaporation of ~ 200 μm of carbon layer at the strike point. However, the vapor layer formed above the strike point during the first 5-10 μs of disruption leads to absorption and redistribution of core plasma energy and significant protection of surface from further erosion that results in reducing erosion depth in ~ 1000 times in comparison with unshielded scenarios.

Figure XIII.1 shows schematic description of ITER-like divertor area and illustrates plasma particles transport to the divertor surface during plasma instability events such as ELMs and disruptions. This configuration was used in our modeling analysis of divertor surface response to these events [29].

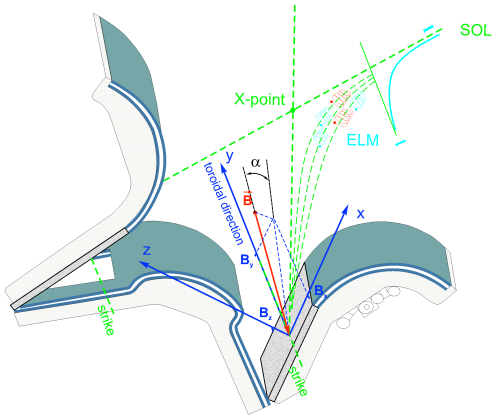

Figure XIII.1. Schematic illustration of ITER-like divertor design and coordinate systems used in HEIGHTS modeling [29]. Angle α corresponds to the poloidal angle of magnetic field lines at the divertor surface in tokamak reactors.

Analysis of vapor/plasma characteristics in the developed plume from the divertor eroded carbon showed that plume with plasma density of order of 10^{18} cm^{-3} and thickness of 1-2 cm can be formed during the first 10 μs as shown in figure XIII.2. Based on cross-sections for interactions of D/T/electrons with such vapor/plasma plume we estimated that the incident 3.5 keV D/T ions will totally lose their energy in 0.2-0.3 cm layer and the intensity of the incident core plasma electrons will also significantly slowdown in their way through the developed plasma. Figure XIII.3 shows absorption of disrupting plasma energy in the developed plume above the divertor surface that resulted in reducing heat intensity to the divertor strike area and protection of surface at this location.

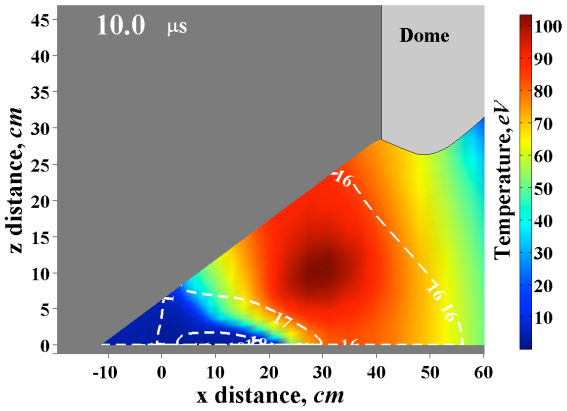

Figure XIII.2. Electron temperature and density (white contours) distribution in vapor/plasma plume developed from eroded carbon during the first 10 μs of disruption.

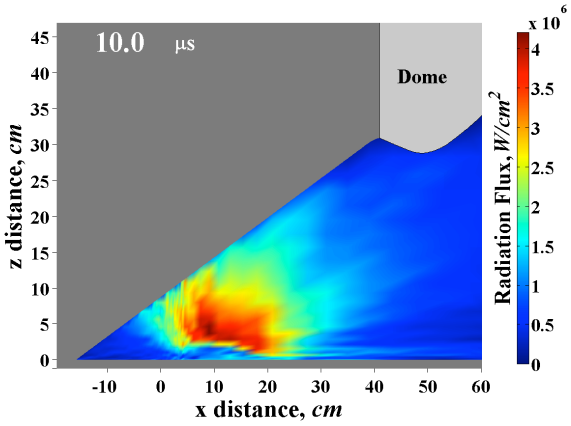

Figure XIII.3. Core plasma energy and electron density (white contours) distribution in vapor/plasma plume developed from eroded carbon during the first 10 μs of disruption.

The early development of a protective layer during very short time was possible due to the high evaporation rate of carbon surface caused by the initial intense heat flux of 50 MW/cm^2 and high velocity of the developed hot plume. Plume with velocity of 1-10 km/s can expand up to 0.1-1 cm during 1μs as shown in figure XIII.4.

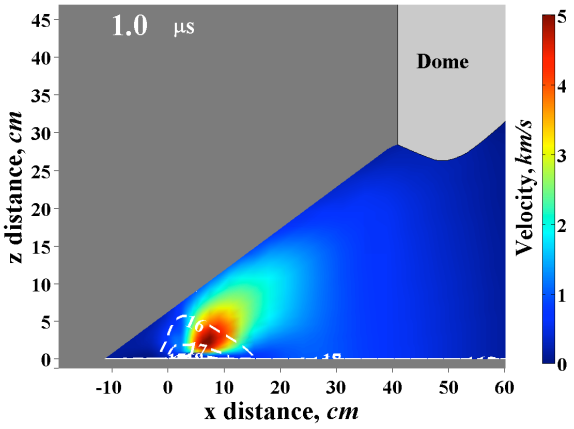

Figure XIII.4. Electron density (white contours) distribution and velocity in vapor/plasma plume developed from eroded carbon during first 1 μs of disruption.

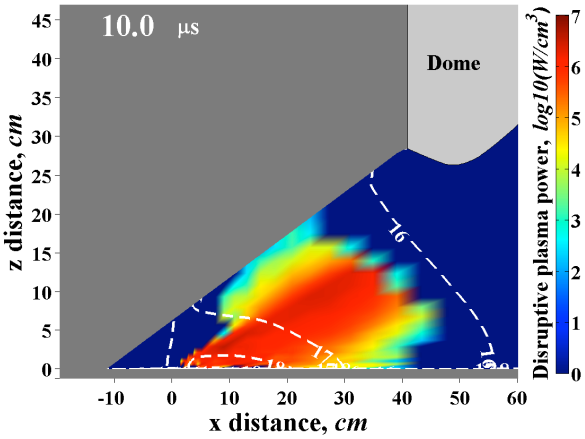

Figure XIII.5. Radiation fluxes in plasma developed from eroded carbon.

However, such hot plasma with temperatures up to 120 eV (still much lower than the original disrupting plasma temperature) caused extensive erosion of surfaces surrounding the strike point. Radiation fluxes from carbon plasma with intensity of the order of 10^6 W/cm^2 to the divertor during a disruption time of 100 μs were the main reason of the erosion along 40 cm of divertor surface [18]. Radiation energy density to surfaces of nearby components was even higher. Such potential damage of nearby components has to be evaluated very carefully when choosing plasma facing and nearby materials as well as diveror design and configuration in future power rectors [65]. Figure XIII.5 shows radiation fluxes in carbon plasma as well as illustrates surfaces in the divertor area subjected to plasma radiation with such high intensities.

The above example showed the importance of thorough analysis of materials as candidates for the divertor surface coating to predict erosion of these materials during plasma instabilities as well as to predict potential damage resulting from the secondary plasma developed from the eroded material. Estimation of vapor/plasma shielding efficiency and magnitude of plasma radiation fluxes can be predicted through detailed analysis of materials behavior using simple and well-diagnosed LPP devices.

Prediction of similar conditions in laser-produced plasma (LPP)

Based on the main characteristics of disruption energy load used in our analysis for ITER-like conditions such as maximum unshielded energy density of 5 kJ/cm^2 deposited during 100 μs we estimated the initial parameters of a laser beam needed to simulate carbon erosion and shielding efficiency in LPP devices. Taking into account typical Nd:YAG laser pulse duration of 10 ns, that is 4 orders of magnitude lower than a tokamak plasma disruption duration, we predicted 5×10^{11} W/cm^2 for the laser beam intensity.

The spot size is another important parameter of laser beam that can influence target erosion and developed plasma characteristics. Figures XIII.6a) and b) show difference in plasma temperature and mass density distribution in plasma created by lasers with 100 μm and 300 μm spot sizes, respectively using the above laser beam intensity and duration. In both cases craters with the same depth of around 1 μm were created as shown in figures XIII.7a) and b).

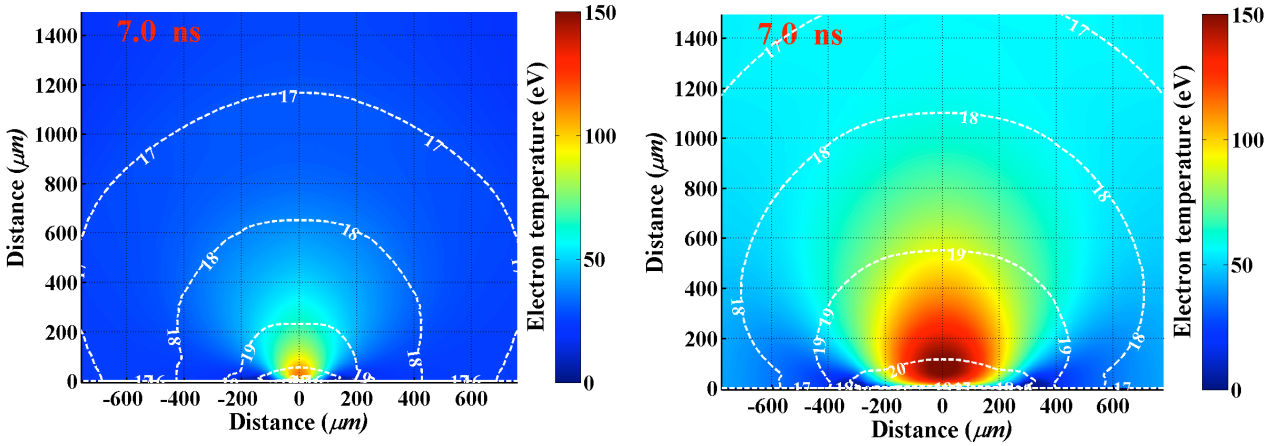

Figure XIII.6. Electron temperature and density (white contours) distribution in vapor/plasma plume developed from carbon target by Nd:YAG laser with a) 100 μm and b) 300 μm spot sizes.

The main difference is in the larger volume of material eroded by laser with the larger spot size that resulted in higher plasma density in the plume. Higher absorption of laser photons as well as slower processes of plasma cooling by radiation transport and by energy dissipation due to thermal conduction in such dense plasma explain the higher temperatures shown in figure XIII.6b).

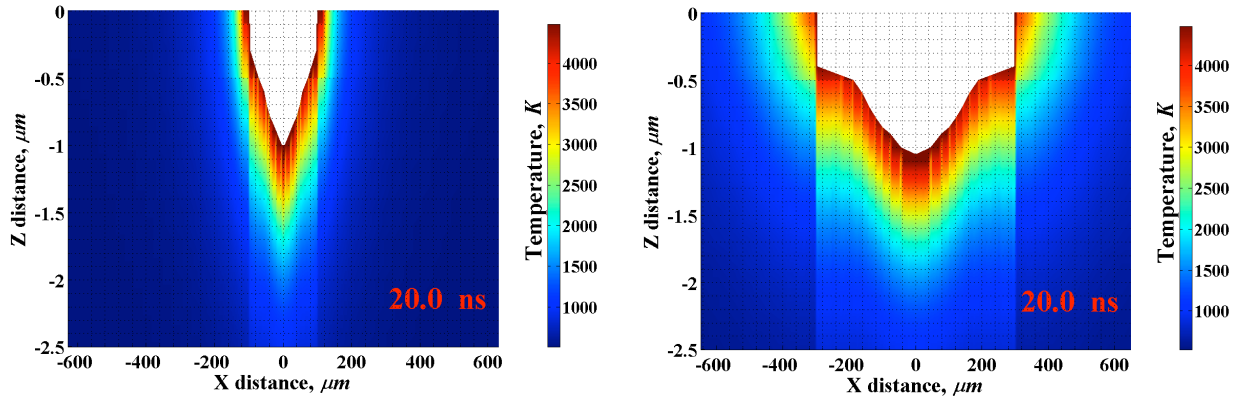

a) b)

Figure XIII.7. Carbon erosion by Nd:YAG laser with a) 100 μm and b) 300 μm spot and $5x10^{11}$ W/cm^2 intensity.

The optically thick plasma plume developed during laser irradiation protected the target surface from laser photons that significantly decreased target erosion. However, high intensity of radiation fluxes from the hot and dense plasma reduced the shielding efficiency for the considered laser intensity. Plasma radiation was the main energy source that caused the extensive evaporation and determined the spatial temperature profiles in target. Figures XIII.8a) and b) show the shielding efficiency of plasma plumes in both cases demonstrating almost total protection of the target from the incident laser irradiation at the center of laser spot, however, predicting high energy density of plasma irradiation to the target at this location. The combined effect of low shielding from laser photons and radiation fluxes from peripheral

plasma regions is the reason of intensive evaporation of the target at the borders of laser spot area that is more evident in the case of larger spot size (figure XIII.7b)).

Figures XIII.8a) and b) clearly demonstrate the processes developed above the surface during laser interaction with target and with evolving plasma. Heating and evaporation of the target, flow of vapor/plasma from the crater, and, at the same time, compression of plasma plume at the laser spot center resulted in variation of plasma layer thickness above the surface during laser irradiation that influenced surface protection and shielding efficiency. Due to the large difference in energy transfer to the target in the spot area and outside as well as due to low thermal conductivity in carbon, sharp boundaries in temperature profiles are seen in figure XIII.7b). The difference in the shown spatial dimensions, i.e., several hundreds of micrometers along surface and up to 2 μm in depth, increases visual evidence of such boundaries.

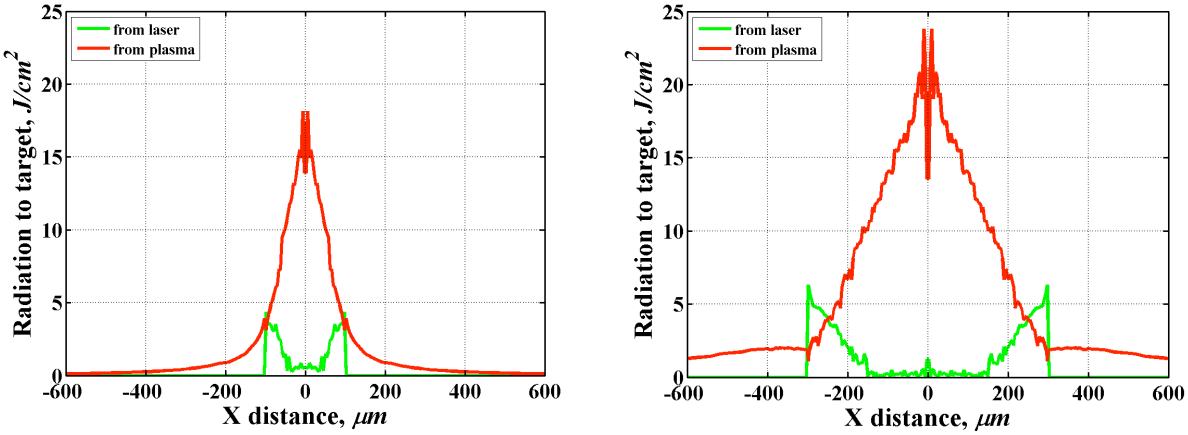

a) b)

Figure XIII.8. Energy density to the target from laser and from developed plasma for a) 100 μm and b) 300 μm spot sizes of Nd:YAG laser beams.

In spite of similar temperatures range in the plasma developed during disruption in fusion reactor environment and in LPP devices using Nd:YAG laser, denser plasma plume created by this laser resulted in almost four orders of magnitude larger radiation fluxes from such a plasma to the target. Taking into account the difference in time scale between the considered events, total energy density from plasma radiation to the target at the center of beam spot can be the same as at the location of the maximum unshielded energy density on the divertor surface [18]. Since plasma irradiation was the main source of target erosion in both cases, similarity in shielding and erosion mechanisms in MFE and LPP devices is evident. Thus, one can find analogy in the processes of target erosion from the two different initial energy sources such as core plasma particles in MFE and laser photons in LPP devices and by the secondary, created source – radiation fluxes from the developed plasma of the eroded material.

To further track the dependence of the shielding efficiency on energy density in different devices we simulated carbon ablation by laser beam with 10 times lower intensity that, based on our scaling mechanism, can correspond to a Giant ELM energy load during 100 μs in ITER-like devices [24]. Figures XIII.9 and XIII.10 show that developed secondary vapor plasma also had the same temperatures range in both MFE and LPP environments. Similar to the more intensive disruptive regimes described above, radiation fluxes to the target were also approximately four orders of magnitude higher in LPP device due to denser plasma developed.

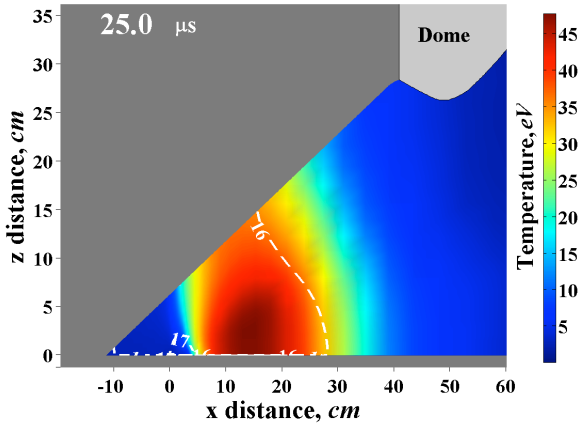

Figure XIII.9. Electron temperature and density (white contours) distribution in vapor/plasma plume developed from eroded carbon during first 25 μs of Giant ELM with 100 μs duration.

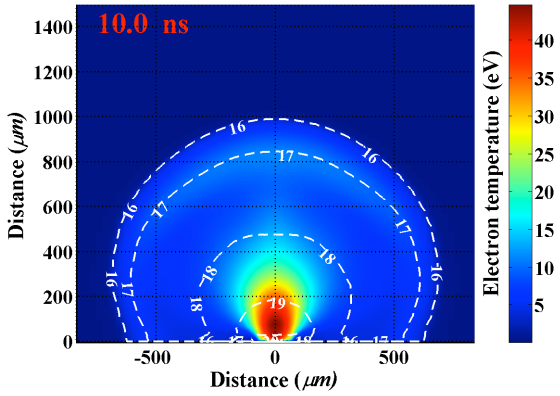

Figure XIII.10. Electron temperature and density (white contours) distribution in vapor/plasma plume developed from carbon target by Nd:YAG laser with 100 μm spot and $5x10^{10}$ W/cm^2 intensity.

Because of this lower intensity of energy sources in both LPP and MFE cases, therefore lower evaporation rate, less dense, and colder plasma was created. Hence, the shielding efficiency from the main source particles was significantly reduced in comparison with the previous higher intensity regimes. Erosion of target in this case was mainly due to ions and electrons in MFE device [18] and by laser photons in LPP rather than radiation fluxes from the developed shielding layer. Crater depths on the divertor surface as well as on carbon plate in LPP device were approximately two times lower in this case for the 10 times lower intensities of these events. Relevant scaling can be easily developed and benchmarked using simple LPP experiments and simulation.

Vapor/plasma shielding in LPP for Fusion environment

We studied the effect of vapor shielding and plasma radiation on target ablation for two materials, i.e., low-Z carbon and high-Z tungsten, varying several laser beam parameters. The pulse intensity of the laser beam for the given wavelength is one of the main parameters in determining plasma temperatures and densities distribution. Other parameters such as pulse duration, shape, and spot size, also affect the values range and combination of these characteristics. However, the tendency in target ablation shape and the main energy source responsible for the ablation, i.e., laser photons or plume plasma photons are determined by laser intensity.

Initially we found the lowest reasonable intensity of laser beam for tungsten erosion based on estimation of the lowest energy density required for vaporization of significant amount of material to get tangible plasma layer with temperatures around 1 eV and higher. From tungsten thermodynamic properties, about 1 J/cm^2 is required for the heating of material up to boiling point and for further vaporization of about 100 nm layer. Taking into account reflectivity of Nd:YAG laser with 1064 nm wavelength from W surface as well as energy distribution due to high thermal conductivity in this material even for nanosecond time duration, we estimated lowest energy density to be 3-4 J/cm^2. We started simulations utilizing 5 J/cm^2 with typical laser beam duration for Nd:YAG laser, such as 5 ns, that leads to 1 GW/cm^2 intensity. We obtained in modeling maximum ablation depth of ~100 nm. Our simulations showed that erosion of target was caused mainly by laser photons and only half of laser

energy at the spot center was transferred to the target that demonstrates shielding effect of tungsten vapor/plasma even at such low beam intensity.

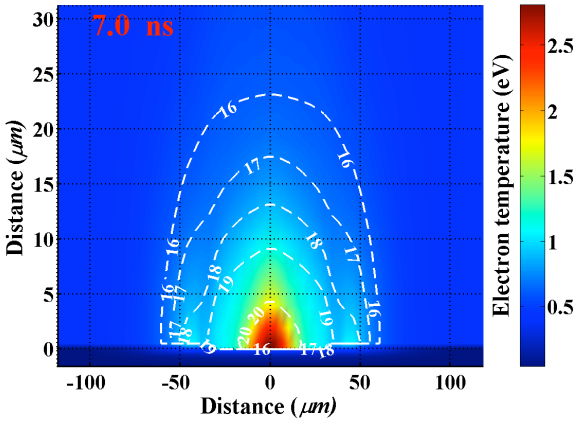

Figure XIII.11. Temperature and density (white contours) distribution in plasma plume developed from W target by Nd:YAG laser with 100 μm spot and $1x10^9$ W/cm^2 intensity.

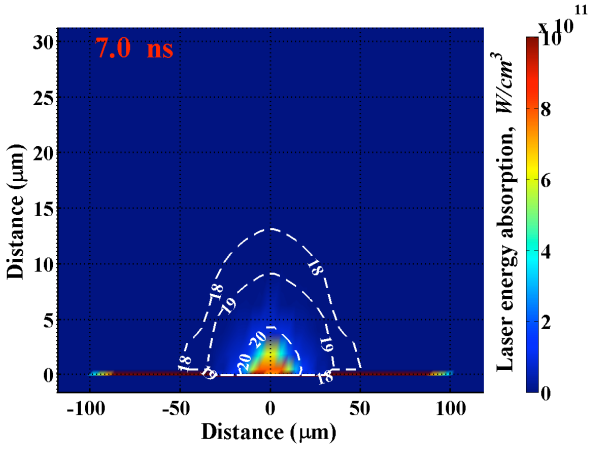

Figure XIII.12. Laser energy absorption in developed plasma.

Figures XIII.11 and XIII.12 demonstrate the processes of plasma evolution at the end of laser pulse and the corresponding location of preferential laser energy absorption in the developed plume. These results for plasma evolution in W at low laser intensity are consistent with results for energy density threshold for laser induced plasma formation in tungsten obtained in experiments.

Based on the above benchmarking of the start point for modeling of tungsten ablation by laser beam we extended the range of considered intensities up to 10^{12} W/cm^2 as shown in figures XIII.13 and XIII.14 for both tungsten and carbon targets.

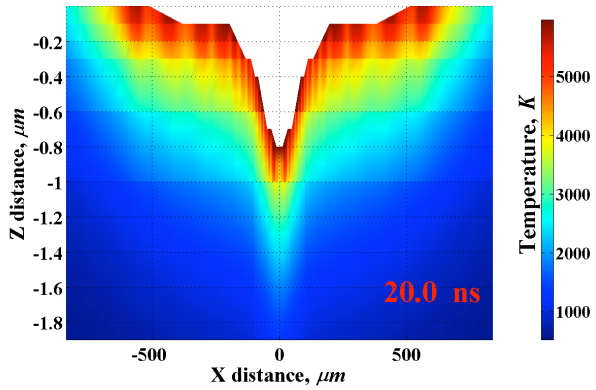

Figure XIII.13. Tungsten erosion by Nd:YAG laser with 100 μm spot, 10^{12} W/cm^2 intensity and 10 ns pulse.

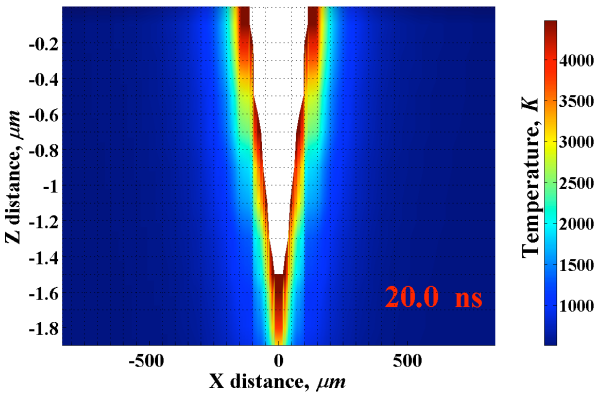

Figure XIII.14. Carbon erosion by Nd:YAG laser with 100 μm spot, 10^{12} W/cm^2 intensity and 10 ns pulse.

For higher laser intensities, the shape of the crater or the evaporated mass are the most important characteristics in analysis of target ablation and shielding effect, rather than crater depth as usually analyzed in experiments. For example, figures XIII.13 and XIII.14 show that laser with intensity of 10^{12} W/cm^2 creates almost two times deeper crater in carbon than in tungsten. However, width of crater in W

sample is several times larger and significantly exceeds the laser spot size. The intense radiation flux from the plasma developed from high-Z material is one of the reasons for that. Although the vaporized layer of high-Z material provides higher protection of the target from laser photons, however it generates 10 times higher radiation fluxes from the developed plasma, as shown in figures XIII.15 and XIII.16. Radiation fluxes that caused intense evaporation of target surface in original spot area had also large effects on nearby surfaces. This should be taking into account in analysis of materials and reactor design for MFE environment.

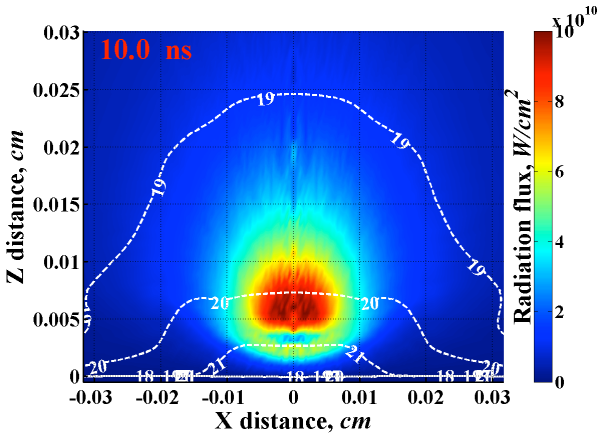

Figure XIII.15. Radiation fluxes and plasma density (white contours) in W plasma produced by Nd:YAG laser with 100 μm spot, 10^{12} W/cm^2 intensity and 10 ns pulse.

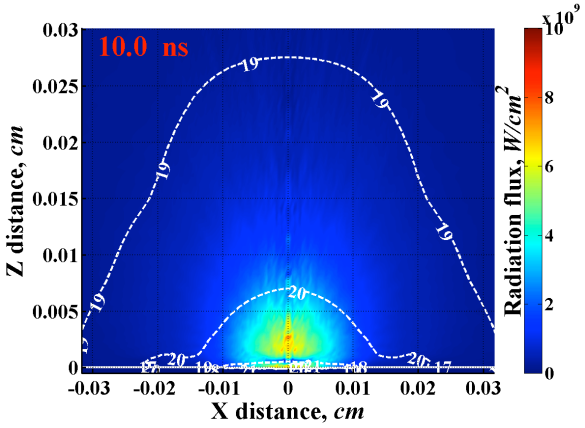

Figure XIII.16. Radiation fluxes and plasma density (white contours) in C plasma produced by Nd:YAG laser with 100 μm spot, 10^{12} W/cm^2 intensity and 10 ns pulse.

Figures XIII.17 and XIII.18 show the difference in shielding efficiency of tungsten and carbon plasmas at the crater center developed by Nd:YAG laser with the same beam parameters. The evaporated mass and maximum crater depth in carbon target did not change much (0.3-0.5 μm) up to 10^{11} W/cm^2 laser intensity that corresponds to approximately the same total energy load due to low shielding by carbon plasma and low irradiation from plasma (figure XIII.18). We should note that these results are consistent with experimental measurements of plasma parameters at 3 mm distance from carbon sample where almost steady-state temperature and density values were found in the range of laser intensities from 10^{10} W/cm^2 to 10^{11} W/cm^2 [212].

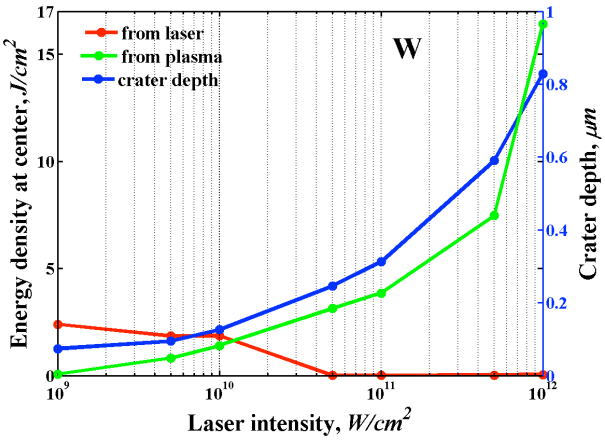

Figure XIII.17. Energy density from laser and from plasma at crater center of W target and related crater depth

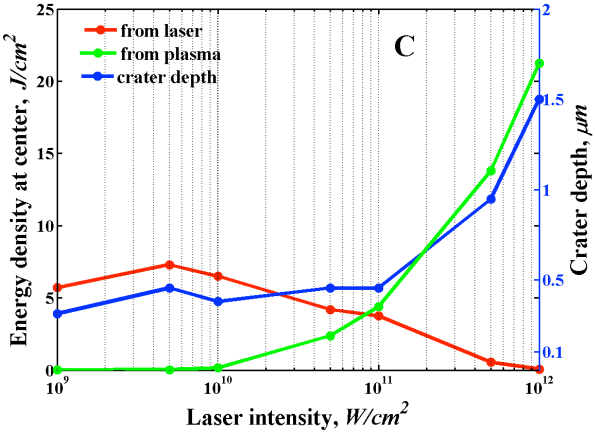

Figure XIII.18. Energy density from laser and from plasma at crater center of C target and related crater depth

Better protection of the surface at the spot center from laser irradiation as well as from hot plasma irradiation by denser tungsten vapor/plasma plume results in almost two times less erosion depth of developed crater (figure XIII.17). However, tungsten target received almost 10 times more of total energy at the higher laser beam intensities compared to carbon as shown in figures XIII.19 and XIII.20. Evaporation rate from tungsten was totally determined by the high radiation from plasma as shown in figure XIII.19.

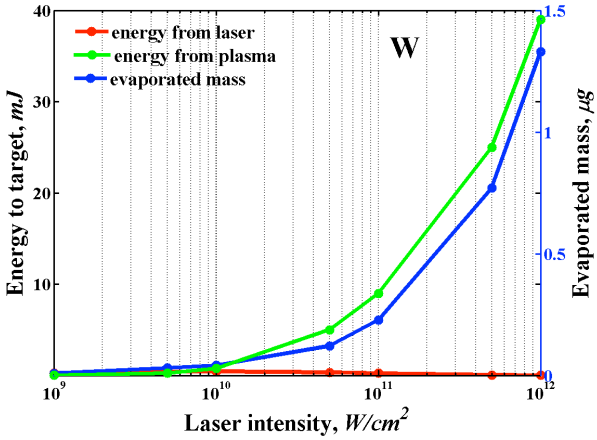

Figure XIII.19. Energy deposition on W target from incident laser radiation and from evolving plasma and the resulting evaporated mass.

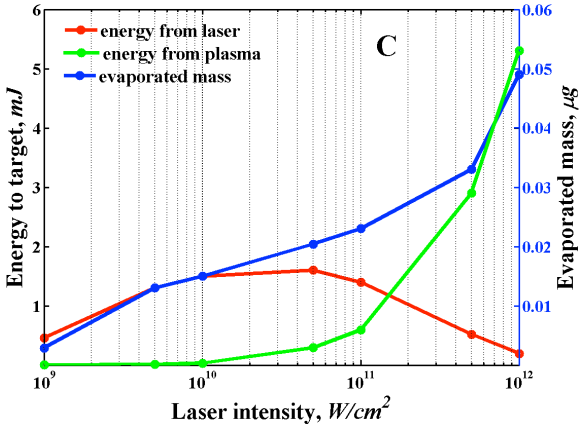

Figure XIII.20. Energy deposition on C target from incident laser radiation and from evolving plasma and the resulting evaporated mass.

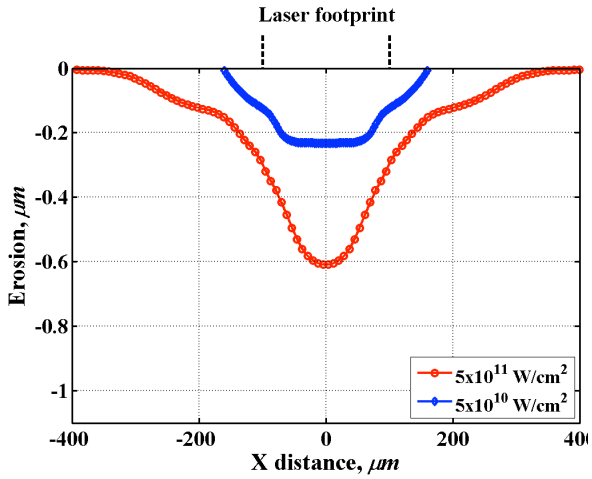

Figure XIII.21. Crater depth and shape in W target created by Nd:YAG laser with 100 μm spot, 10 ns pulse, and $5x10^{10}$ and $5x10^{11}$ W/cm^2 intensities.

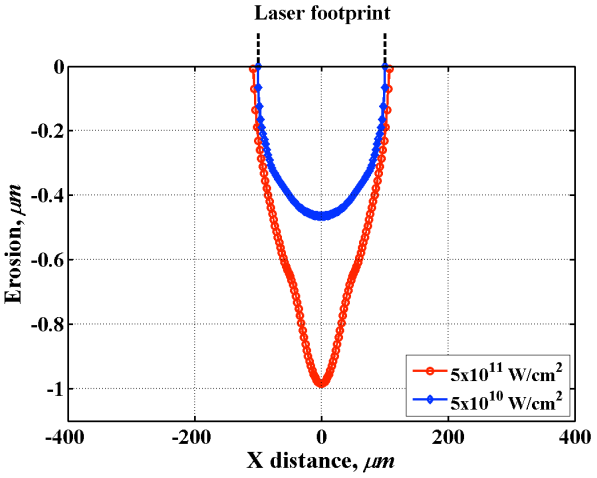

Figure XIII.22. Crater depth and shape in C target created by Nd:YAG laser with 100 μm spot, 10 ns pulse, and $5x10^{10}$ and $5x10^{11}$ W/cm^2 intensities.

Application of LPP to simulate shielding analysis in magnetic fusion

Above results of comparative analysis of plasmas created from solid targets in MFE and LPP devices showed the potential application of simple and well-diagnosed laser experiments to study material erosion and shielding efficiency. The analysis showed the possibility of extrapolating the results to the intensities

and time scales relevant to MFE reactor during major plasma instabilities. Effects of the strong radiation from the shielding plasma on secondary nearby components can be predicted based on analysis of plasma radiation in LPP devices. Several laser beam parameters such as beam intensity, spot size, and pulse duration can be used and adjusted to study through modeling and simple experiments to predict various materials behavior at different extreme conditions. The effect of laser wavelength as well as number of laser beam shots on crater formation, evaporated mass, and material modification should be also considered in details in relation to understanding the effect of various plasma instabilities on PFCs in tokamaks. Further assessment of various mechanisms and processes in MFE environment such as the strong oblique magnetic field will require more comprehensive 3D modeling of LPP devices. We are currently implementing these effects. Comprehensive modeling of reactor environment during plasma instabilities and target ablation using LPP devices with adjusted parameters can help in predicting material damage and lifetime from direct plasma energy deposition as well as from plasma radiation of the shielding layer.

Summary

Laser beams can be used with adjusted parameters to study through modeling and well-diagnosed simple experiments to predict materials behavior and lifetime at extreme conditions anticipated in magnetic fusion energy systems. We developed and implemented scaling mechanism, from LPP to MFE regimes, to study wall erosion, plasma shielding and radiation in MFE reactor conditions, based on modeling of LPP devices using their typical temporal and spatial scales. In spite of the large differences in time scales, energy source, and intensities of transient events between MFE reactors and nanosecond laser devices we found analogy in plasma evolution and shielding efficiency among these systems. Such approach will allow utilizing validated modeling and well-designed simple experimental studies of LPPs for predictions of plasma facing and nearby components damage in MFE environment due to both incident plasma energy as well as radiation of shielding layer developed during plasma instabilities.

XIV. Experimental Simulation of Materials Degradation of Plasma-facing Components Using Laser Beams

Currently high current ion and electron beams are used in laboratories for simulating the behavior of PFC materials under ITER-like conditions. Our study indicates that high-power nanosecond lasers can be used for laboratory simulation of high heat flux PFC material degradation [213]. In this study, we exposed tungsten (W) surfaces with repetitive laser pulses from a nanosecond laser with a power density ~ a few GW cm^{-2}. Our results indicate that the typical particle emission features from laser-irradiated tungsten are consistent with high-power particle beam simulation results.

An Nd:YAG laser operating at 1064 nm and at 10 Hz repetition rate was used to expose a polycrystalline cold-rolled W (99.95% purity, average grain size ~1μm). The laser gives 6 ns full-width at half-maximum (FWHM) pulses and possesses an approximately Gaussian profile. The whole experiments were performed in a high vacuum chamber with a base pressure of $\sim 10^{-6}$ Torr. To provide a fresh W surface for each measurement, the target was mounted on an XY translational stage. The laser beam was allowed to pass through a window of the chamber and focused perpendicularly on the sample surface using a plano-convex lens (f = 40 cm) with spot diameter ~500μm. The fluence at the target surface was set at ~0.46 MJ m^{-2} (~7.6 GW cm^{-2}) for the entire experiments. A complementary metal–oxide– semiconductor (CMOS) sensor camera with 2 ms exposure per frame was used to record time-integrated emission of particle streams. The time evolution of plasma self-emission and the particle distribution were collected by fast-gated imaging setup comprising of an intensified charged coupled device (ICCD) camera. The spectral emission features of the particles were analyzed using a 0.5 m triple grating (1800, 600 and 150 lines mm−1) spectrograph, which was coupled to an ICCD. To analyze the particle size and their distribution from the W surface, a polish silicon substrate was placed at a distance

of 12 cm and was characterized using an atomic force microscope (AFM). Surface morphology of the treated samples was characterized by utilizing scanning electron microscope (SEM).

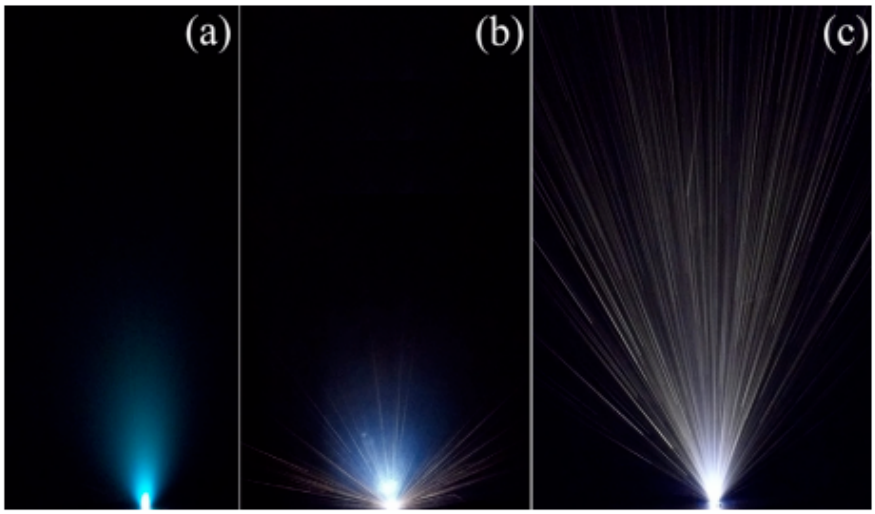

Figure XIV.1. Time-integrated images of emission from W target after laser exposure of 0.46 MJ m^{-2} are given for different power loads. A 2 ms time integration was used for recording the images. (a) Image of the plasma after the first shot, (b) stream of ejected particles after ~50 pulses and (c) stream of ejected particles after ~100 pulses.

Figure XIV.1 shows the time-integrated particle emission recorded during the laser interaction with the polycrystalline W with an integration time of 2 ms. It should be noted that there were no particle emissions during the first few pulses as shown in figure XIV.1(a). Particle emission started after loading the tungsten surface with repetitive laser pulse exposure. At 0.46 MJ m^{-2} energy load, particle emission started after about ~50 pulses with higher flux at large angles to the target normal, as shown in figure 1(b). The number of emitted particles increases with a higher flux emerging normal to the target surface with further exposure of the W surface with subsequent laser pulses, as shown in figure XIV.1(c).

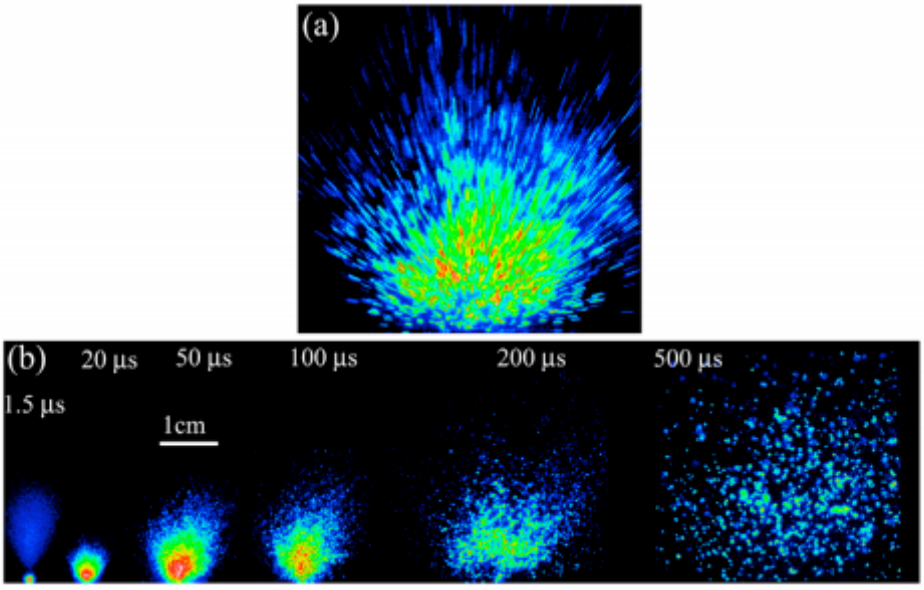

Figure XIV.2. W plume/particle images recorded at different times using an ICCD after the laser pulses are given; (a) time-integrated with an integration time 2µs and delay 100µs and (b) time-resolved traces of tungsten particles obtained using 500 ns gate width.

The ICCD provides a 2D view of 3D plume expansion and particle emission features and provides useful information about hydrodynamics. Figure XIV.2(a) shows the stream of particles acquired using an integration time of 2µs and with a delay of 100µs while figure XIV.2(b) shows the time-resolved particle emission captured at various times after laser exposure. The particle emission features were observed even after 500µs after the termination of the laser pulse. Particles continue to be ejected from the surface after the laser impact and their velocity can be estimated from the length of their traces. An average

velocity of 50 ms^{-1} was derived from the particle movement in a direction perpendicular to the target surface. The mechanism of particle generation was attributed to the brittle destruction of carbon at an elevated temperature.

A typical normalized broadband continuum emission spectrum and semi-logarithmic plot corrected for the spectral response of the detection system are given in figures XIV.3(a) and (b), respectively. The temperature estimate of the particles showed that they possess higher temperatures at early times with a maximum recorded temperature ~4300 K at 1µs, but rapidly cools down to ~2400 K at 10µs. The temperature curve with time showed a t^{-1} dependence (curve fit in figure XIV.3(b)).

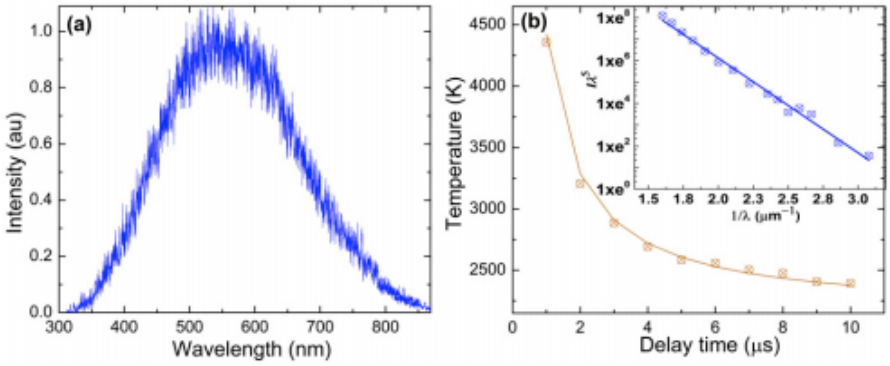

Figure XIV.3. A typical spectrum of thermal emission from particles recorded after 10µs delay with a gate width of 1µs and at a distance 2 mm from the target surface and (b) variation in particle temperature with delay time with respect to laser peak (distance = 2 mm). The solid curve corresponds to t^{-1} fitting. The inset of (b) shows the typical semi-logarithmic plot of I λ^5 against $1/\lambda$ after spectral response correction (distance 2 mm, time delay 2µs).

Figure XIV.4(a) presents the surface morphology of the irradiated tungsten surface after 50 laser shots with a laser energy density of ~0.46 MJ m^{-2}. SEM micrographs clearly indicate that the energy load was sufficient to provide melting. The laser-treated area can be divided into the central melting pool and a region around it where the melting material solidified in the form of microstructures. The ridge formation with melted whirlpools or channels around the central portion, turbulence with liberation of micrometre-sized particulates, droplets and cracks can be seen in the treated surface.

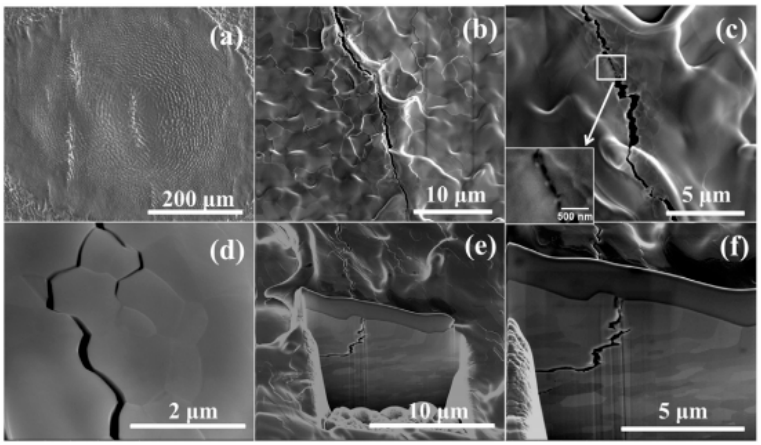

Figure XIV.4. (a) Surface morphology of the W surface after irradiation with 50 pulses at 0.46 MJ m^{-2}. (b) Crack near the molten region with a varying width that ranges from 150 to 550 nm. (c), (d) A zoomed region indicates that the crack occurred through a recrystallized region of ultrafine grains (<500 nm). (e), (f) Cross-section imaging of the cracks show a depth of a few micrometres in the middle of the molten region.

The nature of the cracks observed on the treated surfaces is evident in the surface and cross-sectional SEM images. Figure XIV.4(b) shows a crack near the molten region with a varying width that ranges from 150 to 550 nm. A zoomed region (figure XIV.4(c)) indicates that the crack occurred through a recrystallized region of ultrafine grains (<500 nm). Figure XIV.4(d) confirms the same observation outside the molten region. The majority of the cracks are on the molten region or in the periphery. Moreover, figures XIV.4(c) and (d) demonstrate that

the cracks which occurred through the grain boundaries were intergranular in nature, which is a sign of brittle destruction behavior in tungsten. Cross-sectional imaging of the cracks shows a crack depth of a few micrometers (figures XIV.4(e) and (f)) in the middle of the molten region. Particles with a size of a few micrometers were found inside the bulk cracks as shown in figures XIV.4(c), (d). This concludes that the bulk cracks produce large particles and these results are consistent with large particle generation from the W surface under intense ion beam irradiation. We believe that the fine cracks along the grain boundaries are responsible for the generation of small particles. Due to the exposure of the W surface with repetitive laser pulses, the delayed pulses interact with reconditioned target (melted and recrystallized). During the recrystallization of the surface, particles are loosely bounded at the grain boundaries. These loosely bounded particles are easily ejected during the irradiation of the next pulse. This makes the grain boundaries distinct and wider, resulting in their cracking, as given in figures XIV.4(c) and (d). We estimated particle distribution and their sizes by placing a silicon substrate at an angle of 20◦ with respect to the target normal and at a distance of 12 cm from the target surface. The AFM study of the deposited particles revealed that particles with hundreds of nanometre sizes were generated with a maximum probable size ∼50 nm diameter (figure not given). This is in good agreement with the SEM observation of some small particles in the vicinity of the crack (figure XIV.4(c)).

In conclusion, Tungsten target was exposed with repetitive pulses at 0.46 MJ m^{-2} energy loads from a high-power nanosecond laser. Intense particle emission was observed from the exposed W target and it started after a certain number of pulses. It has been concluded from the surface morphology characterization of treated surface that ductile-to-brittle transition of W is responsible for the generation of particles. Two types of cracks were observed on the treated surface; major cracks with 500 nm width and a network of fine grains around the grain boundaries with 200 nm width. Residual stresses are believed to be responsible for the bulk crack formation and large particles. Small particles are formed from the grain boundaries after the recrystallization of molten material. Our investigation showed the similarity in particle emission as well as surface morphology with the ion beam interaction with W target. Even though the power density used in this study is higher compared with the expected values in ITER, these results could be useful for the investigation of PFC erosion and material degradation during the abnormal events under ELM-like transients and high-energy loads.

XV. Effect of surface segregation and mobility on erosion of plasma-facing materials

We studied mixing materials evolution and resulting effects on plasma performance and erosion lifetime of MFE-related materials using our ITMC-DYN Monte Carlo simulation package. We combined and integrated collisional and thermal processes to study tungsten erosion by the energetic carbon impurity ions during plasma operation. Integrated self-consistent simulation of particles collisional processes, radiation enhanced diffusion, and surface segregation allowed explaining recent experimental results regarding the difference in tungsten erosion and buildup of carbon layer at different target temperatures. Based on various experimental predictions for the diffusion coefficients and the segregation energy we found several key dependences that can affect carbon impurity behavior in tungsten at various temperatures. The integrated simulation allowed reproducing the experimental results [214, 215] and predicting transition from enhanced tungsten erosion to significant surface coverage by carbon on the tungsten surface. Simulations for wider range of system conditions including mixed ion beams with hydrogen isotopes content can be done by including detailed modeling of chemical erosion in self-consistent analysis. The developed models and simulation package can then be used to predict mixed materials behavior and evolution and the effect on plasma operation in future devices such as ITER.

The calculated carbon implantation, the difference between incoming carbon (dotted black line) and sputtered and reflected for two temperatures, are shown in Fig. XV.1 as a function of fluence. At higher, 870 K target temperature, carbon coverage of the surface was significantly delayed and an increased tungsten erosion was found (Figs. XV.1 and XV.2).

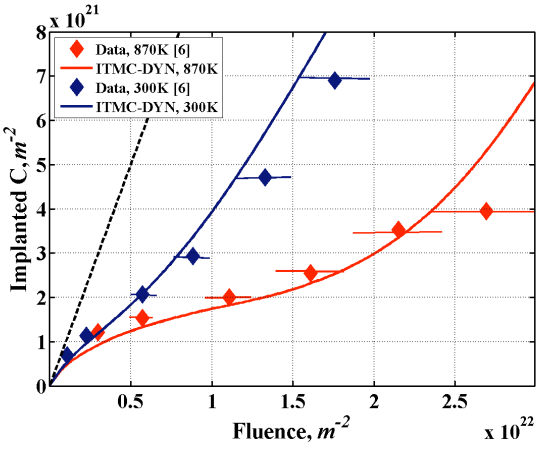

Figure XV.1. Carbon implantation at 300 K and 870 K. Ion beam parameters: 10^{18} $m^{-2}s^{-1}$, 6 keV at 15° of incidence. Modeling of diffusion and surface segregation at 870K: segregation energy = 2 eV; diffusion coefficient = $7x10^{-20}$ m^2s^{-1}; mobility coefficient = 10^{-21} m^2s^{-1}/kT. Experimental results from [215]

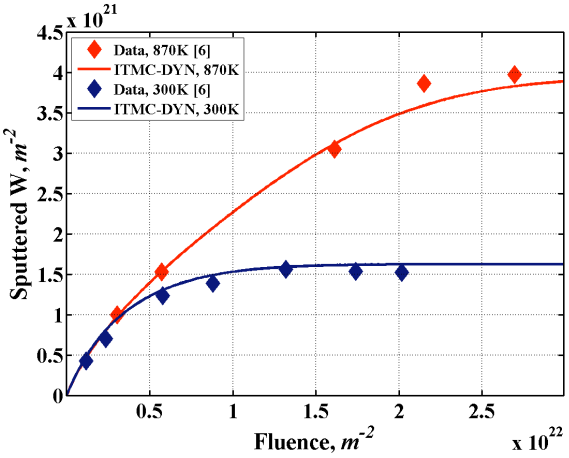

Figure XV.2. Tungsten erosion by carbon ions at 300 K and 870 K. Ion beam parameters: 10^{18} $m^{-2}s^{-1}$, 6 keV at 15° of incidence. Modeling of diffusion and surface segregation at 870K: segregation energy = 2 eV; diffusion coefficient = $7x10^{-20}$ m^2s^{-1}; mobility coefficient = 10^{-21} m^2s^{-1}/kT. Experimental results from [215]

Several processes can cause enhanced sputtering of tungsten and carbon at higher temperatures. First, radiation enhanced diffusion (RED) due to high radiation damage in tungsten by the energetic 6 keV ions can be significant at the considered temperature, and become much higher than pure thermal diffusion. The RED increases and promotes the transfer/migration of carbon atoms from the main deposition area to the surface as well as to the bulk. Second, carbon segregation to the near surface layers further increases carbon motion/diffusion to the surface. Combination of these processes results in accumulation of carbon on the surface that leads to higher carbon sputtering by the incoming ions. Migration of carbon to the surface and the subsequent increase in sputtering, however, reduces its accumulation in the target. As a result, the more collisions of ions with tungsten atoms also lead to the enhanced erosion of tungsten.

ITMC-DYN simulation results were obtained integrating collisional and thermal processes described above. Results shown in Figs. XV.1 and XV.2 are in good agreement with experimental measurements except the data for carbon implantation at higher fluence in the target at 870 K. The linear increase in carbon implantation at fluence > $2.5x10^{22}$ m^{-2} indicates that the surface was covered by carbon and incoming ions interacted only with carbon atoms. Therefore, modeling results at this time were determined only by collisional processes, which were similar to 300 K case.

XVI. Publications related to the DOE Project (2014)

1. J.N. Brooks, A. Hassanein, A. Koniges, P. S. Krstic, T.D. Rognlien, T. Sizyuk, V. Sizyuk, and D.P. Stotler, Scientific and computational challenges in coupled plasma edge/plasma-material interactions for fusion tokamaks, *Contributions to Plasma Physics*, **54** 329 (2014).
2. Jackson G.L., Chrobak C.P., McLean A.G., Maingi R., Mansfield D.K., Roquemore A.L., Diwakar P., Hassanein A., Lietz A., Rudakov D.L., Sizyuk T., and Tripathi J. "Effect of lithium in the DIII-D SOL and plasma-facing surfaces". Journal of Nuclear Materials, in press (2014)

3. G. Miloshevsky and A. Hassanein, Stability and erosion of melt layers developed on plasma facing components of tokamaks, *Nuclear Fusion* **54** *Art. No.*043016 (2014).
4. V. Sizyuk and A. Hassanein, Heat loads to divertor nearby components from secondary radiation evolved during plasma instabilities, *Physics of Plasmas*, accepted for publication (2015).
5. A. Suslova, O. El-Atwani, D. Sagapuram, S.S. Harilal, and A. Hassanein, Recrystallization and grain growth induced by ELMs-like transient heat loads in deformed tungsten samples *Scientific Reports*, **4**, 6845 (2014).
6. V. Sizyuk and A. Hassanein, Efficient Monte Carlo Simulation of Heat Conduction Problems for Integrated Multi-Physics Applications, *Numerical Heat Transfer, Part B* **66**, 381 (2014).
7. X. Yang and A. Hassanein, Kinetic Monte Carlo simulation of hydrogen diffusion on tungsten reconstructed (0 0 1) surface, *Fusion Engineering and Design* **89**, 2545 (2014).
8. F. Genco and A. Hassanein, Simulation of damage to tokamaks plasma facing components during intense abnormal power deposition, *Fusion Engineering and Design* **89**, Issue 4, 335–341 (2014).
9. A. Hu and A. Hassanein, Model to estimate fractal dimension for ion-bombarded materials, *Nuclear Instruments and Methods in Physics Research B* **323**, Pages 82–86 (2014).
10. F. Genco and A. Hassanein, Partile-In-Cell (PIC) methods in predicting materials behavior during high power deposition, *Laser and Particle Beams* **32**, 217 (2014).
11. G. Miloshevsky and A. Hassanein, Effects of plasma flow velocity on melt-layer splashing and erosion during plasma instabilities, *Nuclear Fusion* **54** *Art. No.*033008 (2014).
12. X. Yang and A. Hassanein, Atomic scale calculations of tungsten surface binding energy and beryllium-induced tungsten sputtering, *Applied Surface Science* **293***,* 187-190 (2014).
13. T. Sizyuk and A. Hassanein, Scaling mechanisms of vapor/plasma shielding from laser produced plasmas to magnetic fusion regimes, *Nuclear Fusion*, **54** *Art. No.* 023004 (2014).
14. N Farid, S.S. Harilal, O. El-Atwani, H. Ding, and A. Hassanein, Experimental simulation of materials degradation of plasma facing components using lasers, *Nuclear Fusion* (Letter) **54** *Art. No.* 012002 (2014).
15. T. Sizyuk and A. Hassanein, Effect of surface segregation and mobility on erosion of plasma-facing materials in magnetic fusion systems, *Journal of Nuclear Materials,* accepted for publication (2015).
16. A. Hu and A. Hassanein, Modeling hydrogen isotope behavior in fusion plasma-facing components, *Journal of Nuclear Materials* **446** 56-62 (2014).
17. D. L. Rudakov, P. C. Stangeby, W. R. Wampler, J. N. Brooks, N. H. Brooks, J. D. Elder, A. Hassanein, A.W. Leonard, A. G. McLean, R. A. Moyer, T. Sizyuk, J. G. Watkins and C. P. C. Wong, Net versus gross erosion of high-Z materials in the divertor of DIII-D, *Physica Scripta***, T159**, 014030 (2014).
18. J. Tripathi, T. Novakowski, G. Joseph, J. Linke, A. Hassanein, Temperature Dependent Surface Modification of Molybdenum due to Low Energy He^+ Ion Irradiation, *Nuclear Fusion,* submitted.
19. J.N. Brooks, L. El-Guebaly, A. Hassanein, T. Sizyuk "Plasma Facing Material Alternatives to Tungsten". Accepted for Publications in Nuclear Fusion (2014).

XVII. References

1. R.M. Kulsrud *MHD Description of Plasma* in: M.N. Rosenbluth and R.Z. Sagdeev (Eds.), Handbook of Plasma Physics, vol.1 Basic Plasma Physics, North-Holland Publisher Company (1983).
2. Q. Hu *et al*, Effect of externally applied resonant magnetic perturbations on resistive tearing modes, *Nucl. Fusion* **52** 083011 (2012).
3. J.D. Lore *et al*, Implementation of the 3D edge plasma code EMC3-EIRENE on NSTX, *Nucl. Fusion* **52** 054012 (2012).

4. F. Militello *et al*, Simulations of edge and scrape off layer turbulence in mega ampere spherical tokamak plasmas, *Plasma Phys. Control. Fusion* **54** 095011 (2012).
5. R. Paccagnella *et al,* 3D MHD VDE and disruptions simulations of tokamaks plasmas including some ITER scenarios, *Nucl. Fusion* **49** 035003 (2009).
6. H.W. Kugel *et al,* NSTX plasma response to lithium coated divertor, *J. Nucl. Mater.* **415** S400 (2011).
7. S.I. Braginskii *Transport Processes in a Plasma* in: M.A. Leontovich (Ed.), Reviews of Plasma Physics, vol.1 Consultants Bureau, New York (1965).
8. S.K. Erents *et al,* EDGE2D modeling of JET and ITER including the combined effect of guiding centre drifts and an edge transport barrier, *J. Nucl. Mater.* **363-365** 565 (2007).
9. A. Loarte *et al,* Progress in the ITER Physics Basis Chapter 4: Power and particle control, *Nucl. Fusion* **47** S203 (2007).
10. K.C. Shaing Extended neoclassical transport theory for incompressible tokamak plasmas, *Phys. Plasmas* **4** 3320 (1997).
11. C. Angioni *et al,* Particle transport in tokamak plasmas, theory and experiment, *Plasma Phys. Control. Fusion* **51** 124017 (2009).
12. D.P. Stotler *et al,* Simulations of NSTX with a Liquid Lithium Divertor Module, *Contrib. Plasma Phys.* **50** 368 (2010).
13. Y. Todo *et al,* Simulation of Alfvén eigenmode bursts using a hybrid code for nonlinear magnetohydrodynamics and energetic particles, *Nucl. Fusion* **52** 033003 (2012).
14. R.V. Budny *et al,* Benchmarking ICRF full-wave solvers for ITER, *Nucl. Fusion* **52** 023023 (2012).
15. H. Frerichs *et al,* Numerical analysis of particle recycling in the TEXTOR helical divertor, *Nucl. Fusion* **52** 023001 (2012).
16. A.H. Kritz *et al,* Integrated modeling for prediction of optimized ITER performance, *Nucl. Fusion* **51** 123009 (2011).
17. J.W. Coenen *et al,* Analysis of tungsten melt-layer motion and splashing under tokamak conditions at TEXTOR, *Nucl. Fusion* **51** 083008 (2011).
18. V. Sizyuk and A. Hassanein, Damage to nearby divertor components of ITER-like devices during giant ELMs and disruptions, *Nucl. Fusion* **50** 115004 (2010).
19. T.K. Gray *et al,* Dependence of divertor heat flux widths on heating power, flux expansion, and plasma current in the NSTX, *J. Nucl. Mater.* **415** S360 (2011).
20. A. Kreter *et al,* Dynamics of erosion and deposition in tokamaks, *J. Nucl. Mater.* **390–391** 38 (2009).
21. V. Sizyuk and A. Hassanein, Integrated models to study the impact of ELMs and disruptions on lithium in the NSTX divertor, *J. Nucl. Mater.* **415** S881 (2011).
22. V. Sizyuk and A. Hassanein, Self-consistent analysis of the effect of runaway electrons on plasma facing components in ITER, *Nucl. Fusion* **49** 095003 (2009).
23. A. Hassanein, *et al,* New critical assessments of chamber and wall response to target implosion in inertial fusion reactors, *Fusion Eng. Des.* **69** 781 (2003).
24. A.Hassanein, I. Konkashbaev, Comprehensive modeling of ELMs and their effect on plasma-facing surfaces during normal tokamak operation, *J. Nucl. Mater.* **313-316** 664 (2003).
25. V. Sizyuk and A. Hassanein, Integrated self-consistent analysis of NSTX performance during normal operation and disruptions, *Journal of Nuclear Materials* **438** S809-S813 (2013).
26. V. Sizyuk and A. Hassanein, Kinetic Monte Carlo simulation of escaping core plasma particles to SOL for accurate response of plasma-facing components, *Nuclear Fusion* **53** 073023 (2013).
27. G. Miloshevsky and A. Hassanein, Stability and erosion of melt layers developed on plasma facing components of tokamaks, *Nuclear Fusion* **54** 043016 (2014).
28. A. Hassanein *et al*., *HEIGHTS-EUV package for DPP source modeling,* in: Bakshi V. (Ed.), EUV Sources for Lithography, Chap. 9, SPIE, Bellingham, WA (2006).
29. A. Hassanein, V. Sizyuk, and T. Sizyuk, The Effect of Critical Plasma Densities of Laser-Produced Plasma on Production of Extreme Ultraviolet Radiation, *IEEE Transactions on Plasma Science*, **39** 2810 (2011).

30. M. Rieth *et al.,* Recent progress in research on tungsten materials for nuclear fusion applications in Europe, *J. Nuclear Materials* **432** 482 (2013).
31. C.C. Baker *et al.,* "STARFIRE–A COMMERCIAL TOKAMAK FUSION POWER PLANT STUDY", Argonne National Laboratory Report ANL/FPP-80-1 (1980).
32. L. El-Guebaly *et al.,* Goals, challenges, and successes of managing fusion activated materials, *Fusion Eng. Design* **83** 928 (2008).
33. S.S. Harilal, T. Sizyuk, V. Sizyuk, and A. Hassanein, Efficient laser-produced plasma EUV sources using grooved Sn targets, *Applied Physics Letters* **96** 111503 (2010).
34. A. Hassanein, V. Sizyuk, V. Tolkach, V. Morozov, T. Sizyuk, B.J. Rice, and V. Bakshi Simulation and Optimization of DPP Hydrodynamics and Radiation Transport for EUV Lithography Devices, *Proceedings of SPIE. Emerging Lithographic Technologies VIII*, Santa Clara, CA, vol. 5374, Part 1, pp. 413-422, SPIE, Bellingham, WA, (2004).G5
35. J.A.Jr. Fleck and J.D. Cummings, An implicit Monte Carlo scheme for calculating time and frequency dependent nonlinear radiation transport, *J. Comp. Phys.* **8** 313 (1971).
36. Ya. Zeldovich and Yu. Raizer, *Physics of Shock Waves and High-Temperature Hydrodynamics Phenomena* Academic Press, New York and London (1966).
37. R. Siegel and J. Howell *Thermal Radiation Heat Transfer* Hemisphere Publishing Corp., Washington, New York, London (1981).
38. Tolkach V., Morozov V., and Hassanein A. *Development of Comprehensive Models for Opacities and Radiation Transport for IFE Systems* Argonne National Laboratory Report ANL-ET/02-23, Argonne, IL (2002).
39. S.S. Harilal, G.V. Miloshevsky, T. Sizsyuk and A. Hassanein, Effects of excitation laser wavelength on Ly-alpha and He-alpha line emission from nitrogen plasmas, *Physics of Plasmas,* **20** 013105 (2013).
40. F.Herman and S. Skillman, *Atomic Structure Calculations,* Prentice Hall, Englewood Cliffs, (1963).
41. D. Zaltzmann, *Atomic Physics in Hot Plasmas,* Chap.4, Oxford University Press, New York (1998).
42. J.P. Apruzese *et al,* A direct solution of the equation of transfer using frequency- and angle-averaged photon escap e probabilities, with application to a multistage, multilevel aluminum plasma, *J. Quant. Spectrosc. Radiat. Transfer,* **23** 479 (1980).
43. S.S. Harilal *et al,* The effect of excitation wavelength on dynamics of laser-produced Sn plasma, *J. Appl. Phys.* **109** 063306 (2011).
44. V. Sizyuk *et al., Heights Integrated Model as Instrument for Simulation of Hydrodynamic, Radiation Transport, and Heat Conduction Phenomena of Laser-Produced Plasma in EUV Applications*, Argonne National Laboratory Report ANL-MCS-CPH-06/56, Argonne, IL (2006).
45. A. Hassanein, T. Sizyuk, V. Sizyuk, and S.S. Harilal, Combined effects of pre-pulsing and target geometry on efficient EUV production from laser produced plasma experiments and modeling, *Proceedings of SPIE,* **7969** 79690D (2011).
46. V. Sizyuk, A. Hassanein, and T. Sizyuk, Hollow laser self-confined plasma for extreme ultraviolet lithography and other applications, *Laser and Particle Beams*, **25** 143-154 (2007).
47. Villari R., *et al.,* Nuclear analysis of the ITER full-tungsten divertor, *Fusion Eng. Des.* **88** 2006 (2013).
48. Reiter D., *et al.,* Detailed atomic, molecular and radiation kinetics in current 2D and 3D edge plasma fluid codes, *J. Nucl. Mater.* **363–365** 649 (2007).
49. Scott H.A. and Adams M. L., Radiation Transport in Tokamak Edge Plasmas, *AIP Conf. Proc.* **645** 40 (2002).
50. T. Sizyuk and A. Hassanein, The role of plasma evolution and photon transport in optimizing future advanced lithography sources, *J. Appl. Phys.* **114** 083109 (2013).
51. K. Nishihara *et al.,* Plasma physics and radiation hydrodynamics in developing, *Phys. Plasmas* **15** 056708 (2008).
52. C. Kessel *et al.,* The ARIES Advanced and Conservative Tokamak (ACT) Power Plant Study, Fusion Science Tech., *to be published* (2014).

53. L. El-Guebaly *et al.,* W-Based Alloys for Advanced Divertor Designs: Options and Environmental Impact of State-of-the-Art Alloys, *Fusion Science Tech.,* **60** 185 (2011).
54. R. E. Alcouffe, et al., "PARTISN: A Time-Dependent, Parallel Neutral Particle Transport Code System," LANL Report LA-UR-05-3925 (2005).
55. P. Wilson, D. Henderson, "ALARA: Analytic and Laplacian Adaptive Radioactivity Analysis: A Complete Package for Analysis of Induced Activation," University of Wisconsin Fusion Technology Institute Report Volume I - UWFDM-1070. Volume II - UWFDM-1071 (1998).
56. D. L. Aldama, A. Trkov, "FENDL-2.1 Update of an Evaluated Nuclear Data Library for Fusion Applications," International Atomic Agency Report INDC(NDC)-467 (2004).
57. J.N. Brooks, *Fusion Eng. Des.* **60** 515 (2002).
58. T. Sizyuk, A. Hassanein, *J. Nuclear Materials* **404** 60 (2010).
59. N. Matsunami *et al., Atomic Data and Nuclear Tables* **31** 1 (1984).
60. The Originating Developer of ADAS is the JET Joint Undertaking.
61. H.S. Barnard, B. Lipschultz, D.G. Whyte, *J. Nuclear Materials* **415** S301 (2011).
62. J.N. Brooks, *Nuclear Fusion* **53** 042001 (2013).
63. J.N. Brooks, J.P. Allain, T.D Rognlien, *Physics of Plasmas* **13** 122502 (2006).
64. J.N. Brooks et al., *Contrib. Plasma Physics* **54** 329 (2014).
65. A. Hassanein, *Fusion Eng. Design* **60** 527 (2002).
66. A. Hassanein, T. Sizyuk, I. Konkashbaev, *J. Nuclear Materials* **390-391** 777 (2009).
67. G. Miloshevsky, A. Hassanein, *Nuclear Fusion* **54** 0430 (2014).
68. J.N. Brooks *et al., Nuclear Fusion* **49** 035007 (2009)
69. T. Sizyuk, A. Hassanein, M. Ulrickson, *Fusion Eng. Design* **88** 160 (2013).
70. A. Hassanein *et al., J. Nuclear Materials* **438** S1266 (2013).
71. B.R. Simonovic, S.V Mentus, R. Dimitrijevic, *J. Serb. Chem. Soc.* **68** 657(2003).
72. C.P.C. Wong, *et al., J. Nucl. Mater.* **196–198** 871 (1992).
73. J.N Brooks, D.G. Whyte, *Nuclear Fusion* **39** 525 (1999).
74. P.C. Stangeby *et al., J. Nucl. Mater.* 438 S309 (2013).
75. J.N. Brooks, A. Hassanein, T. Sizyuk, ibid S673.
76. D.L. Rudakov, *et al., Phys. Scr.* **T159** 014030 (2014).
77. D. Naujoks *et al., Nuclear Fusion* **36** 671 (1996).
78. D. L. Rudakov *et al.* "Reduction of Net Erosion of High-Z PFC Materials in DIII-D Divertor Due to Re-Deposition and Low-Z Coating", IAEA-2014 Proceedings, *in press.*
79. J.D. Elder, *et al., J. Nucl. Mater.* **337–339** 79 (2005).
80. S. Lisgo, *et al., J. Nucl. Mater.* **337–339**, 256 (2005).
81. G. Federici, C.H. Skinner, J.N. Brooks, J.P. Coad, C. Grisolia*, et al.,* Plasma-material interactions in current tokamaks and their implications for next step fusion reactors *Nucl Fusion* **41** 1967 (2001).
82. G. Federici, Plasma wall interactions in ITER *Phys Scripta* **T124** 1 (2006).
83. A. Hassanein and I. Konkashbaev, Comprehensive physical models and simulation package for plasma/material interactions during plasma instabilities *J Nucl Mater* **273** 326 (1999).
84. A. Hassanein, T. Sizyuk and I. Konkashbaev, Integrated simulation of plasma surface interaction during edge localized modes and disruptions: Self-consistent approach *J Nucl Mater* **390-91** 777 (2009).
85. Y. Hirooka, M. Bourham, J.N. Brooks, R.A. Causey, G. Chevalier*, et al,* Evaluation of Tungsten as a Plasma-Facing Material for Steady-State Magnetic Fusion Devices, *J Nucl Mater* **196,** 149 (1992).
86. E. Lasnner and W.-D. Schubert, *Tungsten: Properties, Chemistry, Technology of the Element, Alloys and Chemical Compounds* (Kluwer Academic, New York, 1999).
87. W.G. Wolfer and A.M. Hassanein, On Melt Layer Stability Following a Plasma Disruption, *J Nucl Mater* **111,** 560 (1982).
88. A.M. Hassanein, G.L. Kulcinski and W.G. Wolfer, Dynamics of Melting, Evaporation, and Resolidification of Materials Exposed to Plasma Disruptions, *J Nucl Mater* **111,** 554 (1982).

89. A. Hassanein and I. Konkashbaev, Lifetime evaluation of plasma-facing materials during a tokamak disruption, *J Nucl Mater* **233,** 713 (1996).
90. A. Hassanein, V. Belan, I. Konkashbaev, L. Nikandrov, V. Safronov*, et al.,* Modeling and simulation of melt-layer erosion during a plasma disruption, *J Nucl Mater* **241,** 288 (1997).
91. A. Hassanein, Prediction of material erosion and lifetime during major plasma instabilities in tokamak devices, *Fusion Eng Des* **60,** 527 (2002).
92. B.N. Bazylev, G. Janeschitz, I.S. Landman, A. Loarte and S.E. Pestchanyi, Melt damage simulation of W-macrobrush and divertor gaps after multiple transient events in ITER, *J Nucl Mater* **363,** 1011 (2007).
93. B. Bazylev, G. Janeschitz, I. Landman, S. Pestchanyi, A. Loarte*, et al.,* Behaviour of melted tungsten plasma facing components under ITER-like transient heat loads Simulations and experiments, *Fusion Eng Des* **83,** 1077 (2008).
94. B. Bazylev, G. Janeschitz, I. Landman, A. Loarte, N.S. Klimov*, et al.,* Experimental and theoretical investigation of droplet emission from tungsten melt layer, *Fusion Eng Des* **84,** 441 (2009).
95. B. Bazylev, Y. Igitkhanov, J.W. Coenen, V. Philipps and Y. Ueda, Numerical simulations of tungsten melt layer erosion caused by J x B force at TEXTOR, *Phys Scripta* **T145,** 014054 (2011).
96. J. Roth, E. Tsitrone, A. Loarte, T. Loarer, G. Counsell*, et al.,* Recent analysis of key plasma wall interactions issues for ITER, *J Nucl Mater* **390-391,** 1 (2009).
97. B. Lipschultz, J.W. Coenen, H.S. Barnard, N.T. Howard, M.L. Reinke*, et al.,* Divertor tungsten tile melting and its effect on core plasma performance, *Nucl Fusion* **52,** 123002 (2012).
98. J.W. Coenen, V. Philipps, S. Brezinsek, B. Bazylev, A. Kreter*, et al.,* Analysis of tungsten melt-layer motion and splashing under tokamak conditions at TEXTOR, *Nucl Fusion* **51,** 083008 (2011).
99. K. Krieger, T. Lunt, R. Dux, A. Janzer, A. Kallenbach*, et al.,* Induced tungsten melting events in the divertor of ASDEX Upgrade and their influence on plasma performance, *J Nucl Mater* **415,** S297 (2011).
100. G. Sergienko, B. Bazylev, A. Huber, A. Kreter, A. Litnovsky*, et al.,* Erosion of a tungsten limiter under high heat flux in TEXTOR, *J Nucl Mater* **363,** 96 (2007).
101. G. Sergienko, B. Bazylev, T. Hirai, A. Huber, A. Kreter*, et al.,* Experience with bulk tungsten test-limiters under high heat loads: melting and melt layer propagation, *Phys Scripta* **T128,** 81 (2007).
102. J.W. Coenen, K. Krieger, B Lipschultz, R Dux, A Kallenbach*, et al.,* Evolution of surface melt damage, its influence on plasma performance and prospects of recovery, *J Nucl Mater* **438,** S27 (2013).
103. V.N. Litunovsky, V.E. Kuznetsov, B.V. Lyublin, I.B. Ovchinnikov, V.A. Titov*, et al.,* Material response due to simulated plasma disruption loads, *Fusion Eng Des* **49-50,** 249 (2000).
104. N.I. Arkhipov, V.P. Bakhtin, S.M. Kurkin, V.M. Safronov, D.A. Toporkov*, et al.,* Material erosion and erosion products in disruption simulation experiments at the MK-200 UG facility, *Fusion Eng Des* **49-50,** 151 (2000).
105. A.N. Bandura, O.V. Byrka, V.V. Chebotarev, I.E. Garkusha, V.A. Makhlaj*, et al.,* Melt layer behavior of metal targets irradiatead by powerful plasma streams, *J Nucl Mater* **307,** 106 (2002).
106. V.I. Tereshin, I.E. Garkusha, A.N. Bandura, O.V. Byrka, V.V. Chebotarev*, et al.,* Influence of plasma pressure gradient on melt layer macroscopic erosion of metal targets in disruption simulation experiments, *J Nucl Mater* **313,** 685 (2003).
107. G. Federici, A. Zhitlukhin, N. Arkhipov, R. Giniyatulin, N. Klimov*, et al.,* Effects of ELMS and disruptions on ITER divertor armour materials, *J Nucl Mater* **337,** 684 (2005).
108. I.E. Garkusha, Bazylev B.N., Bandura A.N., Byrka O.V., Chebotarev V.V.*, et al* 2007 Tungsten melt layer erosion due to J x B force under conditions relevant to ITER ELMs *J Nucl Mater* **363** 1021
109. I.E. Garkusha, V.A. Makhlaj, V.V. Chebotarev, I. Landman, V.I. Tereshin*, et al.,* Experimental study of plasma energy transfer and material erosion under ELM-like heat loads, *J Nucl Mater* **390-91,** 814 (2009).
110. A. Zhitlukhin, N. Klimov, I. Landman, J. Linke, A. Loarte*, et al.,* Effects of ELMS on ITER divertor armour materials, *J Nucl Mater* **363,** 301 (2007).

111. N. Klimov, V. Podkovyrov, A. Zhitlukhin, D. Kovalenko, B. Bazylev*, et al.,* Experimental study of PFCs erosion under ITER-like transient loads at plasma gun facility QSPA, *J Nucl Mater* **390-391,** 721 (2009).
112. G. De Temmerman, J. Daniels, K. Bystrov, M.A. van den Berg and J.J. Zielinski, Melt-layer motion and droplet ejection under divertor-relevant plasma conditions, *Nucl Fusion* **53,** 023008 (2013).
113. G.E. Dale and M.A. Bourham, Melt layer erosion and resolidification of metallic plasma facing components, *17th Ieee/Npss Symposium on Fusion Engineering, Vols 1 and 2* 892 (1998).
114. H. Wurz, B. Bazylev, I. Landman, S. Pestchanyi and S. Gross, Macroscopic erosion in tokamak off normal events, *Fusion Eng Des* **56-57,** 397 (2001).
115. V. Safronov, N. Arkhipov, V. Bakhtin, S. Kurkin, F. Scaffidi-Argentina*, et al.,* Material erosion and erosion products under plasma heat loads typical for ITER hard disruptions, *J Nucl Mater* **290,** 1052 (2001).
116. J.W. Coenen, B. Bazylev, S. Brezinsek, V. Philipps, T. Hirai*, et al.,* Tungsten melt layer motion and splashing on castellated tungsten surfaces at the tokamak TEXTOR, *J Nucl Mater* **415,** S78 (2011).
117. J.W. Coenen, V. Philipps, S. Brezinsek, G. Pintsuk, I. Uytdenhouwen*, et al.,* Melt-layer ejection and material changes of three different tungsten materials under high heat-flux conditions in the tokamak edge plasma of TEXTOR, *Nucl Fusion* **51,** 113020 (2011).
118. Y. Shi, G. Miloshevsky and A. Hassanein, Boiling induced macroscopic erosion of plasma facing components in fusion devices, *Fusion Eng Des* **86,** 155 (2011).
119. G.V. Miloshevsky and A. Hassanein, Modelling of Kelvin-Helmholtz instability and splashing of melt layers from plasma-facing components in tokamaks under plasma impact, *Nucl Fusion* **50,** 115005 (2010).
120. Y. Shi, G. Miloshevsky and A. Hassanein, Theoretical studies of macroscopic erosion mechanisms of melt layers developed on plasma facing components, *J Nucl Mater* **412,** 123 (2011).
121. G. Miloshevsky and A. Hassanein, Splashing and boiling mechanisms of melt layer losses of PFCs during plasma instabilities, *J Nucl Mater* **438,** S155 (2013).
122. B. Bazylev, G. Janeschitz, I. Landman, A. Loarte, G. Federici*, et al.,* Experimental validation of 3D simulations of tungsten melt erosion under ITER-like transient loads, *J Nucl Mater* **390-391,** 810 (2009).
123. G. Miloshevsky and A. Hassanein, Modeling of macroscopic melt layer splashing during plasma instabilities, *J Nucl Mater* **415,** S74 (2011).
124. OpenFOAM (2014), user guide, version 2.3.0 Available from: http://www.openfoam.org.
125. C.W. Hirt and B.D. Nichols, Volume of Fluid (Vof) Method for the Dynamics of Free Boundaries, *J Comput Phys* **39,** 201 (1981).
126. E. Berberovic, N.P. van Hinsberg, S. Jakirlic, I.V. Roisman and C. Tropea, Drop impact onto a liquid layer of finite thickness: Dynamics of the cavity evolution, *Phys Rev E* **79,** 036306 (2009).
127. H.G. Weller, G. Tabor, H. Jasak and C. Fureby, A tensorial approach to computational continuum mechanics using object-oriented techniques, *Comput Phys* **12,** 620 (1998).
128. G. Miloshevsky and A. Hassanein, Effects of plasma flow velocity on melt-layer splashing and erosion during plasma instabilities, *Nucl Fusion* **54,** 033008 (2014).
129. G. Miloshevsky and A. Hassanein, Stability and erosion of melt layers developed on plasma facing components of tokamaks, *Nucl Fusion* **54,** 043016 (2014).
130. G. Sergienko, A. Huber, A. Kreter, V. Philipps, M. Rubel*, et al* 2005 Tungsten melting under high power load in the TEXTOR edge plasma In: *32nd EPS Conference on Plasma Physics and Controlled Fusion,* (Tarragona, Spain: Europhys. Conf. Abstracts 29C (2005) P-1.019).
131. J.A. Boedo, D.L. Rudakov, E. Hollmann, D.S. Gray, K.H. Burrell*, et al.,* Edge-localized mode dynamics and transport in the scrape-off layer of the DIII-D tokamak, *Phys Plasmas* **12,** 072516 (2005).

132. I.P. Dojcinovic, Plasma flow interaction with ITER divertor related surfaces, *Journal of Physics: Conference Series* **257**, 012033 (2010).
133. V.I. Tereshin, Quasi-stationary plasma accelerators (QSPA) and their applications, *Plasma Phys Contr F* **37,** A177 (1995).
134. S. Chandrasekhar, *Hydrodynamic and Hydromagnetic Stability* (Oxford University Press, London, 1961).
135. T. Funada and D.D. Joseph, Viscous potential flow analysis of Kelvin-Helmholtz instability in a channel, *J Fluid Mech* **445,** 263 (2001).
136. S. Márquez Damián, Description and utilization of interFoam multiphase solver. Available at http://infofich.unl.edu.ar/upload/3be0e16065026527477b4b948c4caa7523c8ea52.pdf.
137. S.S. Deshpande, L. Anumolu and M.F. Trujillo, Evaluating the performance of the two-phase flow solver interFoam, *Computational Science & Discovery* **5,** 014016 (2012).
138. J.A. Shercliff, Steady Motion of Conducting Fluids in Pipes under Transverse Magnetic Fields, *P Camb Philos Soc* **49,** 136 (1953).
139. J.C.R. Hunt, Magnetohydrodynamic Flow in Rectangular Ducts, *J Fluid Mech* **21,** 577 (1965).
140. J. Klostermann, K. Schaake and R. Schwarze, Numerical simulation of a single rising bubble by VOF with surface compression, *Int J Numer Meth Fl* **71,** 960 (2013).
141. Y. Shibasaki, K. Ueno and T. Tagawa, Computation of a Rising Bubble in an Enclosure Filled with Liquid Metal under Vertical Magnetic Fields, *Isij Int* **50** 363, (2010).
142. H. Ubbink, *Computational Fluid Dynamics of Dispersed Two-Phase Flows at High Phase Fractions* Ph.D Thesis (Imperial College of Science, Technology and Medicine, London) (2002).
143. R.I. Issa, Solution of the implicitly discretised fluid flow equations by operator-splitting, *J Comput Phys* **62,** 40 (1986).
144. H.T. Ji, W. Fox and D. Pace, Study of small-amplitude magnetohydrodynamic surface waves on liquid metal, *Phys Plasmas* **12,** 012102 (2005).
145. G. Janeschitz and I. J. a. HTs, Journal of Nuclear Materials **290-293**, 1 (2001).
146. G. Federici, P. Andrew, P. Barabaschi, J. Brooks, R. Doerner, A. Geier, A. Herrmann e, G. Janeschitz, K. Krieger, A. Kukushkin, A. Loarte, R. Neu , G. Saibene, M. Shimada, G. Strohmayer and M. Sugihara, Journal of Nuclear Materials **313-316**, 11 (2003).
147. G. Federici, C. H. Skinner, J. N. Brooks, J. P. Coad, C. Grisolia, A. A. Haasz, A. Hassanein, V. Philipps, C. S. Pitcher, J. Roth, W. R. Wampler and D. G. Whyte, Nuclear Fusion **41**, 1967 (2001).
148. R. P. Doerner, Journal of Nuclear Materials **363-365**, 32-40 (2007).
149. T. Shimada, T. Funabiki, R. Kawakami, Y. Ueda and M. Nishikawa, Journal of Nuclear Materials **329-333**, 747-751 (2004).
150. Y. Ueda, M. Fukumoto, I. Sawamura, D. Sakizono, T. Shimada and M. Nishikawa, Fusion Engineering and Design **81**, 233-239 (2006).
151. W. Eckstein and J. Roth, Nucl. Instr. and Meth. in Phys. Res. B **53**, 279 (1991).
152. W. Eckstein, V. I. Shulga and J. Roth, Nucl. Instr. and Meth. in Phys. Res. B **153**, 415 (1999).
153. K. Schmid, J. Roth and W. Eckstein, Journal of nuclear materials **290-293**, 148 (2001).
154. A. Al-Ajlony, A. Kanjilal, M. Catalfano, S. S. Harilal and A. Hassanein, Applied Surface Science **289**, 358-365 (2014).
155. R. A. Pitts, S. Carpentier, F. Escourbiac, T. Hirai, V. Komarov, S. Lisgo, A. S. Kukushkin, A. Loarte, M. Merola, A. Sashala Naik, R. Mitteau, M. Sugihara, B. Bazylev and P. C. Stangeby, Journal of Nuclear Materials **438**, S48-S56 (2013).
156. Y. Ueda, M. Fukumoto, J. Yoshida, Y. Ohtsuka, R. Akiyoshi, H. Iwakiri and N. Yoshida, Journal of Nuclear Materials **386-388**, 725-728 (2009).
157. T. Sizyuk and A. Hassanein, Journal of Nuclear Materials **415**, S293-S296 (2011).
158. T. Sizyuk and A. Hassanein, Journal of Nuclear Materials **404**, 60-67 (2010).
159. J. Luthin and C. Linsmeier, Surface Science **454-456**, 78 (2000).
160. H. Yoshida, M. Taniguchi, K. Yokoyama, Y. Yamauchi, Y. Hirohata, M. Akiba and T. Hino, Journal of Nuclear Materials **329-333**, 790-794 (2004).

161. M. Poon, J. W. Davis and A. A. Haasz, Journal of Nuclear Materials **283-287**, 1062 (2000).
162. R. P. Doerner, M. J. Baldwin and P. C. Stangeby, Nuclear Fusion **51**, 043001 (2011).
163. M. J. Baldwin and R. P. Doerner, Journal of Nuclear Materials **404**, 165-173 (2010).
164. S. Kajita, W. Sakaguchi, N. Ohno, N. Yoshida and T. Saeki, Nuclear Fusion **49**, 095005 (2009).
165. M. J. Baldwin and R. P. Doerner, Nuclear Fusion **48**, 035001 (2008).
166. Y. Ueda, K. Miyata, Y. Ohtsuka, H. T. Lee, M. Fukumoto, S. Brezinsek, J. W. Coenen, A. Kreter, A. Litnovsky, V. Philipps, B. Schweer, G. Sergienko, T. Hirai, A. Taguchi, Y. Torikai, K. Sugiyama, T. Tanabe, S. Kajita and N. Ohno, Journal of Nuclear Materials **415**, S92-S95 (2011).
167. J. Moulder, F., W. Stickle, F., P. Sobol, E. and K. Bomben, D. , *Handbook of X-ray Photoelectron Spectroscopy*. (Perkin-Elmer Corporation; Physical Electronics Division, Eden Prairie, Minosota, USA 1992).
168. S. Takamura, N. Ohno, D. Nishijima and S. Kajita, Plasma and Fusion Research **1**, 051-051 (2006).
169. A. Lasa, S. K. Tähtinen and K. Nordlund, EPL (Europhysics Letters) **105**, 25002 (2014).
170. F. Sefta, K. D. Hammond, N. Juslin and B. D. Wirth, Nuclear Fusion **53**, 073015 (2013).
171. Y. V. Martynenko and M. Y. Nagel', Plasma Physics Reports **38**, 996-999 (2012).
172. G. M. Wright, D. Brunner, M. J. Baldwin, K. Bystrov, R. P. Doerner, B. Labombard, B. Lipschultz, G. De Temmerman, J. L. Terry, D. G. Whyte and K. B. Woller, Journal of Nuclear Materials **438**, S84-S89 (2013).
173. S.P. Kowalczyk *et al.* Phys. Rev. B 8, 3583 (1973).
174. G.K. Wertheim *et al.* Solid State Commun. 33, 1127 (1980).
175. Katsuhiko Naoi *et al.* J. Electrochem. Soc. 152, A1047 (2005).
176. Min He *et al.* Nanoscale, 5, 3298 (2013).
177. S. Belkhiat *et al.* Rom. Journ. Phys. 51, 805 (2006).
178. E. Radvanyi *et al.* J. Mater. Chem. A 1, 4956 (2013).
179. A. Suslova, O. El-Atwani, D. Sagapuram, S.S. Harilal, and A. Hassanein, Recrystallization and grain growth induced by ELMs-like transient heat loads in deformed tungsten samples, Scientific Reports, **4**, 6845 (2014).
180. A. Hu and A. Hassanein, Model to estimate fractal dimension for ion-bombarded materials, Nuclear Instruments and Methods in Physics Research B 323, 82 (2014).
181. A. Hassanein, Fusion Technol. 8 (1) (1985) 1735–1741.
182. A. Hu, A. Hassanein, Nucl. Instr. Meth. Phys. Res. Sect. B 281 (2012) 15–20.
183. C. Heinz-Otto Peitgen, The Science of Fractal Images, Springer-Verlag, 1988.
184. D.N. Ruzic, P.C. Smith, R.B. Turkot, J. Nucl. Mater. 241 (1997) 1170–1174.
185. M. Kustner, W. Eckstein, V. Dose, J. Roth, Nucl. Instr. Meth. Phys. Res. Sect. B 145 (3) (1998) 320–331.
186. J. Krim, I. Heyvaert, C. Vanhaesendonck, Y. Bruynseraede, Phys. Rev. Lett. 70 (1) (1993) 57–60.
187. V.I.T.A. de Rooij-Lohmann, I.V. Kozhevnikov, L. Peverini, E. Ziegler, R. Cuerno, F. Bijkerk, A.E. Yakshin, Appl. Surf. Sci. 256 (16) (2010) 5011–5014.
188. A. Hu and A. Hassanein, Modeling hydrogen isotope behavior in fusion plasma-facing components, Journal of Nuclear Materials **446,** 56-62 (2014).
189. W.S. Gorsky, Physikalische Zeitschrift der Sowjetunion 8 (4) (1935) 457–471.
190. J.V.G. Schaumann, G. Alefeld, Phys. Status Solidi 42 (1970).
191. R. Cantelli, Mater. Sci. Eng., A 442 (1–2) (2006) 5–20.
192. M.I. Baskes, Sandia National Laboratories. Report, SAND83-8231, 1983.
193. K.L. Wilson, R. Bastasz, R.A. Causey, D.K. Brice, B.L. Doyle, W.R. Wampler, W. Moller, B.M.U. Scherzer, T. Tanabe, Nucl. Fusion 1 (1991) 31–50.
194. V.K. Alimov, J. Roth, Phys. Scr. T128 (2007) 6–13.
195. O.V. Ogorodnikova, J. Roth, M. Mayer, J. Appl. Phys. 103 (3) (2008).
196. R.H. Ning, Y.G. Li, W.H. Zhou, Z. Zeng, X. Ju, J. Nucl. Mater. 430 (1–3) (2012) 20–26.
197. V.K. Alimov, J. Roth, M. Mayer, J. Nucl. Mater. 337 (1–3) (2005) 619–623.

198. R.H. Ning, Y.G. Li, W.H. Zhou, Z. Zeng, X. Ju, Int. J. Mod. Phys. C 23 (6) (2012).
199. A.V. Golubeva, M. Mayer, J. Roth, V.A. Kurnaev, O.V. Ogorodnikova, J. Nucl. Mater. 363 (2007) 893–897.
200. X. Yang, A. Hassanein, Fusion Engineering and Design 89 (2014) 2545–2549.
201. X. Yang, A. Hassanein, Applied Surface Science 293 (2014) 187– 190.
202. F. Genco, A. Hassanein, Laser and Particle Beams (2014), 32, 217–232.
203. F. Genco, A. Hassanein, Laser and Particle Beams (2014), 32, 305–310.
204. F. Genco, A. Hassanein, Fusion Engineering and Design 89 (2014) 335–341.
205. N.I. Arkhipov, V.P. Bakthin, V.M. Safronov, D.A. Toporkov, S.G. Vasenin, H. Wuerz, A.M. Zhitlukhin, Fusion Techn. 1, 463–466 (1994).
206. N.I. Arkhipov, V.P. Bakthin, S.M. Kurkin, S.E. Pestchanyi, V.M. Safronov, D.A. Toporkov, S.G. Vasenin, H. Wuerz, A.M. Zhitlukhin, Fusion Technol. 507–510. (1996).
207. N.I. Arkhipov, V.P. Bakthin, S.M. Kurkin, V.M. Safronov, D.A. Toporkov, S.G. Vasenin, H. Wuerz, A.M. Zhitlukhin, J. Nucl. Mat. 233–237, 767–770 (1996).
208. V.M. Safronov, N.I. Arkhipov, I.S. Landman, S.E. Pestchanyi, D.A. Toporkov, A.M. Zhitlukhin, J. Nucl. Mat. 386–388, 744–746 (2009).
209. H. Wuerz, S.E. Pestchanyi, I.S. Landman, B. Bazylev, F. Kappler, FZKA 6582, Karlsruhe, Germany (2001).
210. V. Sizyuk, A. Hassanein, and T. Sizyuk (2006) *J. Appl. Phys.* **100** 103106.
211. A. Hassanein and T. Sizyuk (2013) *Phys. Plasmas* **20** 053105.
212. S. S. Harilal, C. V. Bindhu, Riju C. Issac, V. P. N. Nampoori, and C. P. G. Vallabhan (1997) *J. Appl. Phys.* **82** 2140.
213. N. Farid, S.S. Harilal, O. El-Atwani, H. Ding, and A. Hassanein, Nuclear Fusion (Letter) **54** *Art. No.* 012002 (2014).
214. H. T. Lee, K. Krieger, J. Nucl. Mater. 390–391 (2009) 971.
215. H. T. Lee and K. Krieger, Phys. Scr. T138 **(**2009) 014045.